INVESTIGATING CLIMATE IMPACTS OF URBANIZATION AND THE POTENTIAL FOR COOL ROOFS TO MITIGATE THE KANSAS CITY METROPOLITAN AREA'S URBAN HEAT ISLAND EFFECT

A THESIS IN
Environmental and Urban Geosciences

Presented to the Faculty of the University
of Missouri-Kansas City in partial fulfillment of
the requirements for the degree

MASTER OF SCIENCE

by
KYLE REED

B.S., Fort Hays State University, 2008
D.P.T., University of Kansas Medical Center, 2012
B.S., University of Missouri – Kansas City, 2018

Kansas City, Missouri
2020

INVESTIGATING CLIMATE IMPACTS OF URBANIZATION AND THE POTENTIAL FOR COOL ROOFS TO MITIGATE THE KANSAS CITY METROPOLITAN AREA'S URBAN HEAT ISLAND EFFECT

Kyle Reed, Candidate for the Master of Science Degree

University of Missouri – Kansas City, 2020

ABSTRACT

An urban heat island (UHI) is a phenomenon where the temperatures within cities are greater than those of surrounding rural areas due to human activity and physical properties of urban surfaces. This effect can cause the annual mean temperature within cities to be up to 3^{o}C more than its surroundings. As cities have grown with the migration of people from rural to urban areas, the UHI effect has impacted an increasing number of people over time. One method that has been investigated as a way to mitigate the UHI phenomenon is to increase the albedo in cities, which would reflect a greater amount of solar radiation away from urban surfaces compared to conventional materials (e.g. dark asphalt shingles). In this study, we utilize the Weather Research and Forecasting (WRF) model to investigate the UHI under different scenarios during the same heat wave event (i.e. July 2012) in the Kansas City metropolitan area (KCMA). First a suite of sensitivity simulations is performed and analyzed in order to determine the best combination of physical parameterizations for subsequent scenarios. Next, the difference in urban temperatures from 1938 and 2011 is investigated by using land cover data sets representing these two periods of time. Lastly, two cool roof

simulations will be performed to determine the effectiveness of this mitigation strategy on reducing temperatures within the KCMA. The first scenario will represent “newly installed” cool roofs with an albedo of 0.8, and the second will model “aged” cool roofs with an albedo of 0.5. Over the past seven decades, temperatures in the KCMA have been exacerbated by the increase in city size and impervious surface density. Our results indicate that both newly installed and aged cool roof materials are able to mitigate the urban temperatures and the UHI effect during a heat wave in July 2012.

APPROVAL PAGE

The faculty listed below, appointed by the Dean of the College of Arts and Sciences, have examined a thesis titled “Investigating Climate Impacts of Urbanization and the Potential for Cool Roofs to Mitigate the Kansas City Metropolitan Area’s Urban Heat Island Effect” presented by Kyle Reed, candidate for the Master of Science degree, and certify that, in their opinion, it is worthy of acceptance.

Supervisory Committee

Fengpeng Sun, Ph.D., Committee Chair
Department of Earth and Environmental Sciences

Wei Ji, Ph.D.
Department of Earth and Environmental Sciences

Jimmy Adegoke, Ph.D.
Department of Earth and Environmental Sciences

Jejung Lee, Ph.D.
Department of Earth and Environmental Sciences

CONTENTS

LIST OF ILLUSTRATIONS

LIST OF TABLES

ACKNOWLEDGEMENTS

I would like to acknowledge those that have assisted me financially during my graduate program. I would like to thank Dr. Fengpeng Sun for supporting me with his Missouri Established Program to Stimulate Competitive Research (EPSCoR) funding. I would also like to thank the University of Missouri – Kansas City School of Graduate Studies for the 2019 – 2020 Research Grant, the Earth and Environmental Sciences department for the Newcomb Student Research Assistance fund (2018 and 2019), and the Missouri Space Grant Consortium for their Graduate Fellowship (2018 – 2019).

I would also like to thank Dr. Sun, my advisor, for his support guidance during both my undergraduate and graduate programs. I am thankful that you gave me the opportunity to come into your lab and perform research with you as an undergraduate student even though I didn't have experience in this field at that time. I appreciate all the guidance you have provided me in my research and coursework to help me become a well-rounded researcher. I am also appreciative of my committee members, including Dr. Ji, Dr. Adegoke, and Dr. Lee, for their time and thoroughness in reviewing my thesis, and for providing me with constructive feedback. Next, I appreciate Kevin, Ali, Lili, and Jianfen for their helpful advice and assistance with my research. I would also like to thank my family, especially my parents, for their unwavering support throughout my life. Lastly, I would like to thank my wife, Jessica, and children, Ryleigh and Jax, for their love and for always being there for me.

CHAPTER 1. INTRODUCTION

In 2007, the United Nations estimated that half of all people on Earth lived in cities (Whiting and Unwin 2008), and by 2018, that percentage had grown to 55%, which equates to approximately 4.2 billion people globally (United Nations 2018). The same report predicts that by 2050, another 2.5 billion people will be added to the current estimate of urban population. Due to the movement of people from rural areas to cities, urban land cover surface area has also seen substantial gains in recent decades. He et al. (2019) found that urban land cover had more than doubled in area between 1992 to 2016, from 274,400 km^2 to 621,100 km^2, and projected that between 2010 and 2030, urban land cover could increase by over 1.5 million km^2 to in order to support future urban population growth (Seto et al. 2011).

As the number of those living in cities rises, an increasing proportion of people will be affected by climate phenomena that are only experienced in these areas. One example of these such events is the urban heat island (UHI) effect. An UHI occurs when the temperature within cities becomes significantly warmer than those of the surrounding rural areas due to multiple factors, such as human activities and infrastructure (Oke 1982). The UHI effect was first studied and described by Luke Howard in the early 1800s as he compared thermometer readings from London to those in rural locations around the city (Mills 2008). Recently, a study by Bhati and Mohan (2016) analyzed the impact of built-up land cover on temperature over a five-day period in Delhi, India using a climate model. In their findings, the researchers determined that the UHI effect caused temperatures within the city to be as much as 11^oC warmer than those in a rural location during the evening.

1.1 Causes of urban heat islands

The formation of an UHI is complex and involves different factors within cities. First, physical properties of urban surfaces affect the surface energy balance. One physical property of urban surfaces that contributes to the UHI effect is the imperviousness of the materials, e.g. asphalt and concrete. These surfaces have a reduced ability to absorb moisture when compared to soil (Wang et al. 2018). When precipitation falls on impervious surfaces, a majority of the water becomes runoff and is transported away from the city via the storm drainage system. Due to this process occurring, moisture in urban locations is reduced, limiting the cooling effect from evapotranspiration (Kaiser et al. 2019). The decrease in soil moisture also reduces latent heat flux from the surface to the atmosphere, leading to both a gain in the sensible heat flux and energy storage in the subsurface in order to maintain the surface energy balance. Another physical property of urban surfaces that contributes to the UHI effect is their large thermal inertia. Thermal inertia, or thermal admittance, is a measurement that describes how well a material stores and releases heat energy. Asphalt and concrete, for example, have a high thermal inertia value, which causes heat to be stored readily during the day and released slowly at night. Since these surfaces radiate stored heat throughout the night, this surface characteristic is an important aspect in explaining why the difference between rural and urban temperatures are greatest at night.

The second major contribution to the UHI effect is the release of heat from anthropogenic sources (Oke et al. 2017). First, heat is produced from many different human activities, for example, through fuel combustion from vehicles and the use of air conditioners. In a modeling study by Salamanca, et al. (2014), researchers found that the use of air conditioning raised urban temperatures in Phoenix, AZ over 1^{o}C in certain portions of the city. Second, the

production of greenhouse gas emissions from human activities cause a greater amount of longwave radiation to be absorbed in our atmosphere and re-emitted back toward Earth's surface to warm it rather than escaping to space.

A third major contributor to elevated temperatures in the UHI is the geometry of buildings in the city (Oke et al. 2017). Core urban areas tend to have tall buildings that are closely placed together. By having this configuration, heat that has been released from the surface is able to accumulate within the urban canyon instead of being moved away from the city via advection.

Lastly, changes in surface albedo, i.e. the ratio of the amount of solar radiation reflected from a surface to the amount of solar radiation incident upon the surface, affects the amount of energy absorbed by land cover. Asphalt, a common material for constructing roads, has a typical albedo of 7% (Hartmann 1994), meaning that 93% of the energy incident upon it is absorbed. A substantial amount of heat is sequentially stored and emitted from the road surface. As metropolitan areas grow, more and more asphalt is used for constructing roads, replacing natural surfaces with man-made, low-albedo surfaces.

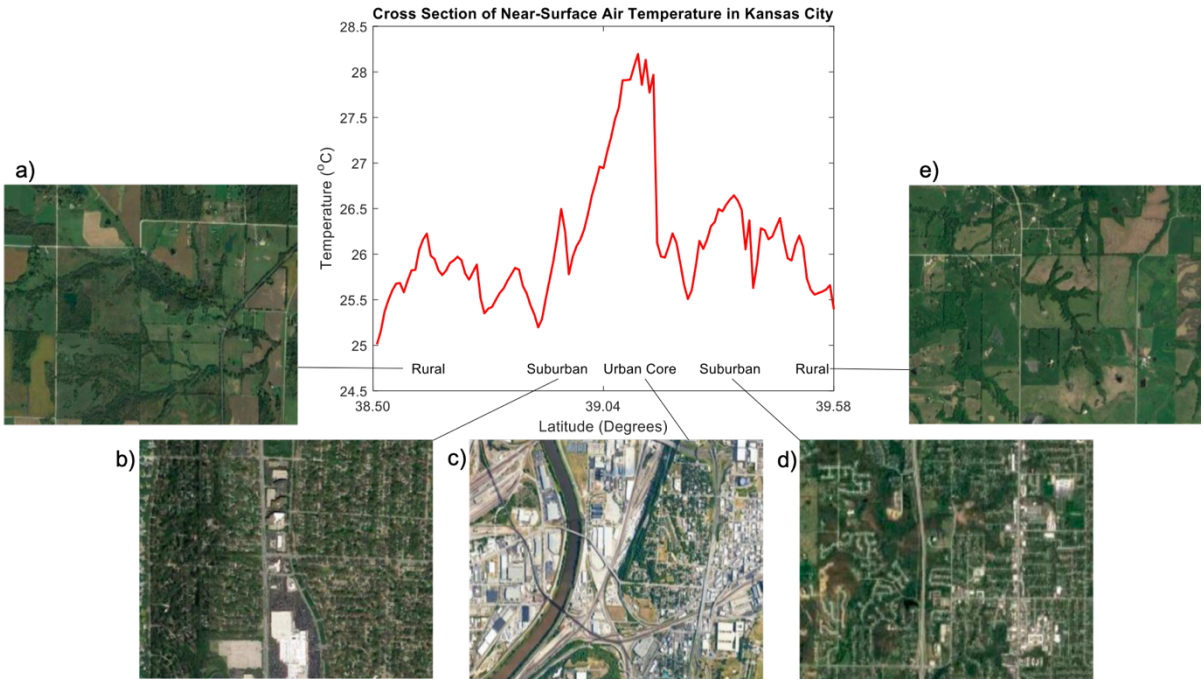

Figure 1. Near-surface air temperature from a climate model simulation along a north-south cross-section through the central portion of the Kansas City metropolitan area at a longitude of 94.6° W. Land cover at different locations within the domain are labeled within the graph, and pictures of land cover at these approximate locations are shown beside and below the graph. These areas include a) cropland near Louisburg, KS, b) suburban Leawood, KS and Kansas City, MO, c) Kansas City, MO and Kansas City, KS urban core, d) suburban Gladstone, MO, and e) cropland near Smithville Lake in Missouri (Google Maps 2020).

A commonly used graph when describing UHIs is shown in Figure 1, where near-surface air temperatures across a city and its surrounding rural areas are plotted. This figure depicts air temperature in the Kansas City metropolitan area during a heatwave, with data being obtained from a climate model. Temperature values are taken from a north-south cross-section through the center of the city at a longitude of 94.6° W. The greatest temperatures are found in

the urban core of Kansas City, then decrease as you move outward into less built-up and rural areas. Examples of land cover at these approximate locations are also shown in Figure 1. Aforementioned differences in physical properties and anthropogenic activity between these types of land cover lead to this type of warming pattern.

1.2 Urban heat island health risks

Over the past 30 years, extreme heat has been the leading cause of weather-related mortality in the United States (National Weather Service 2019). One reason that it is important to study excessive heat in urban areas is that temperatures are exacerbated in these areas. As noted in the prior section, the UHI effect tends to become strongest at night because impervious surfaces release built-up heat from the absorption of shortwave radiation during the day. Therefore, as rural areas begin to cool as the sun sets, temperatures are maintained at a greater magnitude within the city during that time. As a consequence, those living in urban areas have a shorter period of time at night that their bodies are able to recover from the extreme daytime temperatures, increasing their risk of suffering from a heat-related illness (Environmental Protection Agency 2006; Luber and McGeehin 2008; Laaidi et al. 2012). During the 2003 European heat wave that was responsible for over 70,000 deaths in Europe (Robine et al. 2008), approximately 50% of the heat-related deaths in West Midlands, England could be contributed to the UHI effect (Heaviside et al. 2016). In a separate study that analyzed the 2003 European heat wave, researchers found that in Paris, the probability of mortality during the heat wave increased with two main factors, i.e. 1) minimum temperatures during the heat wave and 2) the average minimum temperature the day of and six days prior to their death (Laaidi et al. 2012). Since minimum (i.e. nighttime) temperatures were significant indicators of death risk, this

illustrates how excessive heat in urban areas can exacerbate outcomes during heat waves since UHIs are strongest during the late evening and night.

1.3 Social disparity and urban heat islands

As the amount of research on UHIs has grown over time, it has been found that not all individuals in cities are affected to the same extent. Harlan et al. (2006) found that those who are affected most by the UHI effect in Phoenix, AZ tend to be minorities and those of lower socioeconomic status. These individuals also tended to live in areas with greater population density, less open space, and lower amounts of vegetation. The urban conditions that the authors found contributed to the heat stress experienced in Phoenix align well with the aforementioned causes of UHIs. First, greater population density and reduced vegetation indicate that surfaces are likely covered with greater amounts impervious surfaces, e.g. concrete and asphalt, which will reduce the amount of moisture that is able to be absorbed into the soil and increase the thermal inertia of the land cover. Other studies have also found this to be an important factor when investigating the relationship between vegetation and heat stress inequality (Jenerette et al. 2011; Shiflett et al. 2017; Crum et al. 2017). Second, the combination of less open space with greater population density and reduced vegetation reveals that there are likely a higher density of buildings in these areas, leading to reduced air flow near the surface. Third, the amount of heat produced by anthropogenic activities, e.g. driving vehicles, would be greater in locations with more people. The authors also found that people living in areas that experience greater heat stress have less resources to help them cope with the greater temperatures (e.g. fewer social resources, air conditioners, and homes with swimming pools.

Mitchell and Chakraborty (2018) performed a similar study, but analyzed 20 metropolitan statistical areas throughout the United States and compared differences exposure to urban heat between racial/ethnic groups. Similar to above, the authors determined that areas with lower socioeconomic status had greater exposure to urban heat than those in higher income areas. They also found that non-Hispanic blacks and Asians were 52% and 32%, respectively, more likely to live in areas with greater exposure to heat-risk related land cover compared to whites, while Hispanics were 21% more likely to live in these areas than whites.

CHAPTER 2. UHI MITIGATION

In order to reduce the UHI effect, and therefore heat-related illness and mortality, multiple mitigation strategies have been researched and implemented. These strategies can include things such as applying solar reflective paint to urban surfaces and growing more vegetation within cities. Although these methods are different in the mechanism in which they function, they have the same overall goal, i.e. reduce temperatures within cities. In this section, a brief overview of the surface energy budget will be provided, then different methods to reduce urban heat will be introduced.

2.1 Surface energy budget

UHI mitigation strategies aim to alter the surface energy balance, which describes the conservation of energy at Earth's surface (AMS 2012), and is represented by the equation

$$R_n = G_0 + H + \lambda E, \quad (1)$$

where R_n is the net radiation flux and G_0 , H, and, and λE are the ground storage, sensible, and latent heat fluxes, respectively (Su 2002). Sensible heat flux is the transfer of energy between the surface and atmosphere without a change in phase of a substance, and latent heat flux is the energy released or absorbed when a substance changes phase, e.g. change from liquid water to water vapor (Oke et al. 2017). Ground storage heat flux is the net flow of energy through the ground (Lund et al. 2017).

The surface energy balance for a typical urban surface is depicted in Figure 2a. After incoming shortwave radiation interacts with the surface, different processes will take place. Since moisture is limited in impervious surfaces, the latent heat flux is relatively small compared to sensible and ground heat fluxes. Impervious surfaces with a low albedo, which are typical in urban areas, also absorb a majority of the incoming solar radiation, preventing it

from being reflected back toward the sky. These two factors lead to most of the solar energy to be partitioned into sensible and ground heat fluxes, leading to increased local temperature in these areas. Methods that are commonly employed to reduce urban heat alter these processes occurring at the surface.

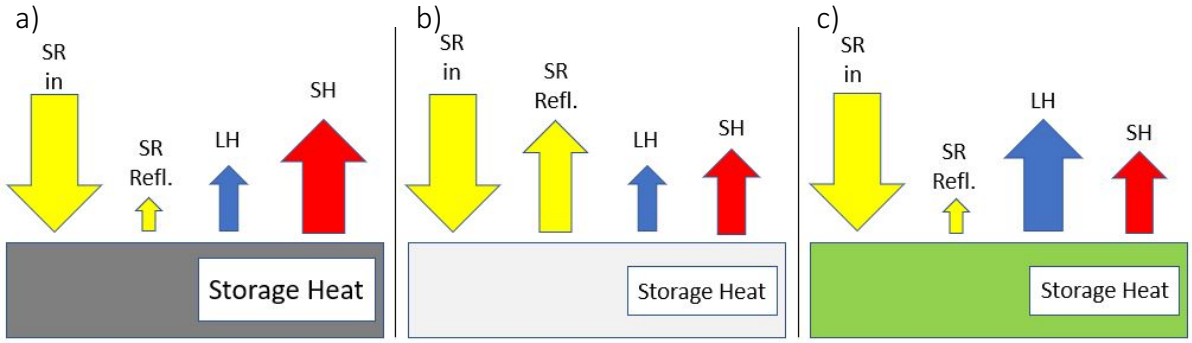

Figure 2. Latent, sensible, and storage heat fluxes for a) typical, low-albedo asphalt, b) a cool surface, and c) green and pervious surfaces. SR in = incoming solar radiation, SR Refl. = reflected solar radiation, LH = latent heat, and SH = sensible heat. Not drawn to scale.

2.2 Cool surfaces

2.2.1 Cool surfaces background

Most UHI mitigation strategies can be subdivided into two major categories, the first of which that will be discussed here are cool surfaces. Cool surfaces, which includes cool roofs, walls, and pavements, alter the energy balance by changing the albedo of a surface (Santamouris et al. 2011). A diagram of the underlying mechanism for of this type of method is shown in Figure 2b. By reflecting more radiation than typical urban surfaces, sensible and storage heat fluxes are reduced, thereby reducing temperatures within the city. Since moisture is not being added to the urban surface, latent heat remains relatively unchanged. Examples of

cool roof materials include paints, metal and shingle roofs, and single-ply membranes (Santamouris et al. 2011), while examples of cool pavement includes pavement coloring additive, reflective paint, and a thin layer of concrete over low-albedo asphalt (Santamouris 2013).

In order to be certified as a cool roof product, many building codes require that the product be tested and certified by specific organizations (Environmental Protection Agency 2008). At this time, there are multiple testing methods and measurements that are utilized to classify a roof as being a cool product. One of the most important measures in rating these roofs is the albedo. One commonly used entity that is used to test and certify these products is ENERGY STAR®. For low-sloped roofs, ENERGY STAR requires the initial albedo to be at least 65% (or 0.65), and it must remain greater than or equal to 50% (or 0.5) after three years (ENERGY STAR 2020). In contrast, the California Energy Commission, has opted to use a combination of solar reflectance and thermal emittance in order to classify cool roofing materials (Urban and Roth 2010). Thermal emittance is a property of a material that describes the efficiency in which it will emit longwave radiation. An example of a cool roof is shown in Figure 3.

Figure 3. Example of cool roofs on residential structures (Cool Roof Rating Council 2016).

2.2.2 Cool roof literature

Regional climate models, such as the Weather Research and Forecasting Model (WRF), are one method that has often been utilized in investigating the potential for UHI mitigation strategies, including cool roofs, to reduce the UHI effect. In a study by Zhang et al. (2017), the authors investigated the effect of implementing cool roofs in the Yangtze River delta in China over a 73 day period in 2013 using the WRF model with a single-layer urban canopy model (SLUCM). For their control simulation, the albedo of roofs in the study area remained at the default of 0.2. For their two experimental simulations, the roof albedo was increased to 0.5 and

0.7. They discovered that in the higher albedo experiments, surface skin temperature and 2-m air temperature (T2) were reduced over this time frame compared to the control. Interestingly, near-surface relative humidity increased, which they contributed to an increase in specific humidity and decreased air temperature.

In an article from Ma et al (2018), the authors completed a similar study, but also compared their results using three heat stress indices, including simplified wet-bulb globe temperature, apparent temperature, and humidity index. These heat stress indices take into account air temperature and humidity in order to provide a representation of how a person would perceive these conditions. The simulations in this study were focused over Sydney, Australia for a one-month period during each of the summers of 2007, 2008, and 2009. They also kept their control simulation roof albedo at 0.2, and chose to use a cool roof albedo of 0.64, which they noted was the median value from multiple other studies. For their results, they found a reduction in near-surface air temperature by up to 0.8-1.2^{o}C during the midday with the deployment of cool roofs, but had little change in vapor pressure between the scenarios. These effects led to a decrease in all three heat stress metrics compared to the control throughout the day, translating to improved human thermal comfort with cool roof implementation.

Vahmani et al. (2016) performed one of the few long-term studies on this topic. Their area-of interest focused on Southern California, and the time frames of their analyses included present-day, mid-21st-century, and end-of-21st-century. Future simulations were performed for both RCP2.6 and RCP8.5 conditions. The cool roof albedo in this study, i.e. 0.4, was lower than the prior two manuscripts mentioned above, which the authors noted was due to “aging” of the roofs through deposition of pollutants over time. They also noted that homeowners prefer

darker roofs to support the use of 0.4-albedo cool roofs. The results showed that cool roofs were effective in countering the current UHI effect by reducing urban air temperature by an average of 0.9^{o}C during the month of July for the present-day analysis. This mitigation strategy showed a similar effectiveness during the mid-century simulation (RCP 8.5), but for the end-of-century simulation (RCP 8.5), cool roofs become less capable of mitigating the UHI effect. The authors warned that cool roofs will only continue to be effective for the next few decades unless steps are taken to reduce future greenhouse gas emissions.

Georgescu et al. (2014) also investigated the UHI phenomenon using future scenarios, which they accomplished by inputting projected urban land cover data that was obtained from the Environmental Protection Agency's Integrated Climate and Land Use Scenarios (EPA 2009) into the WRF model. In contrast to the other articles referenced above, the authors utilized a larger grid spacing, i.e. 20 km, so they could analyze the impact of cool roofs on a national level. Similar to other aforementioned studies, they found a reduction in two-meter air temperature with widespread deployment of cool roofs, which ranged from -0.4^{o}C to -1.80^{o}C depending on the location in the U.S. Interestingly, it was also noted that precipitation along the East Coast was reduced by as much as 2 mm/day during the summer with the increase in roof albedo. Other research has shown that along with reduced local temperatures, planetary boundary layer height and vertical mixing can also be decreased with the deployment of cool roofs (Sharma et al. 2016), which may have affected precipitation in the study by Georgescu et al. (2014).

2.3 Green roofs

2.3.1 Green roof background

A second method to mitigate the UHI effect includes green roofs, where soil and vegetation are installed on a building's roof (Figure 4). Although the goal is the same as cool roofs, i.e. decrease urban temperatures, the underlying mechanism to accomplish this goal is different (Figure 2c). With green roofs, energy from solar radiation is absorbed by water molecules on Earth's surface, which allows for liquid water to be converted to water vapor. When the liquid water is excreted from plants, this process is called transpiration, but for water from other sources, e.g. the soil, it is referred to as evaporation. When discussing the two processes in conjunction, it is referred to as evapotranspiration. After undergoing a change in phase from liquid to gas, the water molecules become airborne, taking with them the absorbed energy from Earth's surface, causing a drop in local air temperature. Figure 2c shows that due to the increase in evapotranspiration with vegetated surfaces, the latent heat flux is increased, leading to a reduction in the sensible and ground heat fluxes, and therefore, air temperature.

In addition to affecting temperature, green roofs have also been shown to reduce storm water flow volumes, decrease air pollution, and reduced building energy consumption (Mentens et al. 2006; Rowe 2011; Jaffal et al. 2012). One drawback for green roofs is that they require a more complex installation compared to cool roofs to protect the structure. In addition, since some water will be retained within the soil on the roof instead of directly running off, the load that a roof is able to withstand becomes an important factor to consider when designing a green roof. It has been estimated that green roofs can weigh approximately 73-122 kg/m^2 (Snodgrass and Snodgrass 2006).

Figure 4. Example of a green roof on Chicago's City Hall (Inhabitat 2006)

2.3.2 Green roof literature

Since green roofs are not the focus of this thesis, a more general overview of their effects from climate modeling studies will be provided compared to cool roofs, focusing on near-surface air temperature and heat stress indices. Of the articles reviewed, the impact of green roofs on near-surface air temperature ranged from a reduction of 0.12°C to 2.4°C compared to each study's respective control simulation. Seven articles noted having a maximum decrease in T2 between 1-2°C during the day (Zhang et al. 2017; Imran et al. 2018; Ma et al. 2018; Georgescu et al. 2014; Li et al. 2014; Carvalho et al. 2017; Sun et al. 2016), while only two saw a maximum decrease over 2°C (Georgescu 2015; Chen and Zhang 2018). The remaining four studies saw more modest benefits with less than 1°C reduction in urban temperatures (Liu et al. 2018; Yang et al. 2016; Sharma et al. 2016; Yang and Bou-Zeid 2019). In the article by Yang & Bou-Zeid (2019), they found that in three of the six cities studied, i.e. Chicago, IL, Miami, FL, and Phoenix, AZ, there was no difference between the green roof

simulations and control. In contrast, Yang et al. (2016) had previously identified a 0.7°C decrease in near-surface air temperature in Phoenix, AZ with widespread use of green roofs, and Sharma et al. (2016) found a reduction of 1.0°C in UHI intensity in Chicago, IL using this mitigation strategy.

Since green roofs act to increase the latent heat flux, thereby causing atmospheric moisture to rise, heat stress indices are an important aspect to consider when studying this strategy. The heat stress indices in the articles that utilized these measures consisted of the simplified wet-bulb globe temperature (SWBGT), apparent temperature (AT), and humidity index (HUMIDEX). Sun et al. (2016) reported a decrease of 1.7°C in AT in the Greater Beijing Area, and Ma et al., (2018) found that AT, SWBGT, and HUMIDEX were reduced by 0.6°C, 0.2°C, and 0.6°C, respectfully. To illustrate the importance of using these measures with green roofs, Ma et al. (2018) noted having a slight increase in heat stress in the morning using SWBGT even though the near-surface air temperature was less than the control simulation at that time.

2.4 Objective

The objective of this study is to investigate the UHI and the potential for mitigating this phenomenon in the KCMA. First, a suite of climate model sensitivity simulations will be performed in order to determine the best-performing set of physical parameterizations to be used in subsequent simulations. Next, the change in UHI size and magnitude will be evaluated by comparing climate model output using present-day and historical land cover data. By performing these simulations, I will be able to objectively analyze the impact of expanding impervious surfaces in this region. Lastly, the potential impact of cool roofs in mitigating the UHI effect will be investigated by comparing model output from a control simulation to output

from two scenarios that involve widespread deployment of cool roofs. In one of these scenarios, the albedo of roofs will be increased to 0.8 in order to simulate the impact of "newly-installed" cool roofs with a high albedo.. The second scenario will employ a roof albedo of 0.5, which will indicate the performance of cool roofs after they have "aged" over a period of time from deposition of atmospheric particulates on these surfaces.

CHAPTER 3. METHODOLOGY

3.1 WRF and simulation parameterizations

In order to accomplish the aims of this study, the Weather Research and Forecasting model will be utilized (version 3.9.1.1). WRF is a state-of-the-art mesoscale numerical model developed by the National Center for Atmospheric Research (Skamarock et al. 2008). WRF will be coupled with a single-layer urban canopy model (SLUCM) (Kusaka and Kimura 2004; Kusaka et al. 2001), which is depicted in Figure 5. The SLUCM accounts for sensible heat fluxes from multiple urban surfaces, including roofs, walls, and roads. Street canyons are parameterized within the model to represent urban geometry, allowing for building shadows and reflection and trapping of radiation (Chen et al. 2011). Up to three urban land cover intensities are able to be specified in WRF's SLUCM, allowing for a more realistic representation of a city's landscape. The coupling of WRF and the SLUCM has successfully been used in prior studies to analyze the impact of cool roofs on the UHI effect in other urban areas (Zhang et al. 2017; Sharma et al. 2016; Ma et al. 2018).

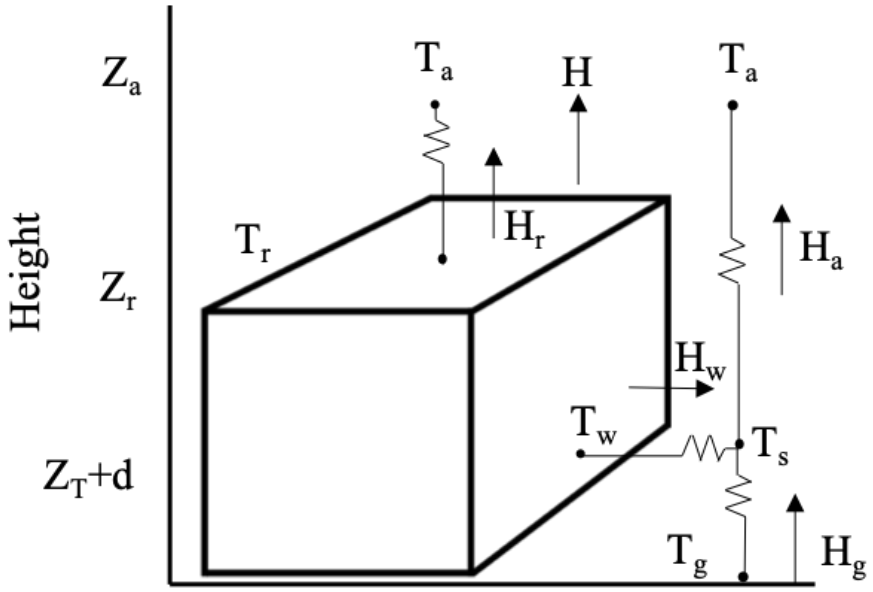

Figure 5. Depiction of the single-layer urban canopy layer. T_a is the air temperature at a given height Z_a. Subscripts w, r, and g indicate values of sensible heat (H) and temperature (T) from walls, roads, and ground, respectively. T_s is the temperature at the height of Z_T+d. Adapted from Kusaka and Kimura (2004).

To represent climate processes that occur at scales smaller than that of model domains' resolutions, parameterizations are utilized. A suite of WRF parameterization sensitivity experiments are performed first to obtain a set of parameterizations that yield the most accurate results, which will be then used in the subsequent portions of this study, i.e. historical and cool roof simulations. As a starting point for this portion of our study, relevant literature was reviewed to determine commonly utilized parameterizations in UHI-relevant climate modeling research. Those which provided adequate results were then included in our sensitivity simulations. Parameterizations that were varied in these simulations include shortwave and longwave radiation, planetary boundary layer, and surface layer. The specific schemes that

were analyzed are shown in Table 1. Parameterizations that were kept consistent for each simulation include land surface model, microphysics, and cumulus. The land surface model, i.e. Noah, was also unchanged because it is required when the SLUCM in employed. The Thompson microphysics and Grell-Freitas cumulus schemes were not varied because they handle atmospheric moisture and precipitation processes, which are of lesser concern during a heat wave where precipitation was not received, as was the case in this study. In addition, both Thompson and Grell-Frietas schemes have been commonly employed in other UHI studies (Vahmani and Jones 2017; Jeong et al. 2019; Cao et al. 2015; Imran et al. 2018; Tewari et al. 2019).

Table 1. Combinations of the different parameterizations tested for sensitivity MYJ = Mellor-Yamada-Janjic; BouLac = Bougeault-Lacarrère; ACM2 = Asymmetric Convective Model 2; MYNN2.5 = Mellor-Yamada, Nakanishi, and Niino Level 2.5; MM5 = fifth generation Mesoscale Model; RRTMG = Rapid Radiative Transfer Model for Global Climate Models; RRTM = Rapid Radiative Model; GFDL = Geophysical Fluid Dynamics Laboratory; CAM = Community Atmosphere Model.

Parameterization Combinations in Sensitivity Testing					
PBL/Surface Layer	**LW**	**SW**	**Microphysics**	**Cumulus**	**Land Surface**
MYJ/Eta					
	RRTMG	RRTMG	Thompson	Grell-Freitas	Noah
	RRTM	Dudhia	"	"	"
	RRTM	Goddard	"	"	"
BouLac/MM5					
	RRTMG	RRTMG	Thompson	Grell-Freitas	Noah
	RRTM	Dudhia	"	"	"
	RRTM	Goddard	"	"	"
	GFDL	GFDL	"	"	"
ACM2/MM5					
	RRTMG	RRTMG	Thompson	Grell-Freitas	Noah
	RRTM	Dudhia	"	"	"
	CAM	CAM	"	"	"
MYNN2/MM5					
	RRTMG	RRTMG	Thompson	Grell-Freitas	Noah
	RRTM	Dudhia	"	"	"
	CAM	RRTMG	"	"	"

3.2 Area-of-interest

The area-of-interest for this study is the Kansas City metropolitan area (KCMA), which is located in the Midwestern United States at the confluence of the Kansas and Missouri Rivers. This area aligns closely with the nine-county area defined by the Mid-America Regional Council (MARC), an association of local governments, as the MARC region. Counties within

this entity include Leavenworth, Wyandotte, Johnson, and Miami counties on the Kansas side and Platte, Clay, Ray, Jackson, and Cass on the Missouri side (Figure 6).

3.2.1 KCMA population

Jackson County, MO is the most populous county in the area (674,158 people), with Kansas City, MO being the city with the greatest population (491,918 people) (US Census Bureau 2018a). According to the Census statistics, the MARC region has grown from 1,919,089 people in 2010 to 2,055,405 in 2018 (+136,316). In a 2014 analysis, research showed that the this area is expected to gain nearly 322,000 people between 2010 and 2040 (this analysis did not include Ray County, MO) (MARC 2014).

3.2.2 KCMA land use and land cover

In order to support growth population over time, the amount of the UHI-contributing impervious surfaces, e.g. roads and parking lots, has also had to expand. Figure 6 reveals the increase in urban surface area that has occurred in the MARC region from 1990 to 2017 using classified Landsat imagery. Landsat images were obtained from the United States Geological Survey's Earth Explorer website at https://earthexplorer.usgs.gov/. In this 27-year period of time, a majority of growth has occurred in suburban areas on the periphery of the KCMA (indicated in black) where the core of this area (indicated in red) had been well established for some time.

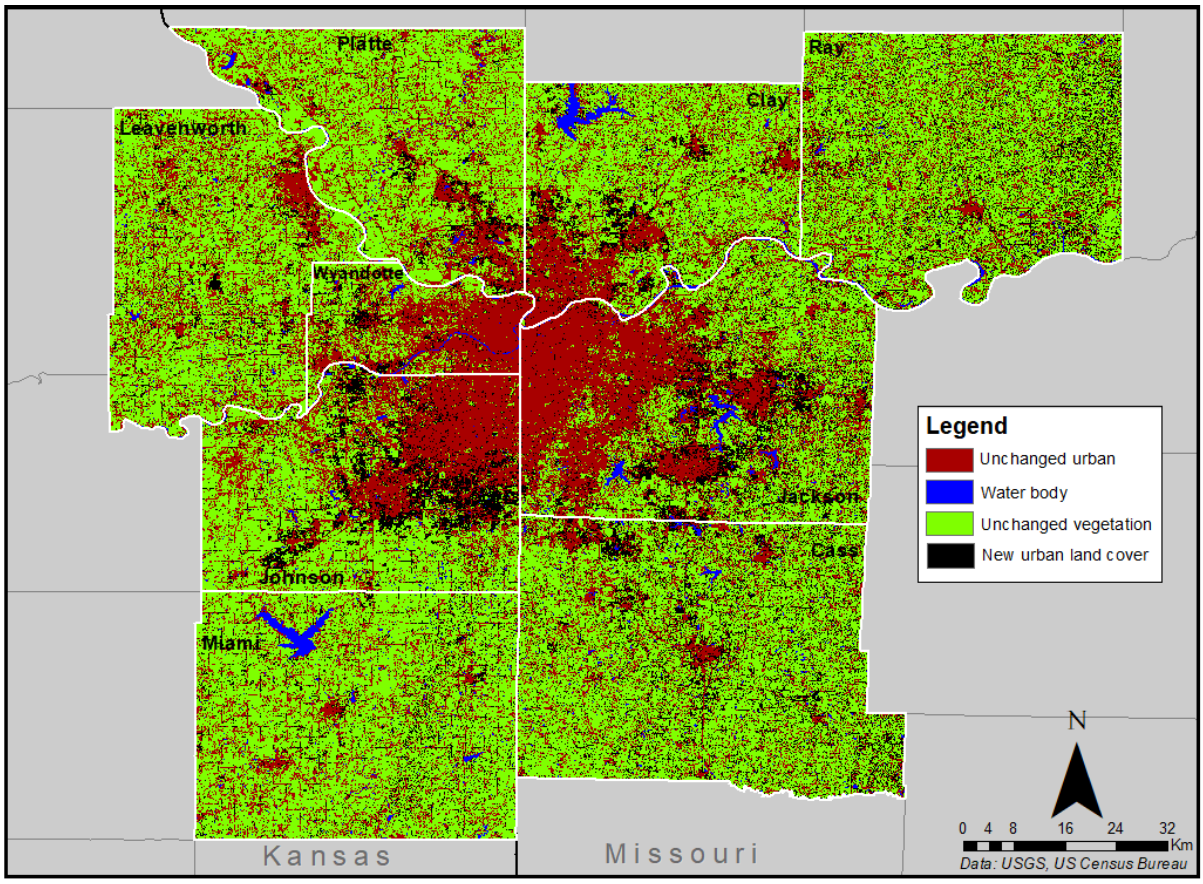

Figure 6. Change in extent of urban land cover in the MARC region from 1990 to 2017 using unsupervised classification of Landsat satellite images.

The extent of impervious surfaces in the MARC region from 2011 is shown in Figure 7 using NLCD 2011 Percent Developed Imperviousness data (Yang et al. 2018). The portion of the KCMA with the greatest density of built-up area is centrally-located where the Kansas and Missouri Rivers meet. The land use in this area largely consists of commercial and industrial purposes (MARC 2010). As one moves outward away from these districts, the density of impervious surfaces decreases as the number of single-family homes increases. From the aforementioned NLCD 2011 data set (Yang et al. 2018), there was approximately 732.22 km^2 of impervious surfaces within the MARC region in 2011. Jackson County, MO

and Johnson County, KS contain the greatest impervious surface area with 227.08 and 186.55 km^2, respectively.

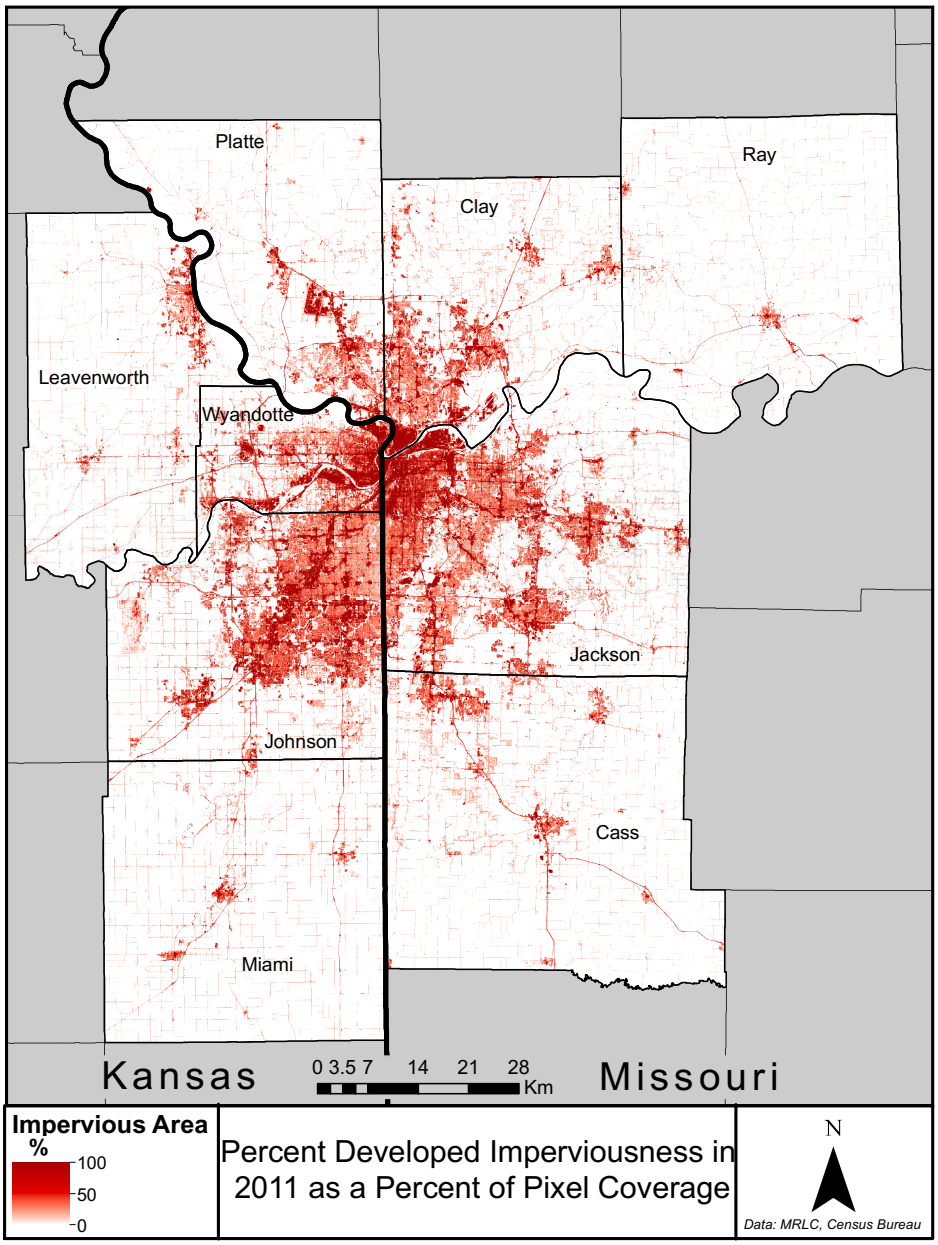

Figure 7. Amount of imperious surface area in the MARC region in 2016. Percentage is given as a percent of each pixel that is covered with impervious surface. Percent developed imperviousness is from the NLCD 2011 Percent Developed Imperviousness data set and has a grid-spacing of 30 m^2 (Homer et al. 2020).

The addition of impervious surfaces over time has contributed to the UHI effect in the KCMA. In 2014, researchers at Climate Central ranked Kansas City as having the seventh most intense UHI effect in the United States (Kenward et al. 2014). In their study, the authors compared weather data from urban and rural stations for all cities from 2003-2014 in order to determine the contrast in temperature between the two locations. For the KCMA, the average difference between urban and rural stations was 2.6°C. In the same study, this area also ranked 15th for the greatest overnight UHI effect.

3.2.3 KCMA climate

The Köppen climate classification describes the KCMA as being at the convergence of two climates, i.e. Dfa (humid continental, hot summer) and Cfa (humid subtropical, hot summer) (Christopherson and Birkeland 2015). Kansas City receives approximately 987 mm of precipitation annually, with a majority falling during the spring and summer months (Figure 8). Temperatures tend to peak during the summer in July, with monthly average and maximum temperatures of 25.7°C and 31.3°C, respectively (NCDC 2012). It is not uncommon for the maximum temperature to be greater than or equal to 37.8°C (i.e. 100°F) during the summer, with an average of three occurrences per year between 1981 – 2010 (NOAA 2020). With monthly temperatures reaching their lowest point in January with an average of -1.8°C, Kansas City has an average range in temperatures of 27.5°C during the year.

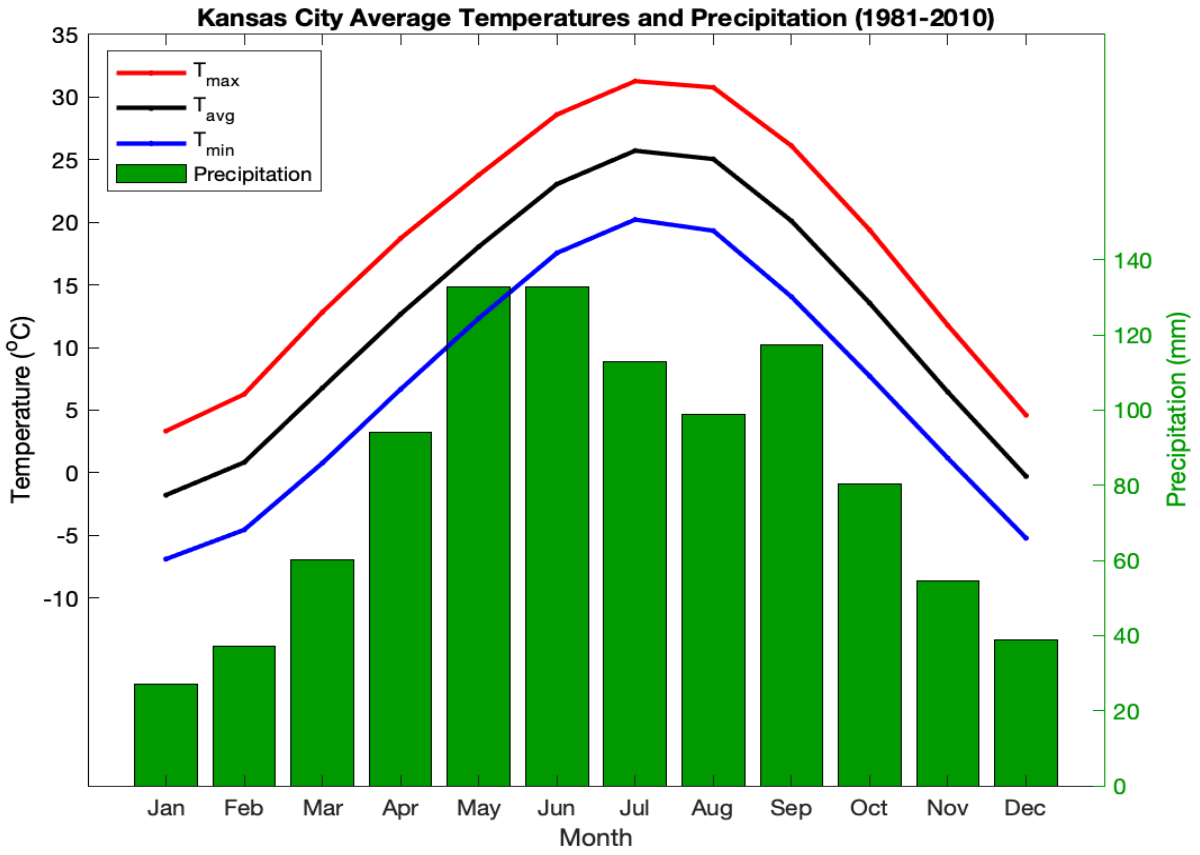

Figure 8. Climograph for Kansas City showing monthly average maximum temperature (T_{max}), temperature (T_{avg}), minimum temperature (T_{min}), and precipitation for 1981-2010. Measurements were taken at the Kansas City International Airport (National Climatic Data Center 2012).

This study focuses on a heat wave during the summer of 2012. During this period of time, many temperature and precipitation records were broken due to persistent heat waves and drought throughout the Great Plains (Climate Central 2012). Over the meteorological summer of 2012, the maximum temperature reached at least 37.8°C (100°F) on 20 separate days, which is a substantial contrast from the typical annual average of three days that the temperature meets or exceeds this threshold (NOAA 2020). In addition, this area received

126.5 mm of precipitation during that summer, which is nearly a third of the typical precipitation experienced during this period of time. One of the major reasons that extreme weather was experienced during the summer of 2012 was the presence of anomalous 500-hPa geopotential heights (Hoerling et al. 2014). In June, a high-pressure ridge over much of the West and Midwest kept cold fronts from tracking into the Great Plains. In July, an anticyclone remained over the northern Plains, again blocking fronts from moving into this region. Lastly, in August, a trough over the eastern half of the US hindered the influx of moisture into the Great Plains, which limited the amount of rainfall in the final full month of the summer. Abnormal sea surface temperatures in the north Atlantic and Pacific Oceans may have contributed to these conditions (Hoerling et al. 2014).

One advantage of performing simulations during a summer in which rainfall was limited is that changes in temperature with the deployment of cool roofs can be more definitively contributed to the roofs themselves rather than a combination of the mitigation strategy and cooling from the process of evaporation. A study by Husain et al. (2014) found that in Oklahoma City, OK, greater amounts of soil moisture led to a reduction in daytime heating within the city due to more energy being partitioned to latent heat flux instead of sensible heat flux. Therefore, during July 2012, extreme temperatures experienced were enhanced by the low soil moisture levels. Performing climate simulations during a hot and dry period of time also allows us to determine the maximum impact that can be expected from the use of cool roofs in the KCMA.

3.4 Model configuration

3.4.1 Domains

In order to effectively simulate the climate in this region, three nested model domains are utilized, each centered on the KCMA. From outermost to innermost, domain grid resolutions are 9, 3, and 1 km. Domain layout is shown in 8.Figure 9a along with the elevation of the outermost domain. Land cover of the innermost domain is presented in Figure 9b at 1-km resolution. Urban land cover is categorized into 3 different classes based on the density of impervious surfaces and include low-intensity residential, high-intensity residential, and industrial/commercial classes. Each domain also has 44 vertical levels between the surface and 100 hPa, with 21 layers within the first 1.5 km above the surface. Having a greater number of levels near the surface helps in resolving near-surface atmospheric processes, e.g. the planetary boundary layer. Only data from the innermost domain are analyzed from each simulation.

3.4.2 Land cover

Land cover for all three domains is represented by the National Land Cover Database (NLCD) 2011 (Homer et al. 2015), which is produced by the Multi-Resolution Land Characteristics Consortium. The NLCD 2011 is a land cover data set for the United States that consists of a spatial resolution of 30 m. It contains four different urban land cover categories, i.e. open space and low-, medium-, and high intensity, and the ranking of these categories are based on the amount of impervious surface covering the pixel area Since the SLUCM allows up to three urban land cover categories, the open space and low intensity urban classes were combined, as recommended by Tewari et al. (2007). This manuscript will follow the urban land cover naming convention of other studies, i.e. low-intensity residential, high-intensity residential, and commercial/industrial (listed in order from least to greatest impervious surface

density). NLCD 2011 was used for all simulations in this study except for the historical scenario.

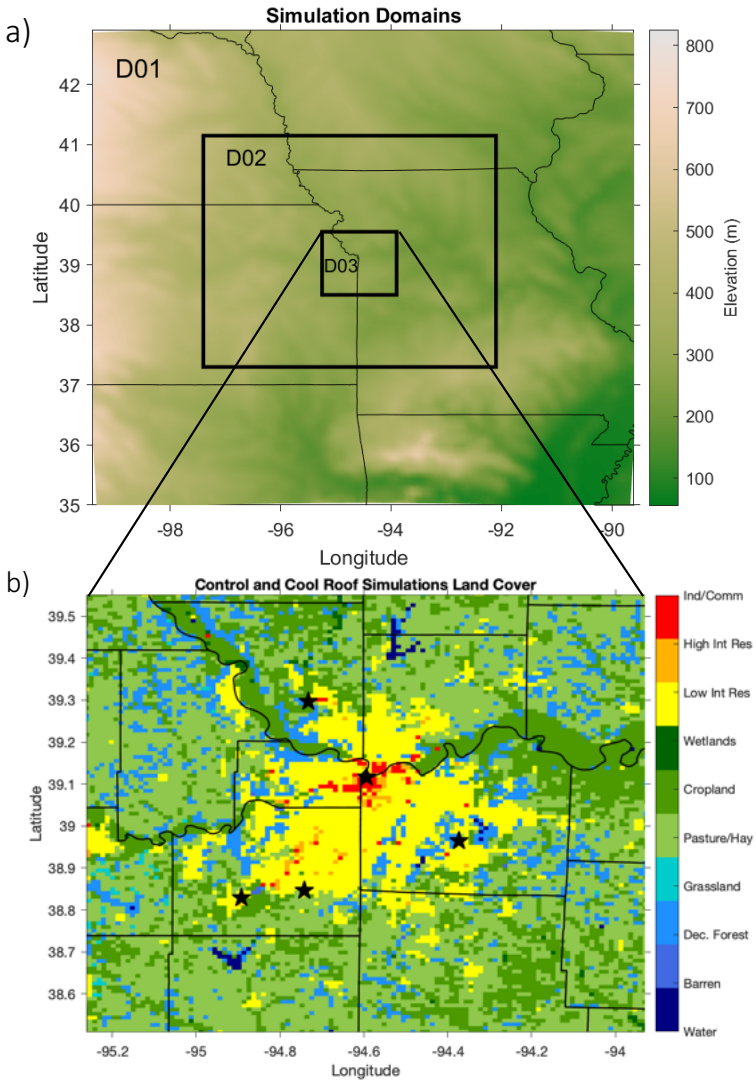

Figure 9. a) Configuration of three nested domains in the WRF simulations. Resolutions for domains 1, 2, and 3 are 9, 3, and 1 km, respectively. Elevation of the outermost domain is also provided. b) Land cover within the innermost domain at a resolution of 1 km. The three urban categories, in order from least to greatest impervious surface area, are low-intensity residential, high-intensity residential, and commercial/industrial. Black stars indicate locations of weather stations used for model validation.

Land cover for the historical simulation will employ a land cover data set that is representative of the year 1938 for the conterminous United States, which was created by the United States Geological Survey Earth Resources Observation and Science Center using the Forecasting Scenarios of Land Use (FORE-SCE) model (Sohl et al. 2016). The grid-spacing for this product is 250 m, and annual LULC data is available from 1938 to 1992. Only one urban land cover category is utilized within this data set, therefore all urban pixels were regarded as being "low-intensity residential" (Figure 10). Additionally, all land cover classes were matched to corresponding classes from the NLCD 2011, and were reclassified using GIS software.

3.4.3 Boundary and initial conditions

Boundary and initial conditions for the simulations were provided by the North American Regional Reanalysis (NARR) product, which is produced by National Centers for Environmental Prediction (Mesinger et al. 2005). The NARR dataset has a temporal resolution of 3 hours and a spatial resolution of 32 km. NARR is a long-term product, with data availability that extends from 1979 to present-day. Lateral boundary conditions for NARR are provided by the National Centers for Environmental Prediction-Department of Energy Global Reanalysis 2 general circulation model.

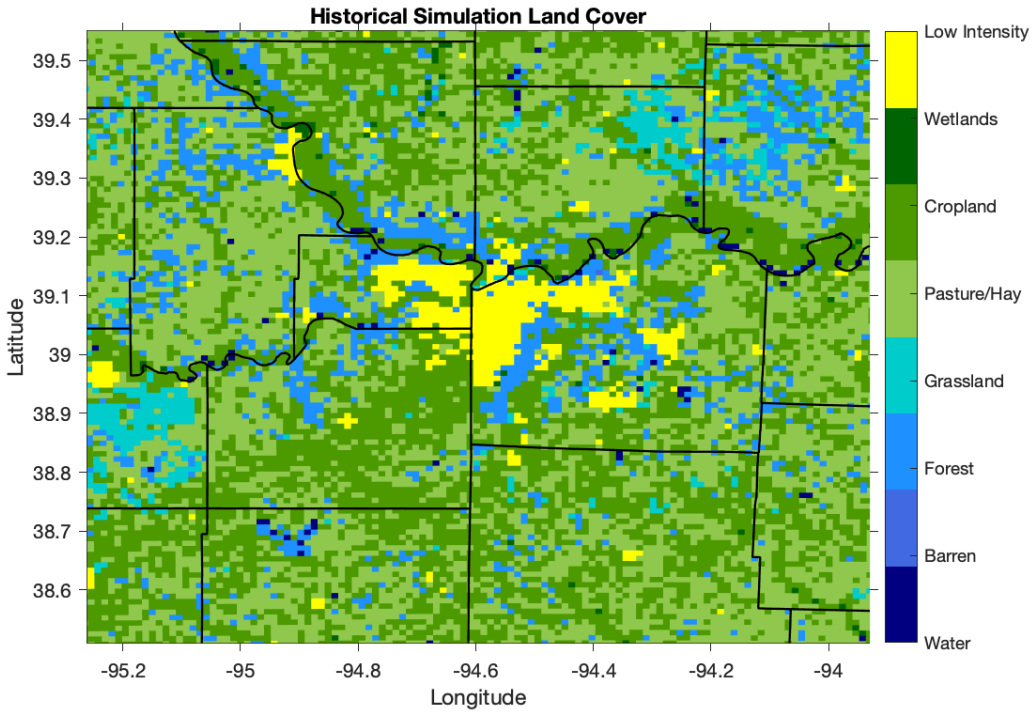

Figure 10. Land cover for the innermost domain of the historical simulation at a resolution of 1 km. All urban land cover is represented by one category, i.e. low-intensity residential.

3.4.4 Experimental design

A diagram depicting the time frame and characteristics of each simulation is presented in Figure 11. A suite of sensitivity simulations was conducted over a ten-day period from 15 July (1800 Local Standard Time (LST)) through 25 July (1500 LST) 2012. Previous testing from our lab had indicated that using a roof albedo of 0.3 led to a better estimation of 2-m air temperature (T2) than the WRF default of 0.2, so the roof albedo was tuned to 0.3 in these simulations. After the models are assessed for performance, the most accurate combination of parameterizations will be utilized in all subsequent simulations, which will all have a time frame of 18 July (0000 LST) to 24 July (2100 LST) 2012. Due to observed cooling effects from clouds in the innermost domain, the run time for all simulations after the sensitivity

experiments are narrowed down to a seven-day period (i.e. 18 – 24 July 2012) to ensure that changes in T2 in the cool roof simulations are from the mitigation strategy and not clouds. After the best-performing set of parameterizations is determined, a control simulation will be completed, which will be used to compare to three experimental scenarios. For the control, land cover will be represented by the NLCD 2011 data set and roof albedo will be 0.3.

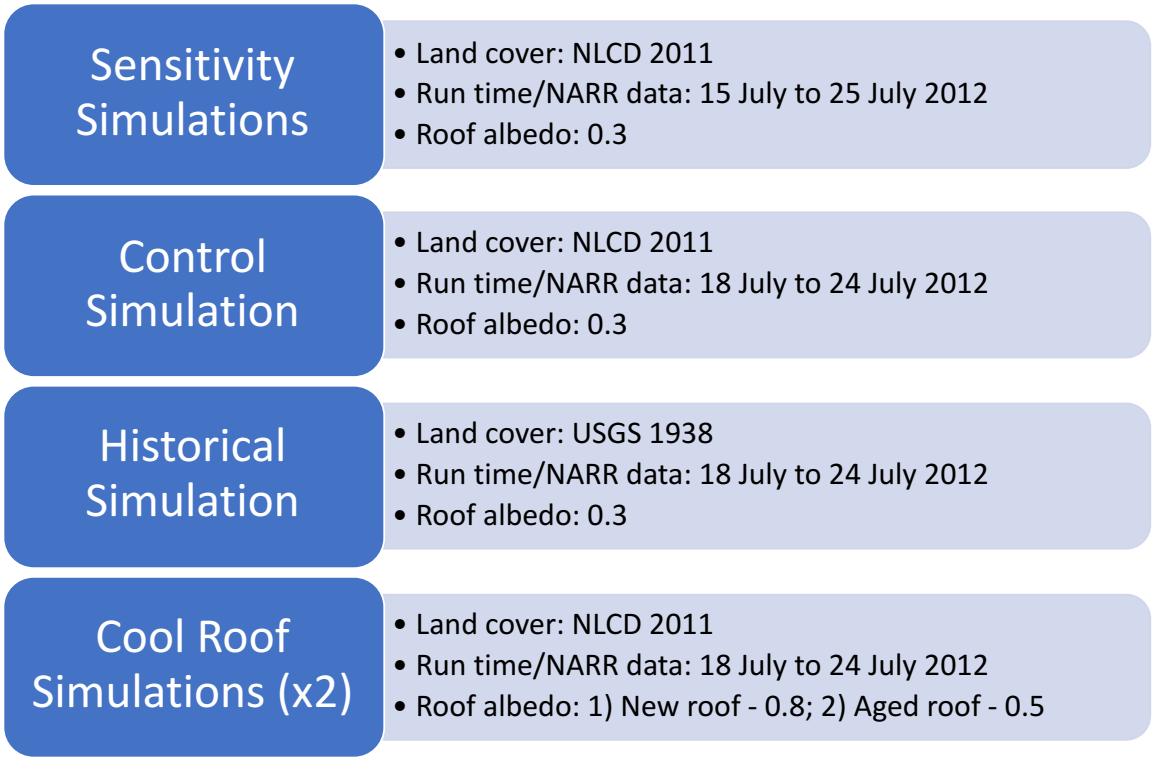

Figure 11. Depiction of the characteristics of each portion of this study. All simulations use NARR data from July 2012 for lateral and boundary conditions. All scenarios, except for the historical, will utilize the NLCD 2011 land cover. The historical case will employ land cover from the USGS for the year 1938. There are two cool roof simulations: the first uses a roof albedo of 0.8 to represent newly installed roofs, and the second has a roof albedo of 0.5, which indicates cool roofs that have been aged through deposition of dust and other particulates.

Next, three experimental simulations will be completed and compared to the control. First, the historical simulation will be performed, which will consist of the USGS land cover product that is representative of 1938, with roof albedo maintained at 0.3. Although it is named as the "historical" scenario, lateral and boundary conditions from the other present-day scenarios, i.e. NARR from 18 – 24 July 2012, will be utilized. This will allow for assessment of how the UHI effect has changed over the past approximately 74 years under equal weather conditions. The final two simulations will be used to represent UHI mitigation via widespread deployment of cool roofs through tuning of roof albedo. The first will depict the impact of newly-installed cool roofs with an albedo of 0.8. Over time, it has been shown that the reflectivity of these materials can be reduced through aging and weathering, such as deposition of airborne particulates (Akbari et al. 2005). In order to represent cool roofs that have been aged, the second mitigation scenario will employ roofs with an albedo of 0.5. This value also corresponds to the minimum albedo that a cool roof must maintain after three years to obtain ENERGY STAR approval (see Introduction for more information) (ENERGY STAR 2020). Road and building wall albedo remained at 0.3 for all conditions. Data from the first 48 hours of each simulation were excluded to account for model spin-up time.

CHAPTER 4. RESULTS

4.1 Evaluation of sensitivity simulations

Results from the suite of sensitivity tests are presented in Table 2. In total, 13 ten-day simulations were completed in order to determine the most accurate set of parameterizations for this study location. It has been recommended that a combination of outcome measures be used to evaluate models (Chai and Draxler 2014); therefore, WRF performance was based on three validation metrics, including root-mean-square error (RMSE), mean bias (MB), and mean absolute error (MAE). Observation data from five local airports were used for validation.

Table 2. Results from the suite of WRF sensitivity simulations. RMSE = root-mean-square error, MB = mean bias, and MAE = mean absolute error. Results are the average of all five weather stations.

Parameterizations			**Statistics**		
PBL/Surface Layer	**LW**	**SW**	**RMSE**	**MB**	**MAE**
MYJ/Eta					
	RRTMG	RRTMG	2.22	1.35	1.83
	RRTM	Dudhia	2.01	1.09	1.64
	RRTM	Goddard	2.27	1.61	1.91
BouLac/MM5					
	RRTMG	RRTMG	2.90	2.50	2.54
	RRTM	Dudhia	2.49	2.02	2.09
	RRTM	Goddard	2.91	2.57	2.59
	GFDL	GFDL	3.26	3.26	2.85
ACM2/MM5					
	RRTMG	RRTMG	2.28	1.98	1.98
	RRTM	Dudhia	2.08	2.02	1.70
	CAM	CAM	1.79	1.06	1.43
MYNN2/MM5					
	RRTMG	RRTMG	1.95	1.40	1.56
	RRTM	Dudhia	1.67	0.83	1.26
	CAM	RRTMG	1.74	0.39	1.40

Overall, measurements varied the greatest with different planetary boundary layer (PBL) and surface layer (SL) combinations. The PBL and SL parameterizations that exhibited the greatest RMSE, MB, and MAE was the BouLac and the fifth generation of the Mesoscale Model (i.e. MM5) schemes, respectively. Next, the Mellor-Yamada-Janjic/Eta and Asymmetric Convective Model 2/MM5 PBL/SL combinations performed slightly better and yielded similar results. The PBL and SL parameterizations that consistently provided the best outcomes are Mellor-Yamada, Nakanishi, and Niino Level 2.5 (MYNN2.5) and MM5, respectively, with all three statistical measures being found to be less than 2^{o}C. Within this group, the longwave and shortwave radiation that provided the best result is Rapid Radiation Transfer Model (RRTM) and Dudhia scheme, respectively. Based on the sensitivity testing, the following parameterizations were selected for use in subsequent simulations in this study: longwave and shortwave radiation were represented by the RRTM and Dudhia scheme, respectively; the MYNN2.5 scheme for the planetary boundary layer; MM5-similarity theory for the surface layer; microphysics were represented by the Thompson et al. scheme; and the Grell-Frietas scheme for cumulus parameterization. The cumulus parameterization was only used for the outermost domain (i.e. 9-km resolution) since these processes are able to be resolved at resolutions less than or equal to three km (i.e. that of the middle and innermost domains in this study) (Jeworrek et al. 2019).

Table 3. Validation of T2 using observation data from local airports, which are indicated by their FAA three-letter code. Root-mean-square error (RMSE), mean bias (MB), and mean absolute error (MAE) are calculated for each location, with the average of each statistic listed on the right. MKC = Charles B. Wheeler Downtown Airport, MCI = Kansas City International Airport, IXD = New Century AirCenter; LXT = Lee's Summit Municipal Airport, and OJC = Johnson County Executive Airport

	Control Validation Using Five Local Airport Stations					
	MKC	**MCI**	**IXD**	**LXT**	**OJC**	**Average**
RMSE (^{o}C)	1.28	1.81	1.54	1.58	1.49	1.54
MB (^{o}C)	0.69	1.22	0.77	0.05	0.50	0.65
MAE (^{o}C)	1.08	1.31	1.20	1.31	1.24	1.23

4.2 Evaluation of the control simulation

Using the aforementioned parameterizations, a seven-day (18 – 24 July 2012) control simulation was completed using a roof albedo of 0.3. The results from validation of the control are presented in Table 3 using the same five local airports as in the prior section. In evaluating model performance, average RMSE, MB, and MAE values were 1.54ºC, 0.65ºC, and 1.23ºC, respectfully, which are in agreement with results in the prior section. Results from each output time over the five-day period (first two days are not included to account for spin-up) are illustrated in Figure 12 using a scatterplot that compares local observed two-meter air temperature (T2) (x-axis) to WRF simulated T2 (y-axis). Results from each airport location appear to follow a similar pattern. First, for observed T2 values less than approximately 23ºC, WRF tended to slightly underestimate a small number of temperatures in this range (i.e. below the identity line). Between observed temperatures of 23 – 34ºC, simulated T2 values show a

relatively even distribution of values above and below the y = x line, but above 34ºC, WRF tended to slightly overestimate T2.

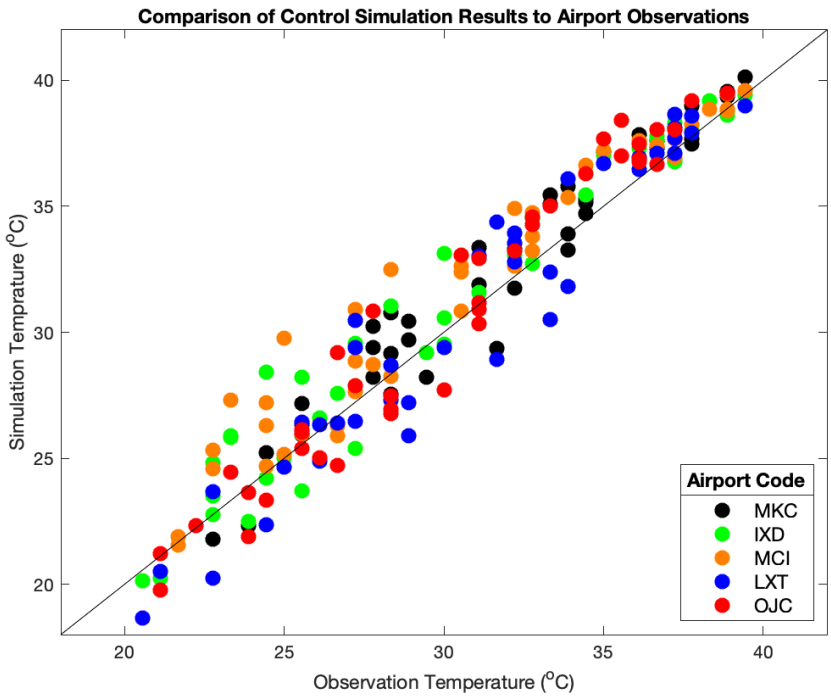

Figure 12. Validation of the control simulation using 2-m air temperature observations from five local airports. The locations of each airport are matched to the nearest pixel within the innermost domain (D03). Points within the plot are aligned vertically due to observation values being in integer format.

The UHI signal in the control case was investigated following validation. In order to calculate the magnitude of the UHI, the difference between urban and rural locations are found using the equation

$$T2_{UHI} = T2_U - T2_R \quad (1)$$

where $T2_{UHI}$ is the UHI magnitude and $T2_U$ and $T2_R$ are the urban and rural two-meter air temperature, respectively (Oke et al. 2017). Figure 13 contains the five-day average UHI

magnitude for each of the three urban land cover categories. In order to reduce the amount of influence of the urban area on temperature, rural pixels were only included if there were no urban pixels within 5 km in any direction. Areas with industrial/commercial and high-intensity residential land cover experience the greatest UHI effect at night during the 2100 and 0000 LST output times, with their magnitude reaching approximately 4^{o}C warmer than rural areas at that time. Locations that consist of low-intensity urban cover also reach their greatest extent at the same times, with a difference of approximately +1.5^{o}C. At 0900 and 1200 LST, the difference between all three urban land cover categories and rural pixels became slightly negative indicating that areas away from the KCMA were warmer than those within the city.

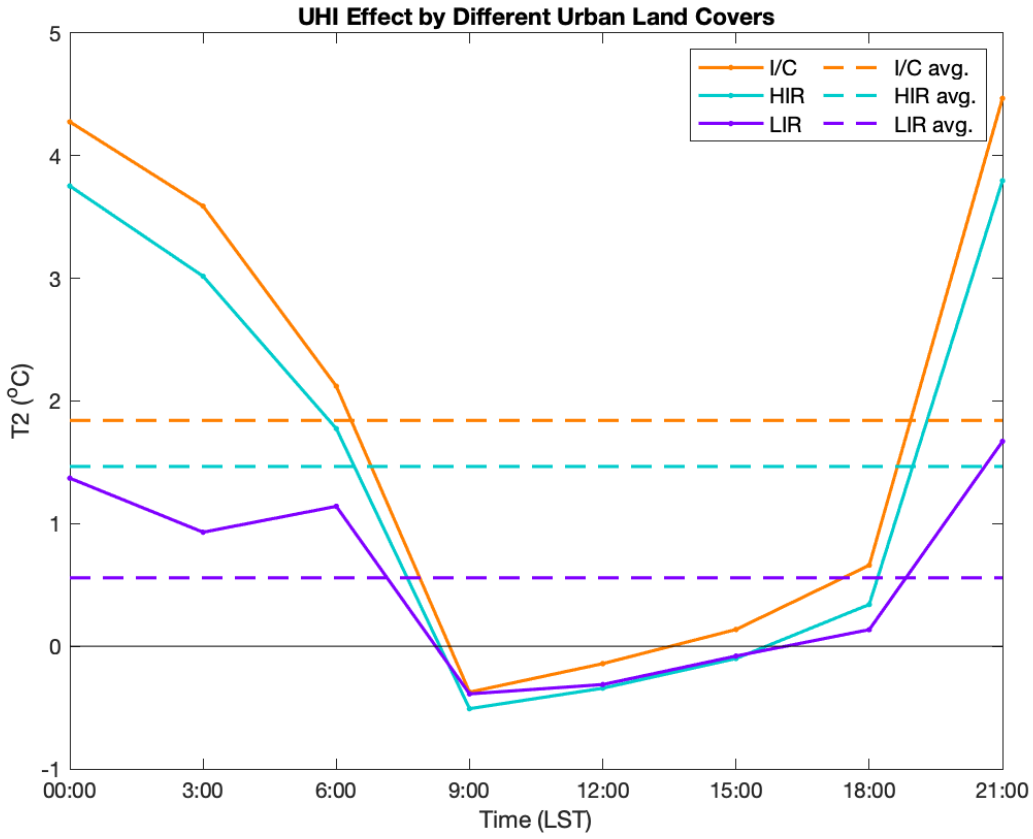

Figure 13. Near-surface UHI effect averaged over the five-day heat wave for every WRF output time in the KCMA. Results are shown for each urban land cover category separately. I/C = industrial/commercial, HIR = high-intensity residential, and LIR = low-intensity residential.

4.3 Comparison of control to historical simulation

The next step in this study was to compare the control to the simulation with land cover that was representative of 1938 in order to analyze the change in KCMA UHI over seven decades. Three-hourly output data from both simulations are presented in 13.Figure 14. T2 in both conditions were shown to be nearly equal in magnitude during the daytime hours. In contrast, at night, temperatures between the two simulations diverged, with the historical case

cooling to a greater extent. The greatest average difference between them came at 0000 LST, with a difference of 0.63°C. The average T2 difference over the five-day period was 31.25°C and 31.02°C for the control and historical simulations, respectively.

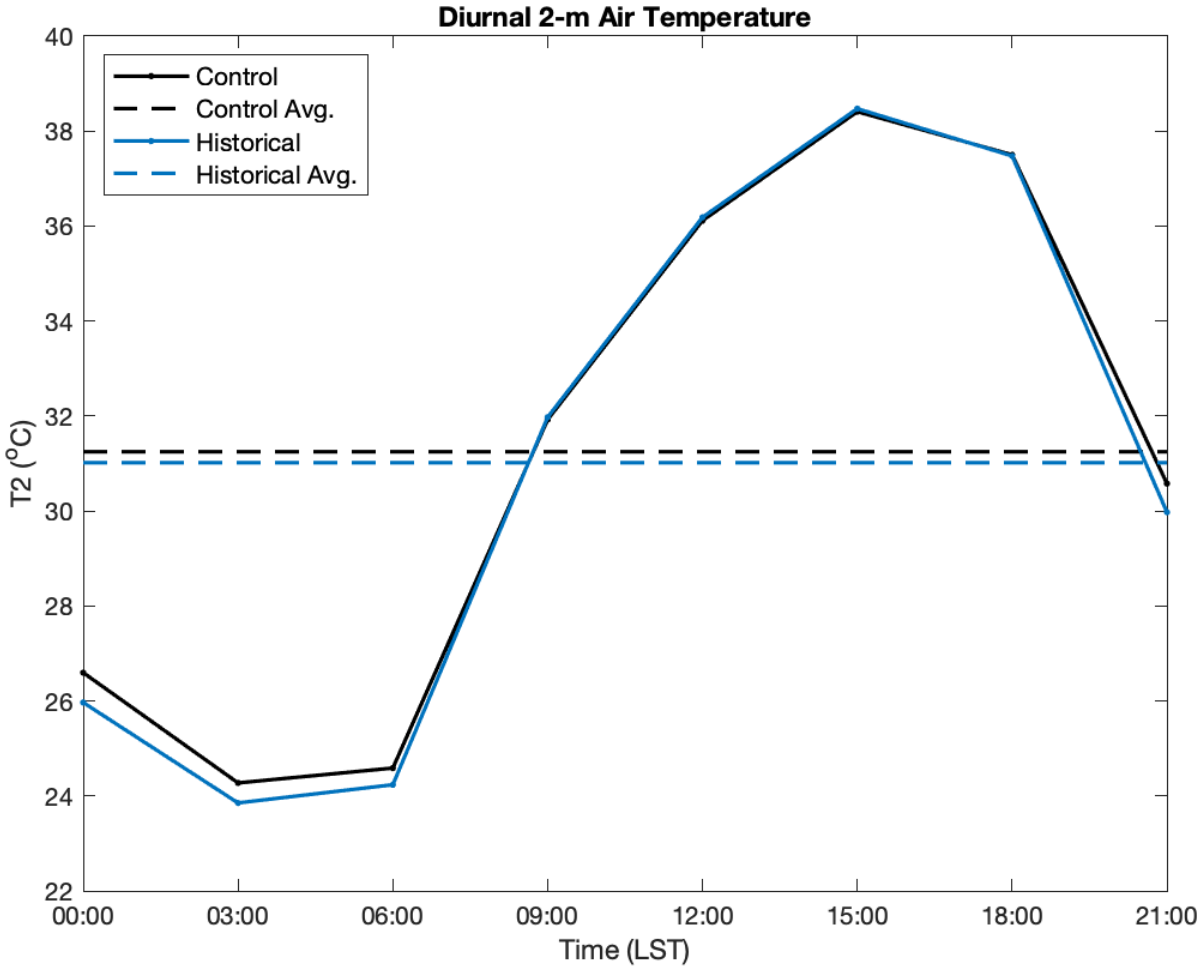

Figure 14. Control and historical simulation five-day time series of T2 with output data plotted every three hours. Average T2 for the entire time frame for both scenarios are shown as dashed line. Only urban values are used in calculations.

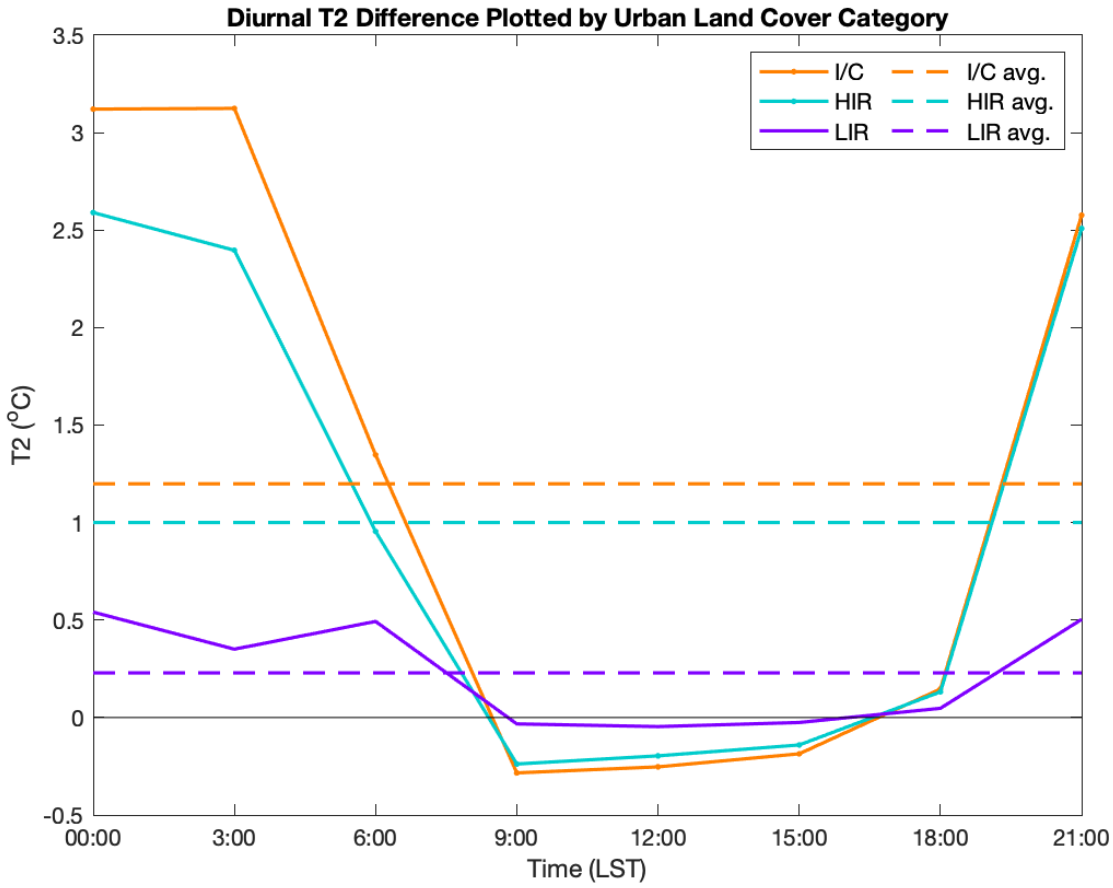

Figure 15. Five-day average T2 difference between historical and control simulations (control minus historical) for the three urban land cover categories. Values averaged over all output times are shown as dashed lines. Only urban values are used in calculations.

When T2 results are separated by urban land cover category, distinctions between these parts of the metropolitan area are revealed. Figure 15 compares the differences in T2 between the three urban classes from the present-day simulation to the corresponding low-intensity residential urban pixels in the historical case to display how temperature would have differed between the same locations during these two periods of time. For example, T2 values from industrial/commercial land cover pixels from present-day were compared to their analogous low-intensity residential pixels in the historical simulation. The same process was used for the

other two present-day urban land cover categories as well. If an urban pixel in 2011 was found to be non-urban in 1938, the T2 values from both data sets were excluded from the data presented in Figure 15 so that only results from urban locations were compared. Figure 15 reveals that during the daytime, average T2 values from the historical simulation were similar, and in some cases slightly exceeded, those that were modeled in the present-day simulation. In contrast, nighttime temperatures in the historical case were less than the present-day scenario, especially for the industrial/commercial and high-intensity categories (over 2.5^{o}C difference at 2100 and 0000 LST). Comparing the five-day average T2 difference in Figure 16 below, similar results are observed. The blue shape approximates the extent of the KCMA UHI in 1938, which is able to be distinguished by similar T2 values between the low-intensity residential pixels from both simulations (i.e. light red color within the blue shape). Locations with a darker red color within the blue shape indicate the impact of the higher intensity urban categories on T2 in 2012 compared to low-intensity residential land cover from 1938. The present-day UHI effect is approximated by the green shape. When these results are separated by output time in Figure A1 (Appendix), the increase in T2 is obvious from 2100 – 0600 LST, where T2 between 0900 and 1800 LST are relatively similar between the two simulations.

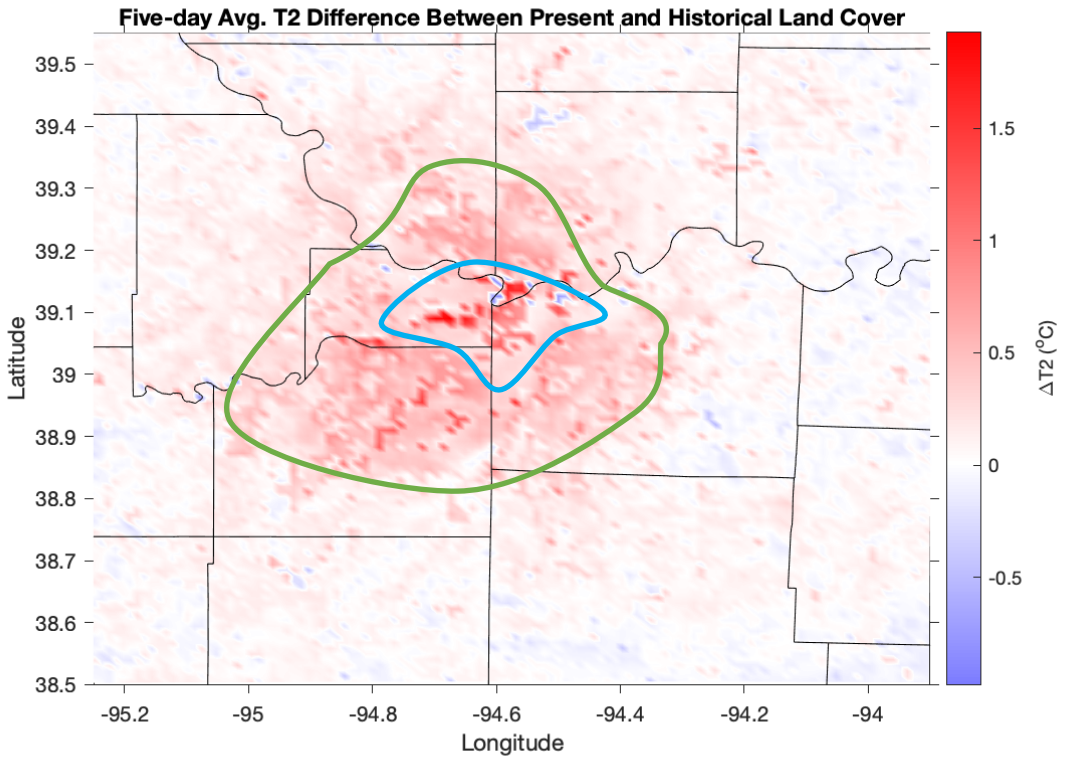

Figure 16. Map of the five-day average T2 difference between the historical and present-day simulations (control minus historical). Areas of the historical and present-day KCMA extent are approximated by the blue and green shapes, respectively.

4.4 Impact of cool roofs

4.4.1 Two-meter air temperature

The next step in this study was to run two cool roof simulations in order to investigate their impact on the excessive urban heat within the KCMA. When averaged over the entire study time frame, the 0.5- and 0.8-albedo cool roof cases were able to reduce urban T2 by approximately 0.2°C and 0.45°C, respectively (Figure 17). Both mitigation scenarios were able to mitigate urban temperatures throughout the day, with their greatest effect occurring at 2100 LST (-0.26°C) and 0900 LST (-0.57°C) for the 0.5- and 0.8-albedo simulations, respectfully. The spatial plots in Figure 18 show that these impacts were not equal throughout the city. Both

scenarios revealed that cool roofs had their largest impact in the industrial/commercial and high-intensity residential sectors within the KCMA, especially those areas located centrally. In the 0.8-albedo simulation, five-day average difference between industrial/commercial and low-intensity residential T2 was nearly 0.20°C (-0.62°C vs. -0.44°C), where there was a 0.06°C difference in the 0.5-albedo case (-0.24°C vs. -0.18°C). T2 spatial plots are also presented for three-hourly output times in the Appendix (Figure A2 and Figure A3). The difference in cooling via the use of cool roofs is able to be visualized throughout the KCMA during each model output time.

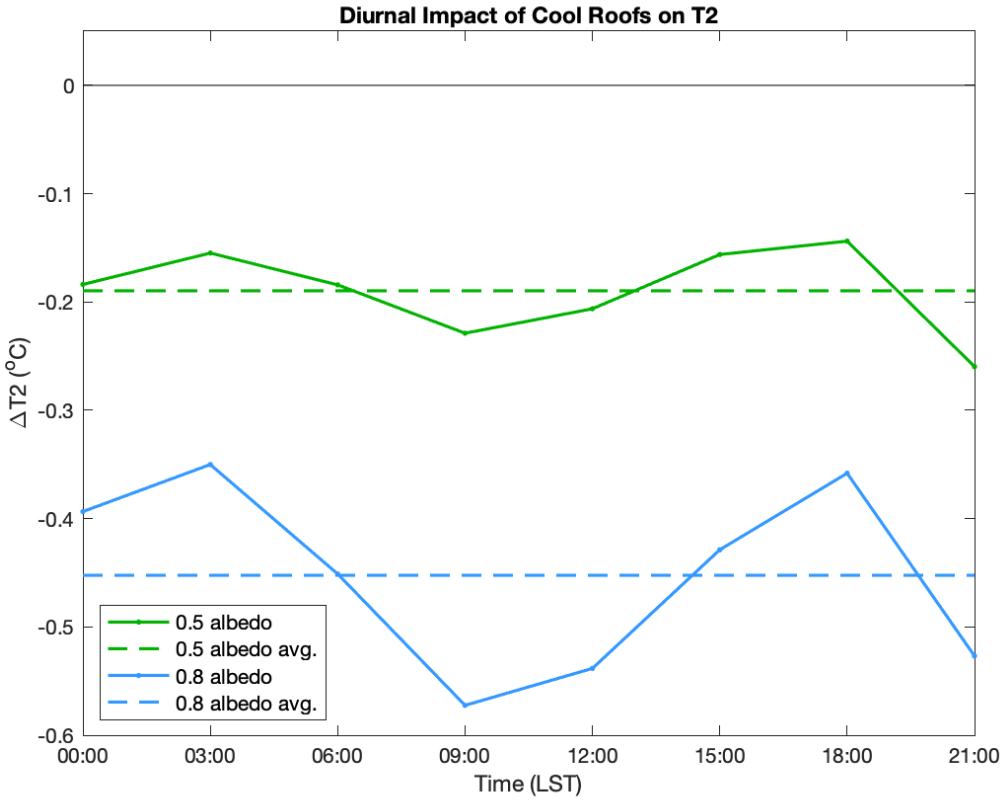

Figure 17. Impact of cool roofs on T2 in the KCMA (cool roofs minus control). Five-day average difference at each output time (solid line) is shown along with the average across all output times (dashed line). Only urban values are used in calculations.

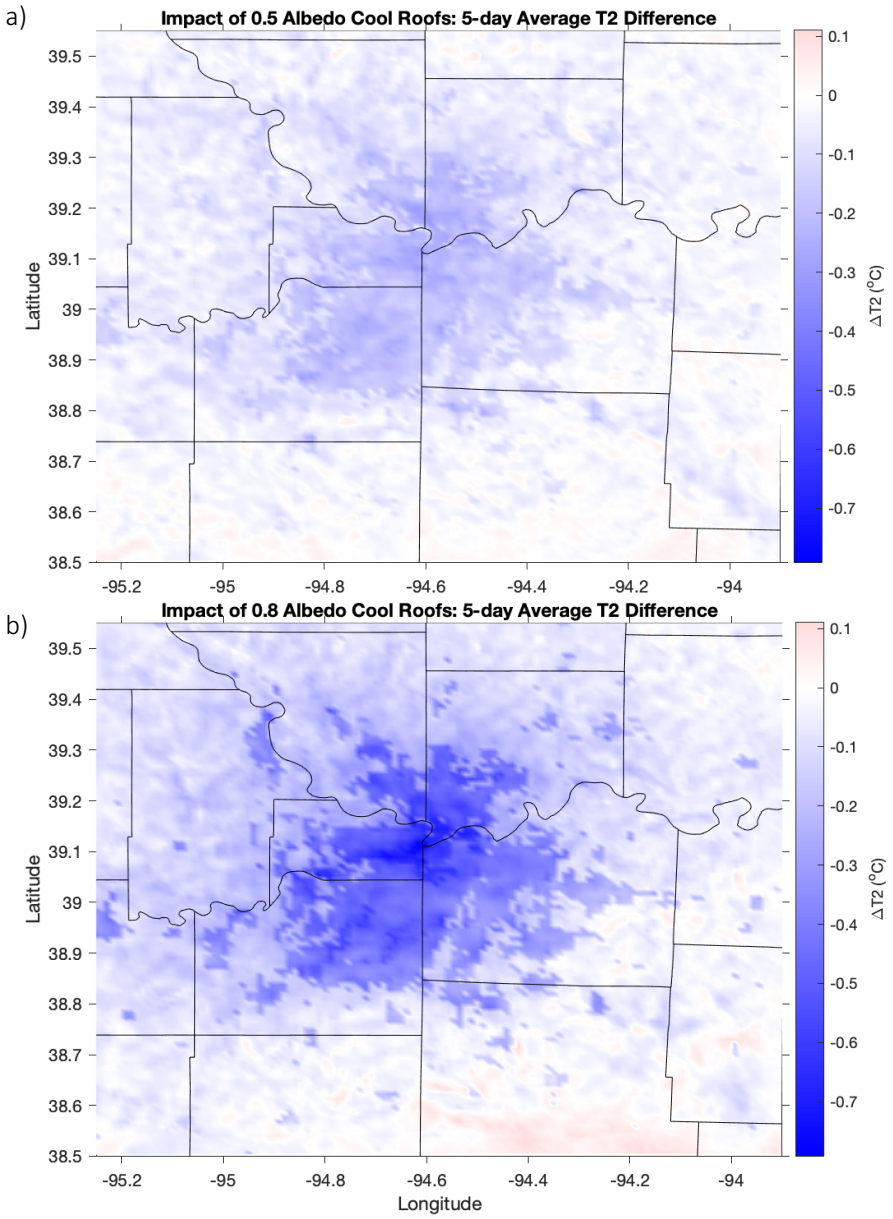

Figure 18. Difference in T2 between the a) 0.5-albedo and b) 0.8-albedo cool roof and control simulations. The color scheme in both figures are equal.

The bar graphs in Figure 19 reveal the UHI effect by taking the average T2 for each urban land cover category in each simulation and subtracting it by the average rural T2 at every

three-hour output time. The UHI effect occurs when the difference between the urban and rural pixels is positive, which was greatest at night at 2100 LST. At this time, the UHI effect was reduced by 0.26 – 0.28ºC for all urban categories in the 0.5-albedo simulation, and in the 0.8-albedo case, it was decreased by 0.51 – 0.64ºC. As the city cools during the night, the contrast in T2 lessens from 0000 LST to 0600 LST, but the three urban categories continue to display a reduction in the UHI effect in the cool roof simulations compared to the control. After the sun rises, the relationship between urban and rural areas switch, and rural locations become warmer than urban sites. At 1500 LST, industrial/commercial land cover began to exhibit the UHI effect in the control (0.3-albedo) simulation, but in both cool roof cases, all urban areas were still cooler than the rural parts of the domain. The UHI started to form during the 1800 LST output time for both cool roof simulations in the industrial/commercial (0.5- and 0.8-albedo simulations) and high-intensity residential (0.5-albedo only) categories. The UHI effect finally appeared in the remaining urban land cover categories by 2100 LST in the cool roof cases.

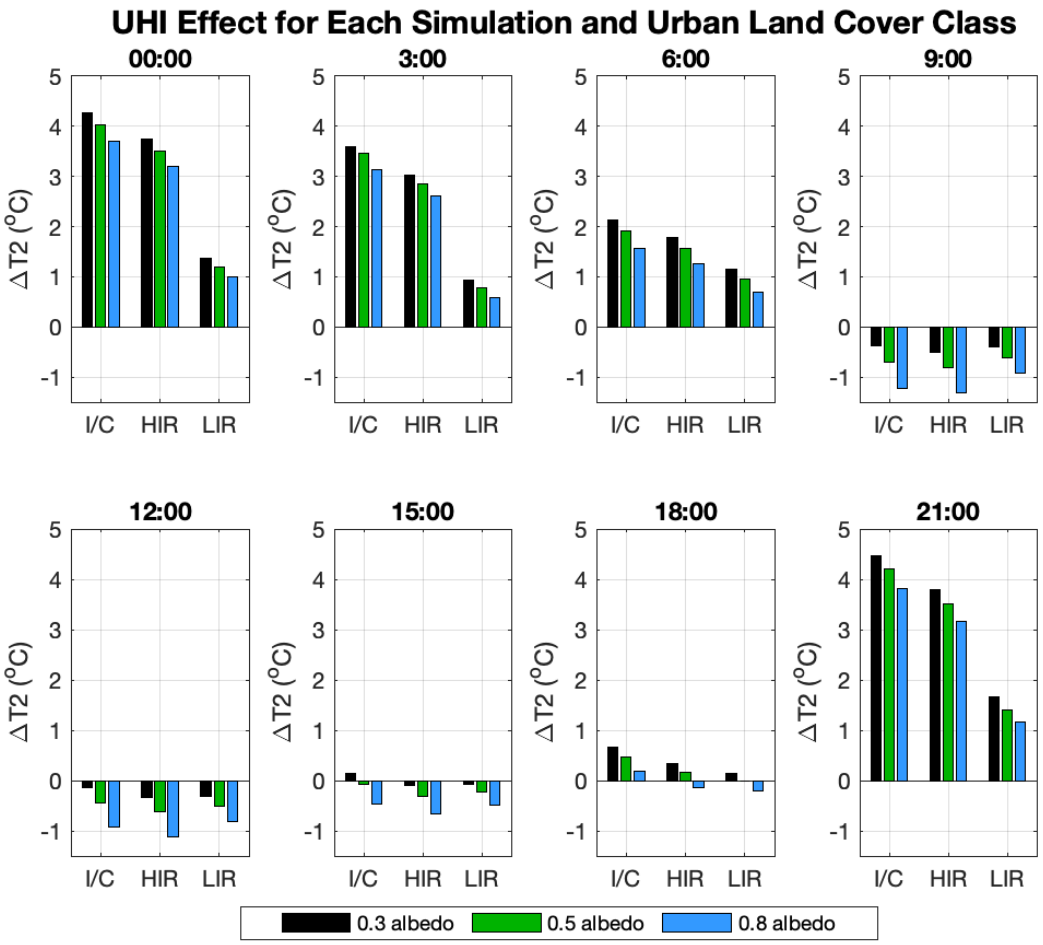

Figure 19. Magnitude of UHI effect comparing urban areas to rural locations (urban minus rural). Results are separated by WRF model output time. T2 data from rural pixels were included in the calculations if there were no urban pixels within five miles in any direction. Times are in local standard time.

The final step in assessing the effect of cool roofs on T2 was to investigate the statistical significance of the impact of cool roofs. Average five-day temperature for each urban pixel was included, which consisted of 75 industrial/commercial, 61 high-intensity residential, and 1,235 low-intensity residential pixels from each scenario. Hypothesis testing was carried out by first analyzing differences among simulations within each urban land cover category. Due

to having non-normal data distributions, the Kruskal-Wallis test was employed (Table 4). The null and alternative hypotheses were as follows:

$$H_0 : r_1 = r_2 = r_3 \quad (2)$$

$$H_A : r_1 \neq r_2 \neq r_3 \text{ or } r_1 \neq r_2 = r_3 \text{ or } r_1 = r_2 \neq r_3 \quad (3)$$

Due to the *p*-values being less than the α-value of 0.01, the null hypothesis was rejected, indicating that a significant difference exists among the three scenarios in each land cover class. Next, differences between roof albedo cases were assessed with the post hoc multiple comparison analysis test using Dunn's approach (Dunn 1961) in to avoid inflation of the type I error rate. The hypotheses for each multiple comparison test were as follows:

$$H_0 : \mu_a = \mu_b \quad (4)$$

$$H_A : \mu_a \neq \mu_b \quad (5)$$

The results show that within each land cover category, comparisons between the control, 0.5-albedo, and 0.8-albedo simulations are all statistically significant (α = 0.01), therefore the null hypothesis was rejected in each pairwise comparison (Table 5).

Table 4. Results from the Kruskal-Wallis test comparing average T2 among the three simulations (i.e. 0.5- and 0.8-albedo and the control), separated by urban land cover category ($\alpha = 0.01$).

Urban Category	***p*-value**
Industrial/Commercial	<0.0001
High Intensity Residential	<0.0001
Low Intensity Residential	<0.0001

Table 5. Results from the multiple comparison test using Dunn's approach comparing average T2 between pairs of simulations for each urban land cover category. The first two columns on the left indicate the groups that were compared in each test. The next three columns contain the p-values for each land cover category. $\alpha = 0.01$

Groups Compared		Results of Post-Hoc Multiple Comparison Test by Urban Category		
Group 1	**Group 2**	***p*-value; Industrial/Commercial**	***p*-value; High Intensity Residential**	***p*-value; Low Intensity Residential**
Control	0.5	<0.0001	<0.0001	<0.0001
Control	0.8	<0.0001	<0.0001	<0.0001
0.5	0.8	<0.0001	<0.0001	<0.0001

4.4.2 Skin temperature

The next variable to be evaluated from the models' output is skin temperature (TSK), i.e. the temperature of the ground surface. Figure 20 reveals the average three-hourly diurnal impact of cool roofs on TSK in the KCMA. The largest cooling effect was experienced at 1200 LST in both the 0.5- and 0.8-albedo simulations, providing a decrease in TSK of approximately 1.5°C and 3.6°C, respectively, at that time. When averaged over the entire five-day heat wave, surface temperatures were reduced by 0.69°C in the 0.5-albedo case, where the impact in the 0.8-albedo condition was -1.66°C.

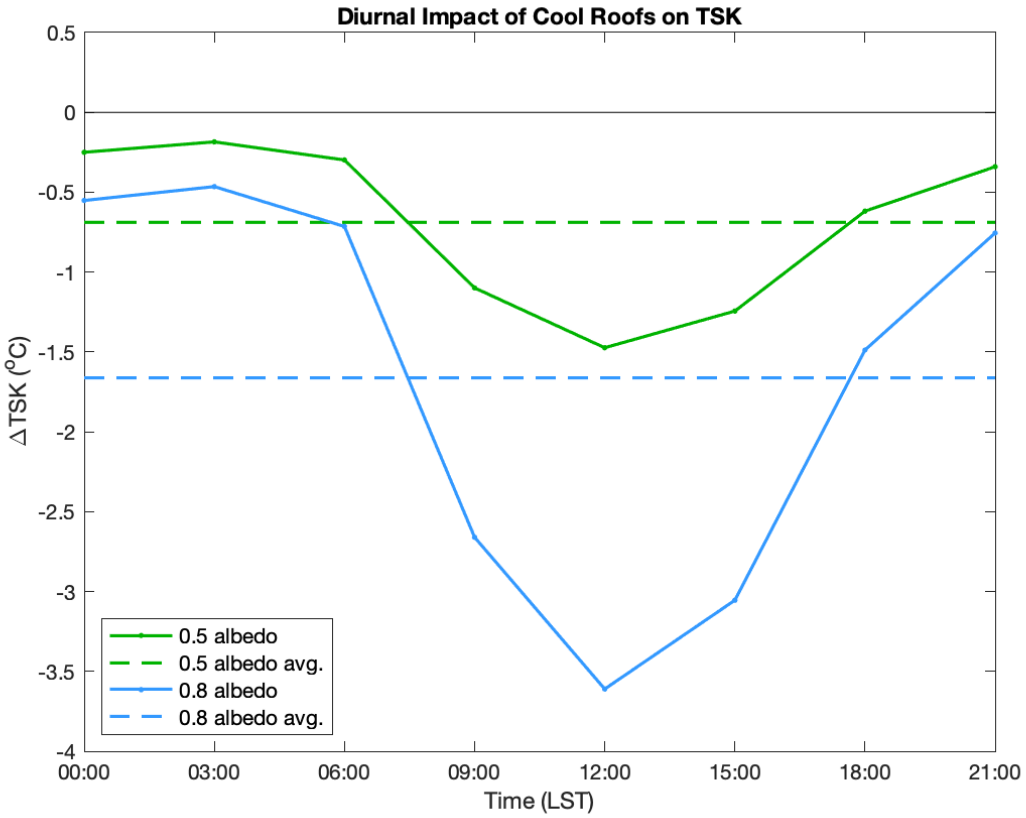

Figure 20. Average three-hourly impact of cool roofs on TSK for both the 0.5- and 0.8-albedo simulations. Dashed lines represent the five-day mean TSK difference, averaged across all output times. Only urban values are used in calculations.

In analyzing the average change in TSK with deployment of cool roofs spatially, differences in cooling within various parts of the KCMA are observed (Figure 21). Similar to T2, cool roofs had the biggest effect in the industrial/commercial and high-intensity residential areas. In these locations, TSK was reduced by up to approximately 1°C in the 0.5-albedo simulation and 2.5°C when the albedo was increased to 0.8. Low-intensity residential locations saw less of an impact compared to the more densely urbanized sites. In the three-hourly spatial

plots (Figure A4 and Figure A5), the greatest impact was observed at 1200 LST for both cool roof simulations, followed by a gradual reduction in cooling from 1500 – 0300 LST.

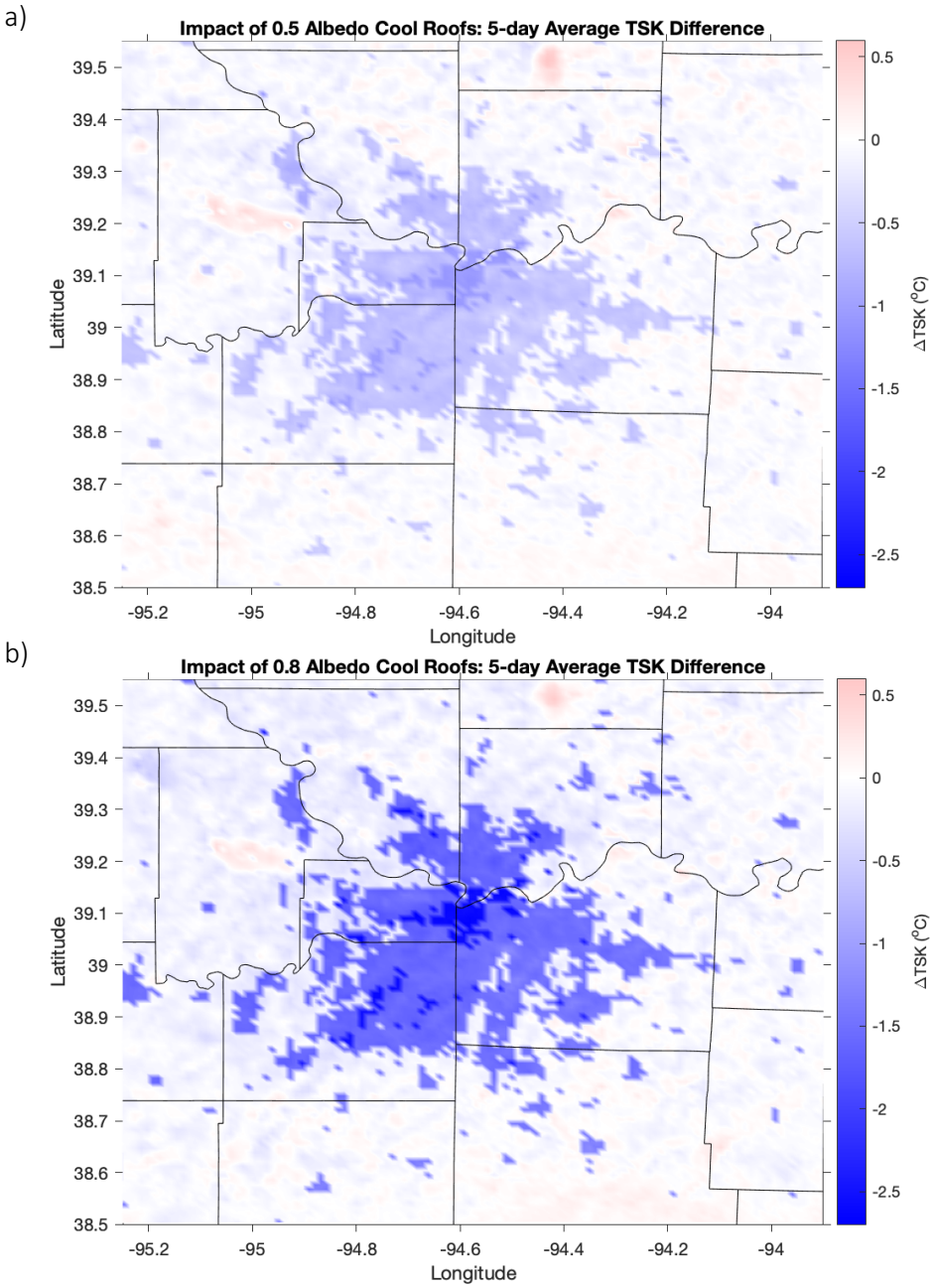

Figure 21. Difference in TSK between the a) 0.5-albedo and b) 0.8-albedo cool roof simulations and control. The color scheme in both figures are equal.

Similar to describing the UHI as a contrast in T2 between urban and rural locations, the same concept can be applied to TSK (i.e. the surface UHI). Figure 22 presents the surface UHI effect in the KCMA at each model output time, comparing TSK from the three urban land cover categories to rural TSK. The strongest surface UHI effect was experienced at both 2100 and 0000 LST, where temperatures in the industrial/commercial sectors were over 7^{o}C warmer than local rural areas (0.3-albedo simulation). After these times, this phenomenon weakened through 0600 LST. From 0900 to 1500 areas outside of the KCMA became warmer than those within it, which is indicated by negative ΔTSK values. During the midday, industrial/commercial and high-intensity residential pixels revealed a TSK difference of up to approximately -9^{o}C. At 1800 LST, as the surface UHI effect forms in all urban locations in the control and 0.5-albedo scenario, high- and low-intensity residential areas in the 0.8-albedo cool roof simulation are still cooler than rural sites.

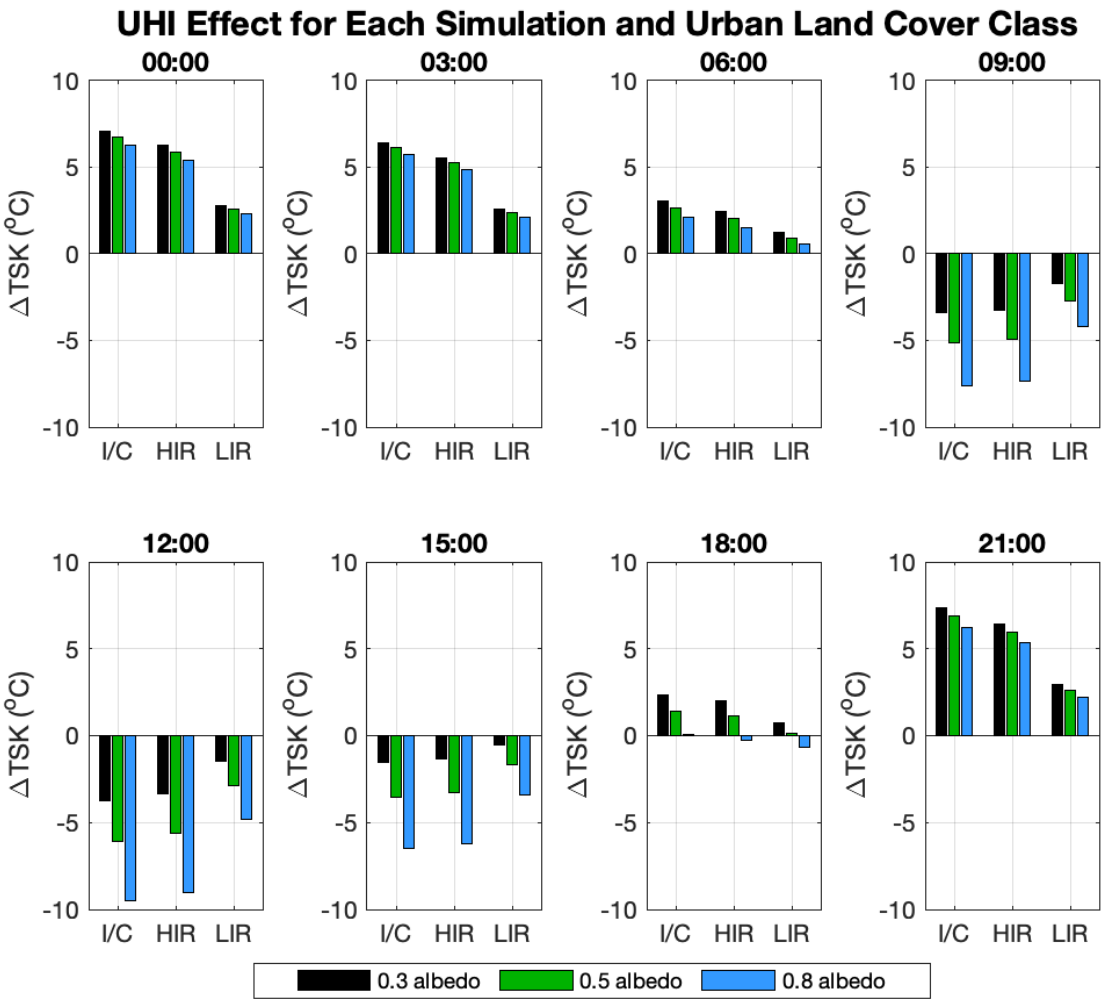

Figure 22. Magnitude of UHI effect comparing urban areas to rural locations. Results are separated by WRF model output time. TSK data from rural pixels were included in the calculations if there were no urban pixels within five miles in any direction. Times are in LST.

4.4.3 Surface energy balance

To better understand the impact of cool roofs on two-meter and skin temperatures, the surface energy fluxes were analyzed. The sensible heat (SH) flux in the control case reached 331.26 W/m^2 at 1200 LST, and was reduced by 39.62 W/m^2 and 95.67 W/m^2 in the 0.5- and

0.8-albedo simulations, respectively (Figure 23a). SH was also decreased at 0900, 1500, and 1800 LST, but to a lesser extent. During the nighttime, the SH between all three scenarios became approximately equal and negative (-20 – -5 W/m^2) from 2100 – 0600 LST. In contrast to SH, latent heat (LH) fluxes were nearly equal throughout the day for all three cases (Figure 23c). LH in the 0.8 simulation deviated slightly from the other two from 0900 – 1500 LST, ranging from 1.08 – 3.66 W/m^2 less than the control at these times. At these same output times, the ground storage heat flux (GH) was negative, indicating that more energy was being stored in the ground rather than released from it (Figure 23b). From 1800 – 0600 LST, the amount of incoming solar radiation was reduced, therefore there was a net release of stored energy from the ground, which is denoted by the positive GH at these times. Using Equation 1, SH, LH, and GH can be combined to reveal the net radiation (R_n) balance at the surface (Figure 23d). The plot of R_n follows a similar shape as that from SH, with the peak reaching 327 W/m^2, 292 W/m^2, and 241 W/m^2 for the control and 0.5- and 0.8-albedo simulations, respectively, at 1200 LST. Differences between scenarios became less pronounced during the nighttime compared to the day.

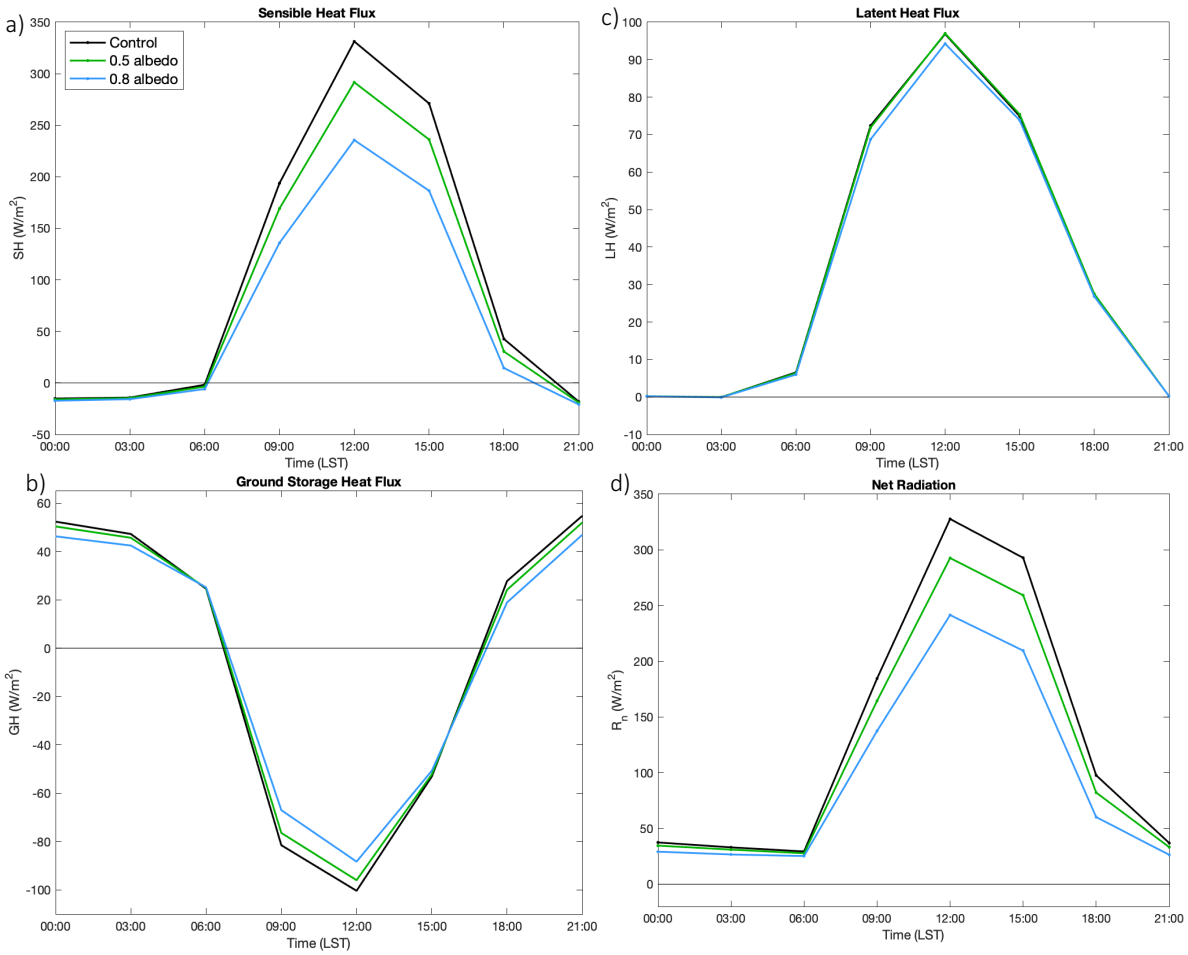

Figure 23. Average three-hourly a) sensible, b) ground storage, and c) latent heat fluxes for the control and 0.5- and 0.8-albedo simulations. d) Net radiation is also presented in the same format. Y-axes are not equal in range.

4.4.4 Water vapor mixing ratio

In comparison to the control simulation, both cool roof cases exhibited an increase in two-meter water vapor mixing ratio (Q2) within the KCMA from 0900 – 1800 LST (Figure 24). At the time of the greatest contrast, i.e. 1200 LST, the difference between the simulations was 0.16×10^{-3} kg/kg (0.5-albedo vs. control) and 0.35×10^{-3} kg/kg (0.8-albedo vs. control). At

other times of the day, values were approximately equal between the three scenarios. In the five-day average Q2 spatial plots, both the 0.5- (Figure 25a) and 0.8-albedo (Figure 25b) cases show an increase in atmospheric moisture over urban areas when compared to the control.

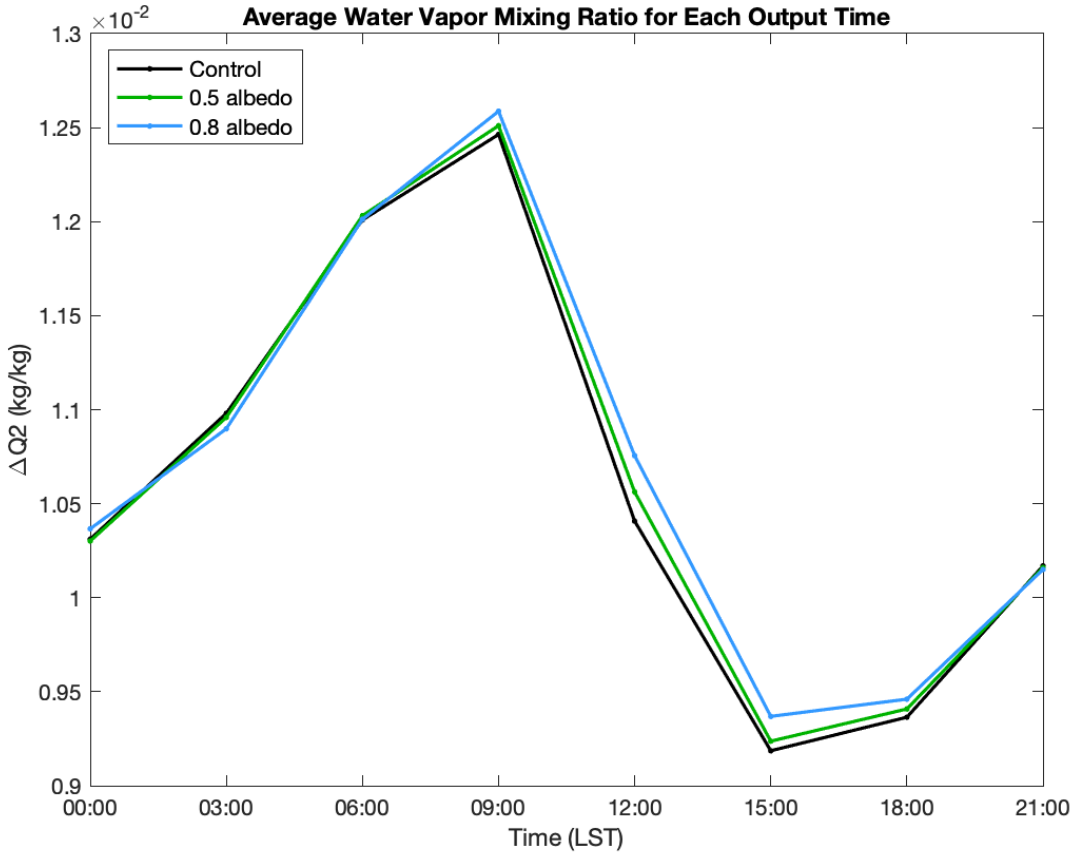

Figure 24. Diurnal average water vapor mixing ratio for all three simulations at each WRF model output time. All y-axis values are $\times 10^{-2}$. Only urban values are used in calculations.

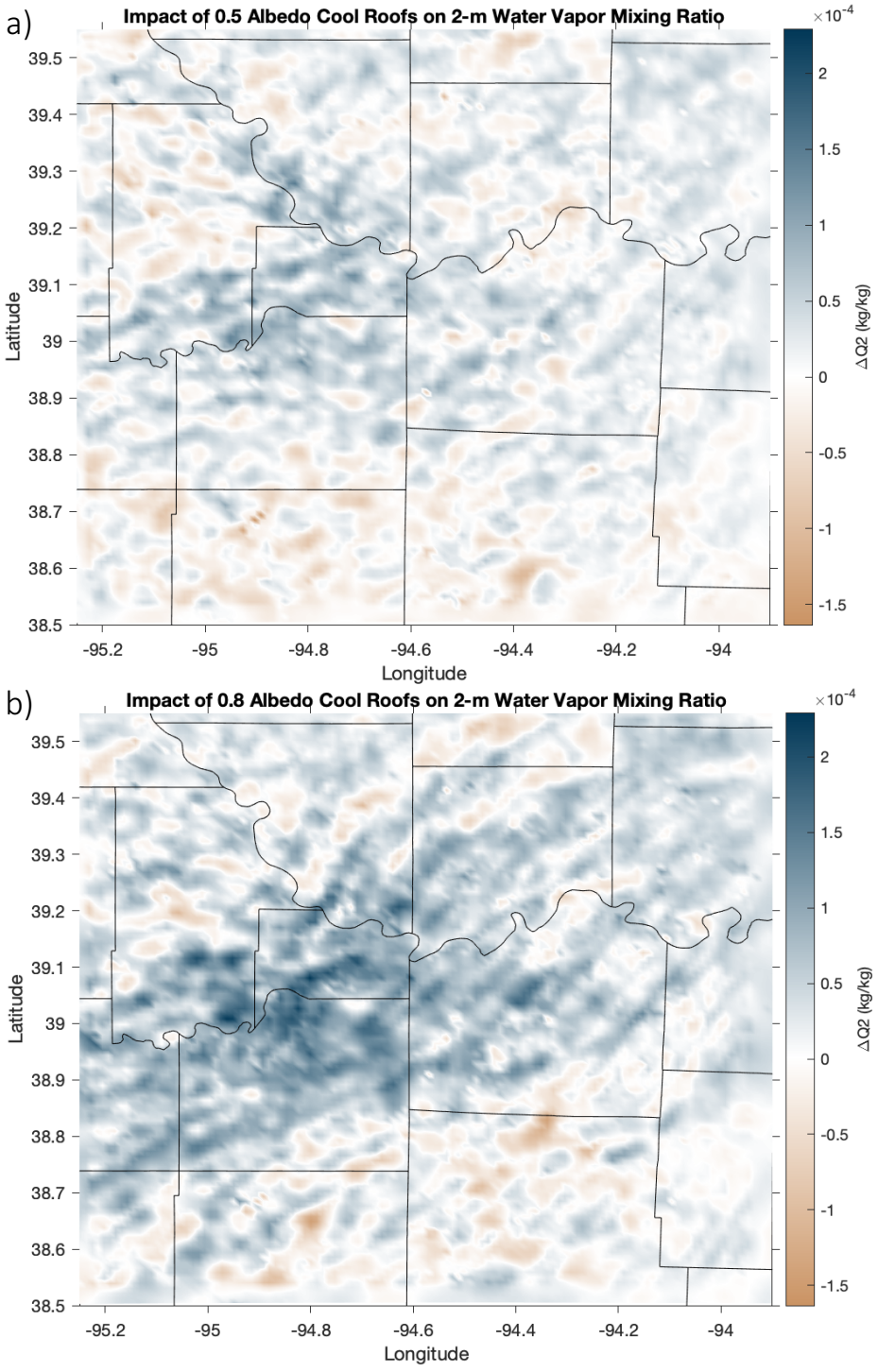

Figure 25. Results for five-day average Q2, comparing the a) 0.5-albedo and f) 0.8-albedo simulations to the control. Colorbar values are $\times 10^{-4}$, and color schemes are equal between the two plots. Note the increase atmospheric moisture over the KCMA in the domain.

The difference in water vapor mixing ratio (Q) with the implementation of cool roofs along a north-south cross-section through the innermost domain at approximately 94.6° W is shown in Figure 26. Both the 0.5- and 0.8-albedo simulations revealed an increase in Q, especially the first one kilometer above the KCMA. Like with Q2, the magnitude of change was greater in the 0.8-albedo case compared to 0.5-albedo. Both scenarios also saw a decrease in Q throughout the cross-section at greater heights, especially between 1-2 km above the surface.

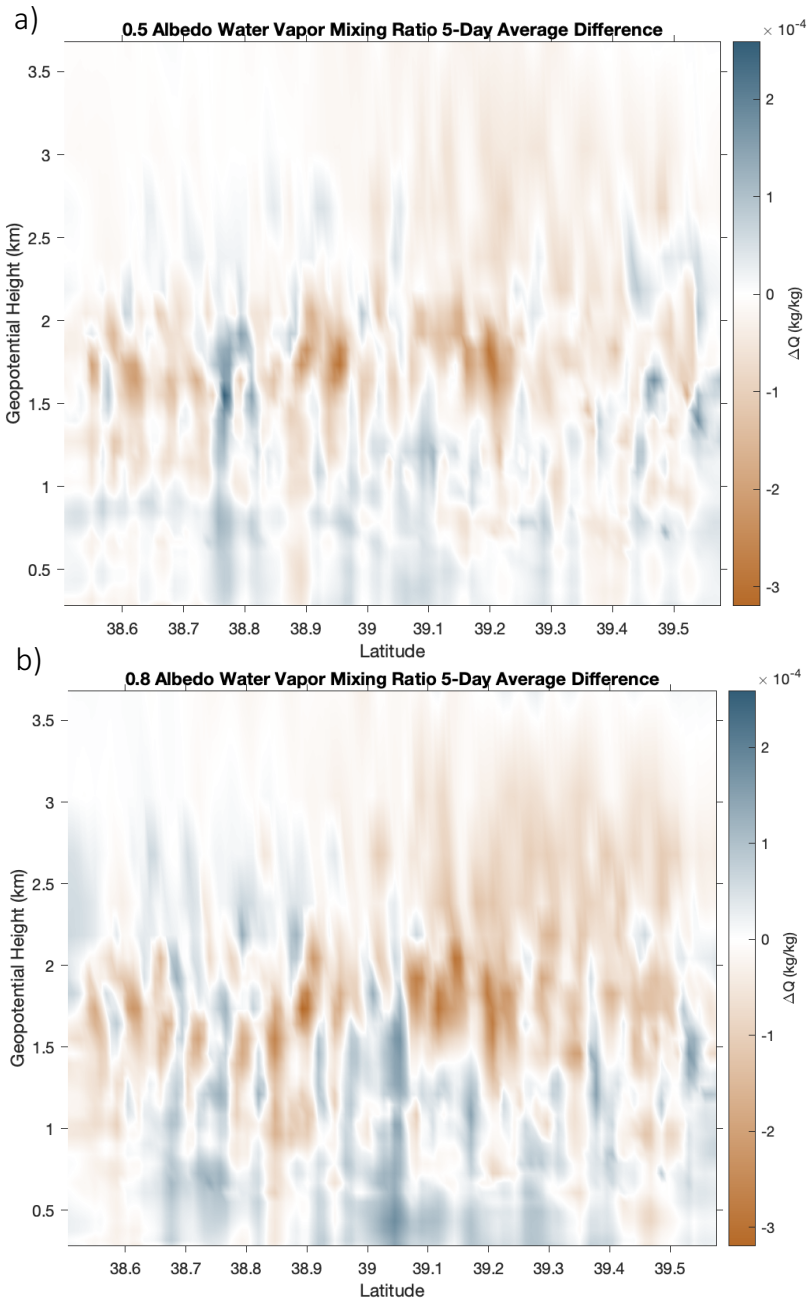

Figure 26. Cross-section of Q from the a) 0.5- and b) 0.8-albedo simulations compared to the control. Cross-section was taken at approximately 94.6° W. Colorbar values are $\times 10^{-4}$, and color schemes are equal between the two plots. The higher-reflectivity roof scenario in b) saw a greater increase in Q difference compared to a), especially near the core of the urban area (i.e. between 39° – 39.1° N). Results in the figure extend vertically to over 3.5 km.

Turbulent kinetic energy and planetary boundary layer height

Due to the influence of turbulent kinetic energy (TKE) on planetary boundary layer (PBL) height, results from both variables will be presented in conjunction. As with Q in the prior section, the difference in TKE between the control and mitigation scenarios was plotted using a cross-section along the longitude of 94.6° W (Figure 27). Both cool roof simulations led to a reduction in TKE in the KCMA, especially between the latitudes of 39° N and 39.2° N where the greatest concentration of industrial/commercial and high-intensity residential urban land cover is located. In this area, the 0.5- and 0.8-albedo scenarios saw a decrease of up to 0.19 m^2/s^2 and 0.49 m^2/s^2, respectively.

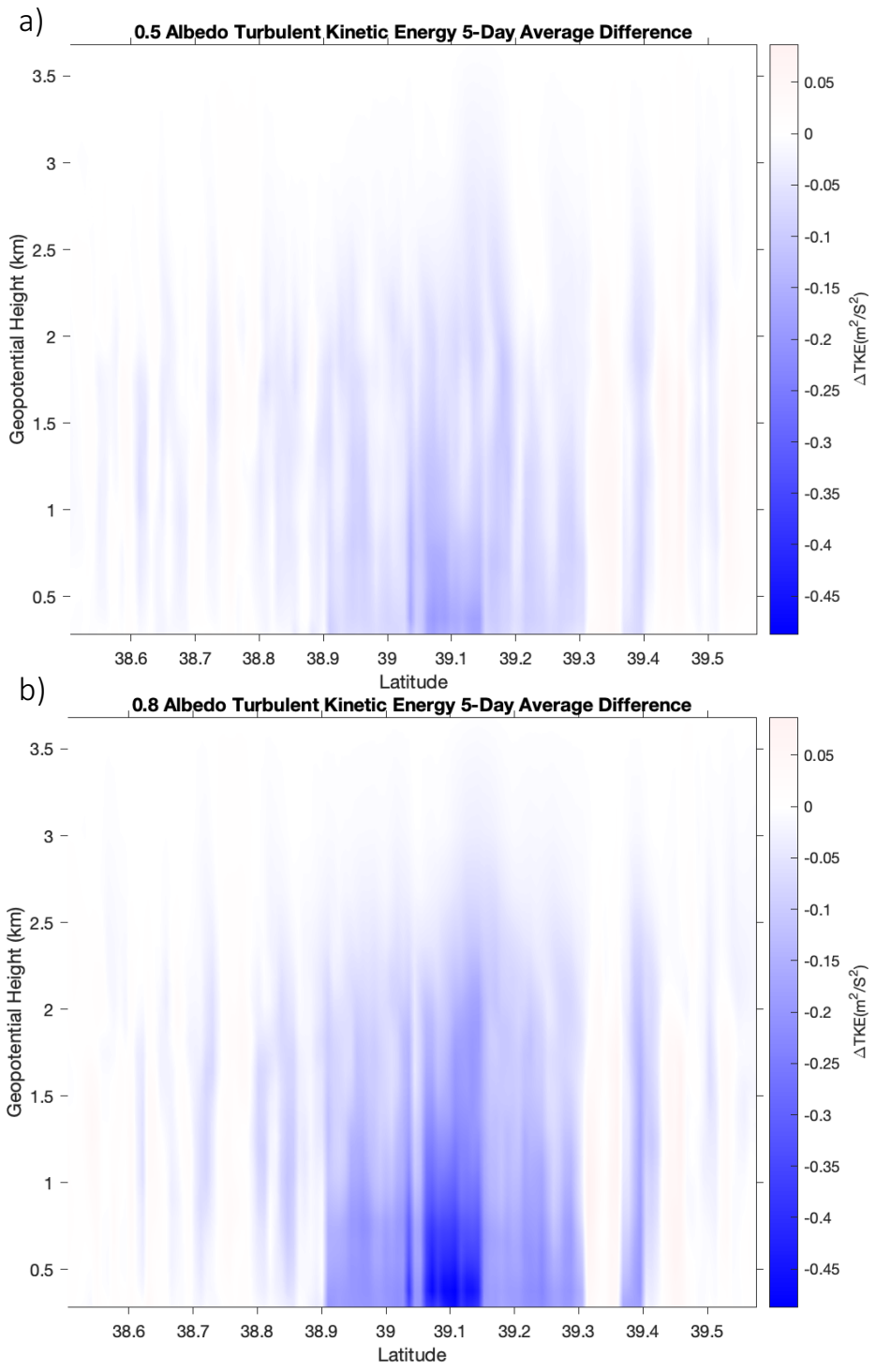

Figure 27. Cross-section at approximately -94° W in domain 1 of the difference in TKE between the a) 0.5- and b) 0.8-albedo and the control. Color schemes are equal between the two figures. Results in the figure extend vertically to over 3.5 km.

The parts of the KCMA that saw the largest reduction in TKE also experienced the greatest loss in PBL height, i.e. areas with the greatest density of impervious surfaces (Figure 28). In the highest albedo case, these areas had an average decrease in PBL height of approximately 93 m compared to the control, while in the "aged" cool roofs simulation, there was an average reduction of approximately 43 m. The low-intensity residential locations saw more modest PBL height decreases. In assessing the diurnal impact of this mitigation strategy at each output time (Figure 29), the plot follows a similar pattern to that of TSK. During the nighttime, little difference in PBL height is seen between the cool roof and control scenarios, but as the sun becomes more overhead during the day, the effect quickly increases to their peak of -50 m and -105 m at 1200 LST for the 0.5- and 0.8-albedo simulations, respectively. Following this time, the difference between the scenarios lessens. Spatial plots at each output time are presented in the Appendix (Figure A6 and Figure A7). The greater magnitudes of PBL height decline during the daytime compared to night are able to be observed in these figures.

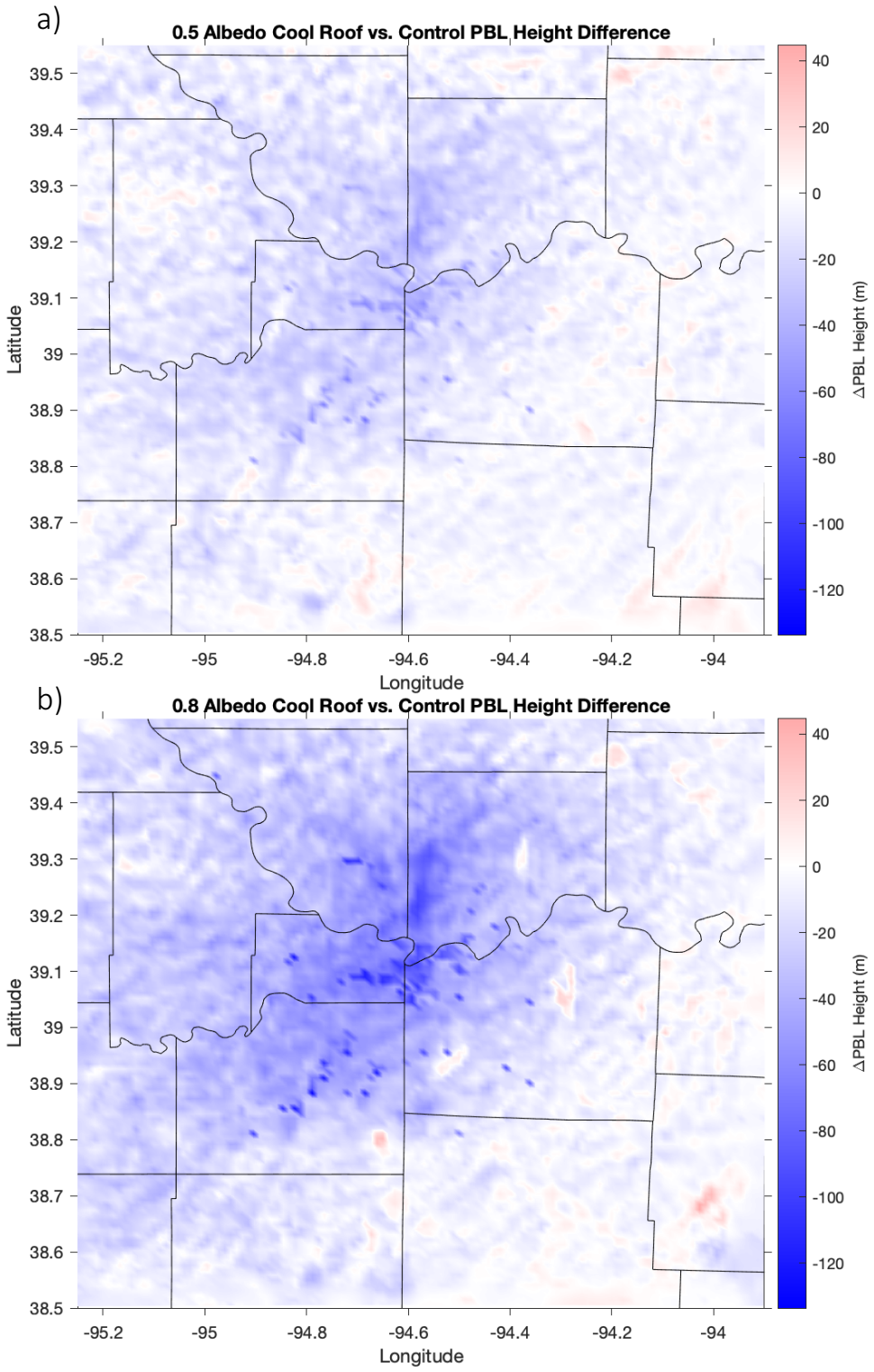

Figure 28. Impact of a) 0.5- and b) 0.8-albedo cool roofs on the PBL height in the KCMA. Color schemes between the two figures are equal.

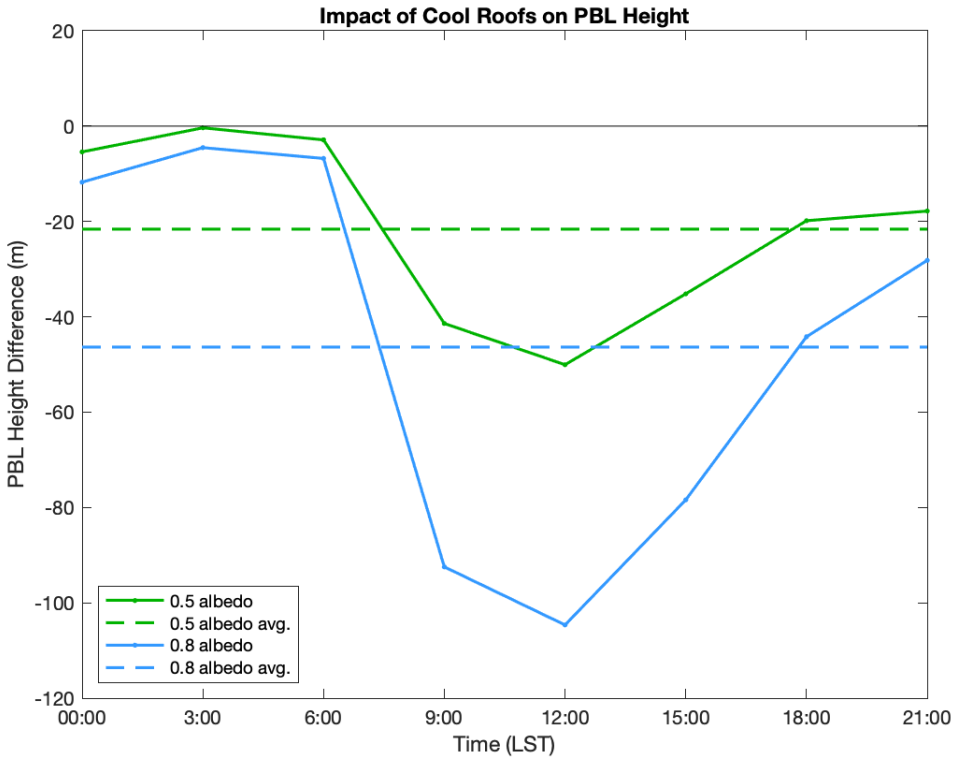

Figure 29. Average change in urban PBL height with the deployment of cool roofs at each model output time. Dashed lines indicate the average change across all output times.

4.4.5 Comparison of median household income and cool roof impact

The final portion of analyzing the data was to compare the impact of cool roofs on T2 within different census tracts and to census tract median household income. Figure 30 shows the median household income from the 2012 American Community Survey five-year estimate (US Census Bureau 2012). A majority of the tracts with lower household incomes are located centrally in the KCMA. The five-day average difference between each cool roof simulation and the control is presented for each tract in Figure 31. This data is equivalent to that in Figure 18, but is presented at census tract-level instead of pixel-level. Like what found in Section 4.4.1, cool roofs provided a greater magnitude of cooling in the central portion of the domain, which corresponds to areas with greater density of impervious surfaces in the KCMA.

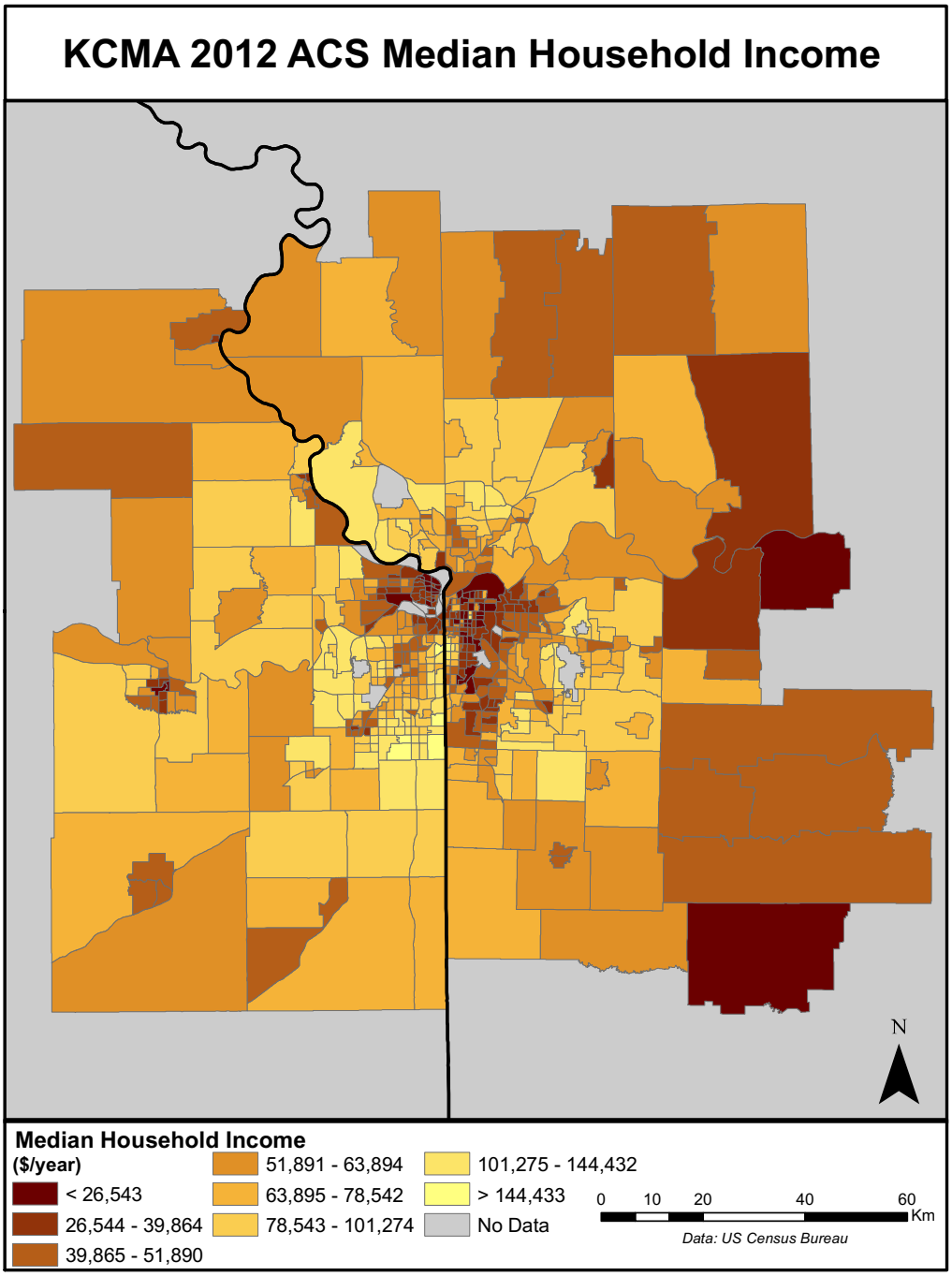

Figure 30. Census tract median household income in the KCMA from the 2012 American Community Survey five-year estimates (US Census Bureau 2012).

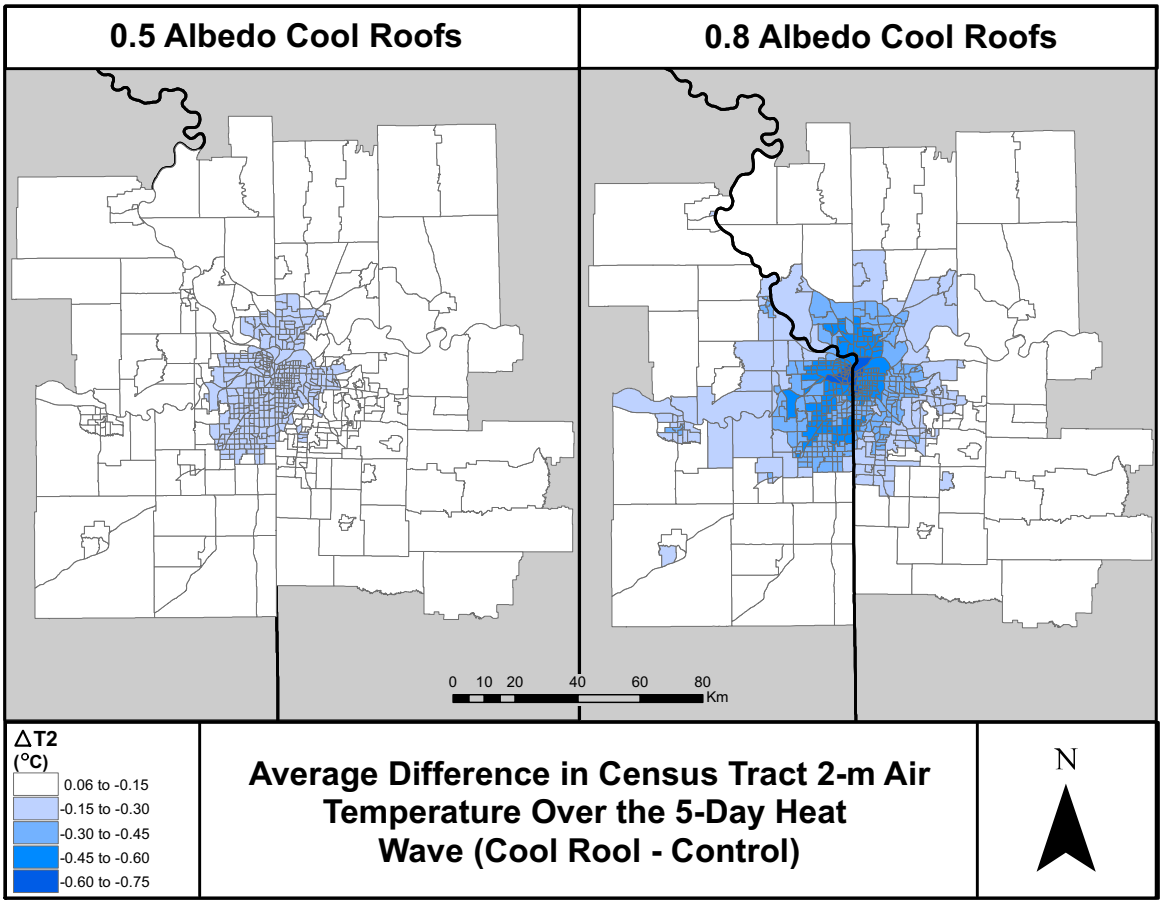

Figure 31. Five-day average T2 difference between the 0.5- (left) and 0.8-albedo (right) cool roof and control simulations. T2 data is equal to that presented previously in Figure 18, but is now presented at census tract level.

In order to focus the analysis on the KCMA within the innermost domain, data from the census tracts that approximately correspond to the cities within the Mid-America Regional Council region were extracted from the prior two figures. Data from the resulting polygon layer (Figure A8; light blue) were used in the following analyses. Next, the histogram for average T2 difference from each census tract was plotted (Figure A9). Both mitigation scenarios yielded slightly positively-skewed histograms, so the Kolmogorov-Smirnov (KS)

test was performed to objectively ensure that both data sets are a non-normal distribution (Table 6). The hypotheses for the KS test were as follows:

$$H_0 : \text{data follows a normal distribution} \quad (6)$$

$$H_A : \text{data does not follow a normal distribution} \quad (7)$$

In the 0.5- and 0.8-alabedo cool roof cases, the *p*-values from the KS test were found to be 0.0059 and 0.0112, respectfully. Since both values are less than α (α = 0.05), the null hypothesis was rejected, indicating that the data sets did not consist of a normal distribution.

Table 6. Results from the Kolmogorov-Smirnov test for normal distribution ($\alpha = 0.05$).

	Kolmogorov-Smirnov Test	
	0.5 Albedo T2 Difference	**0.8 Albedo T2 Difference**
p -value	0.0054	0.0112

Due to having non-normal distributions, the non-parametric Spearman's rank correlation coefficient was calculated for each data, comparing the relationship between census tract median household income and the impact of cool roofs on T2. The correlation coefficients for the impact of 0.5- and 0.8-albedo cool roofs on T2 vs. median household income were found to be 0.41 and 0.50, respectively (Table 7). The hypotheses were as follows:

$$H_0 : \rho_s = 0 \quad (6)$$

$$H_A : \rho_s \neq 0 \quad (7)$$

Both relationships were statistically significant, with *p*-values being less than α (α = 0.05), leading to the rejection of the null hypothesis for each condition. The scatterplots for each comparison are shown in Figure 32, with median household income on the x-axis and T2 difference on the y-axis. Points in the 0.5-albedo simulation are more clustered due to all ΔT2

values being less than 0.3°C. In contrast, points in the 0.8-albedo simulation are more widely dispersed, but the scatterplot shows a clearer relationship of less of a temperature reduction from deployment of cool roofs with increasing median household income.

Table 7. Spearman's rank correlation coefficient for T2 difference and median household income for each census tract in the core urban KCMA ($\alpha = 0.05$).

Spearman's Rank Correlation Coefficient				
	0.5 Albedo T2 Difference		**0.8 Albedo T2 Difference**	
	Corr.	***p*-value**	**Corr.**	***p*-value**
Median Household Income	0.4151	<0.0001	0.5018	<0.0001

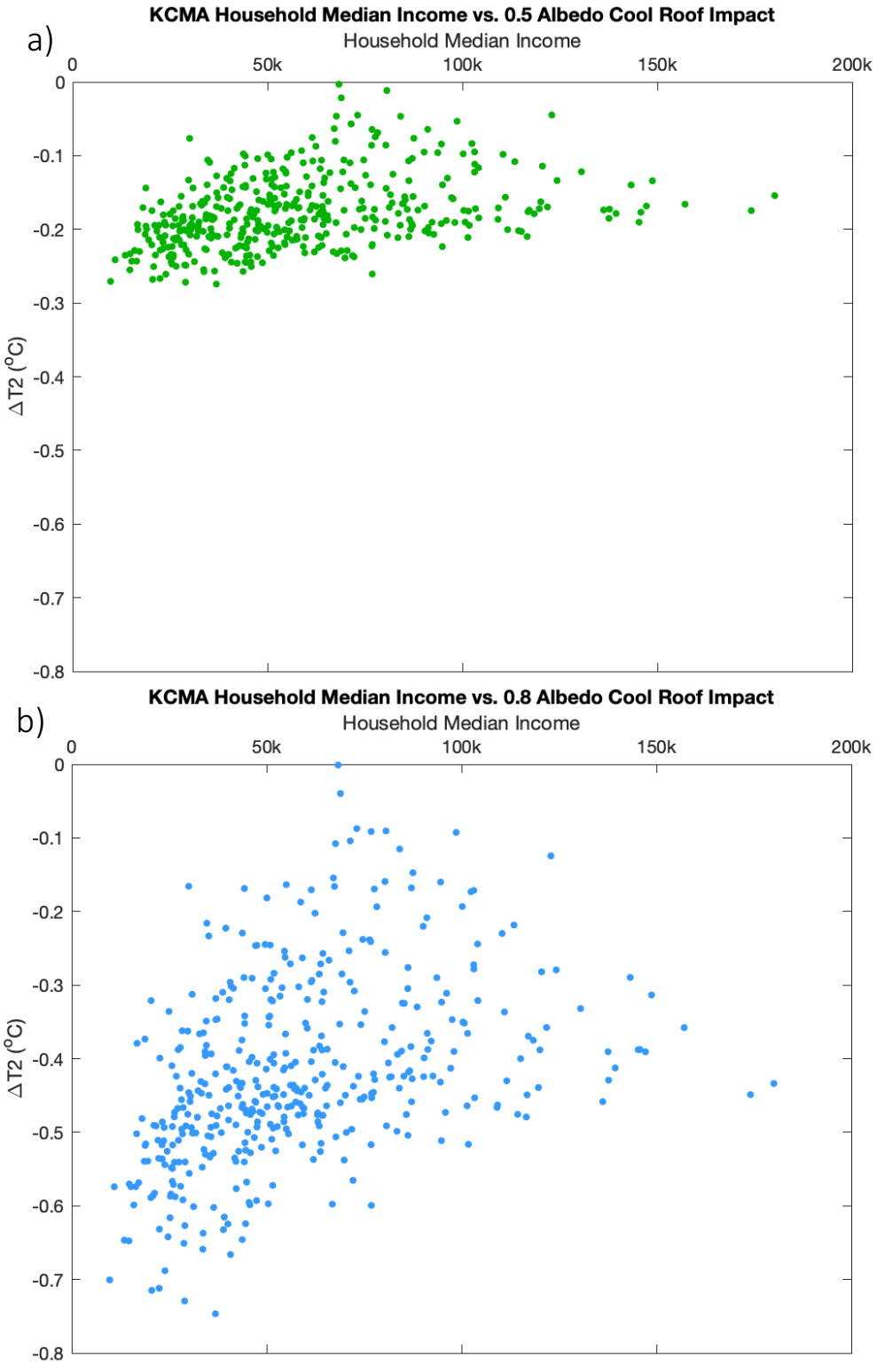

Figure 32. Scatterplots of census tract median household income and T2 difference between the a) 0.5- and b) 0.8-albedo simulations and control.

CHAPTER 5. DISCUSSION

5.1 Evaluation of the control simulation

Overall, WRF was able to re-create the near-surface air temperatures reasonably well. The five-station average RMSE, MB, and MAE were all less than 1.6ºC (i.e. 1.54ºC, 0.65ºC, and 1.23ºC, respectively), and are comparable in magnitude to other studies' control validation results (Vahmani and Ban-Weiss 2016; Morini et al. 2016, 2018; Chen and Zhang 2018). T2 was slightly overestimated as indicated by the low, positive MB value. All five stations, which are distributed throughout the KCMA, provided relatively similar values, with ranges between the minimum and maximum RMSE, MB, and MAE values being less than 0.75ºC. In general, temperatures produced by WRF tended to slightly under-/overestimate observed conditions at lower/higher end of the range of temperatures during the heat wave. A similar pattern was found in a study by Vahmani and Ban-Weiss (2016), where WRF tended to under-/overestimate near-surface air temperature during the nighttime/daytime. Between 23-34ºC, less bias is present as points are well-distributed above and below the identity line (Figure 12).

5.2 Effect of urban expansion on urban temperatures

The purpose of performing a simulation with an estimation of land cover in 1938 was to investigate how excessive urban heat has evolved with development of the KCMA. Upon first glance, temperatures during the heat wave (i.e. 20 – 24 July 2012) indicate only minor differences between the two scenarios, i.e. maximum T2 is approximately equal and they both have average five-day T2 between 31-32ºC. The two cases do deviate from one another overnight, with the historical simulation cooling to a greater extent than the present-day control. In order to further analyze these differences, results were separated by land cover class.

In Figure 15, the impact of greater density of impervious surfaces becomes more pronounced in areas of industrial/commercial and high-intensity residential. From 2100 to 0300 LST, these locations, which are largely clustered in the center of the KCMA, become approximately 2.5-3.1^{o}C warmer in the control case than their corresponding urban pixels in the historical simulation. In addition to an increase in urban temperatures, the expansion of the KCMA areal extent is able to be discerned by an increase in average T2 when comparing the present-day and historical simulations, and is approximated by the area between the blue and green circles in Figure 16. Comparing the number of urban pixels between the two land cover data sets, the increase in the KCMA urban surface area equates to approximately 968 km^2 between 1938 and 2011.

5.3 Impact of cool roofs

Cool roofs were shown to have an impact on multiple variables, especially T2, which directly affects the thermal comfort of those living in the KCMA. When averaged over the entire five-day heat wave and all urban pixels, the 0.5- and 0.8-albedo simulations reduced urban T2 by 0.2^{o}C and 0.45^{o}C, respectively. Multiple comparison testing discovered that the cooling effect from both mitigation scenarios were statistically significant compared to the control. The greatest impact from cool roofs was experienced in areas with industrial/commercial and high-intensity residential land cover, where the five-day average difference in T2 reached -0.3^{o}C and -0.7^{o}C for the 0.5- and 0.8-albedo scenarios, respectively. This is due to the two higher intensity urban land cover categories consisting of a greater percentage of each pixel being covered with buildings that have cool roofs, allowing them to reflect more solar radiation and provide a greater cooling effect than low-intensity residential locations. In regards to output time, the control simulation warmed quicker than the mitigation

scenarios in the morning and midday (0900 and 1200 LST), but cooled slower in the late evening (2100 LST), leading to peaks in T2 difference at these times (Figure 17).

TSK exhibited a similar spatial pattern as T2, where the industrial/commercial and high-intensity residential areas were cooled to a greater extent (0.5-/0.8-albedo: -1°C/-2.5°C) than low-intensity residential locations (-0.6°C/-1.5°C). In contrast to T2, TSK showed more of a straightforward pattern when comparing the cool roof scenarios to the control, i.e. when the sun was more overhead, TSK was reduced to a greater extent. From 0600 LST until 1200 LST, TSK in the control warmed at a quicker rate than with cool roofs, as evidenced ΔTSK becoming more negative during these times. From 1200 – 0000 LST, TSK abated at a faster rate in the control, as evidenced by ΔTSK becoming less negative; however, the cool roof scenarios continued to maintain the KCMA at a lower TSK than the control at these times.

It is also important to take into account the impact that this mitigation strategy has on both the near-surface, i.e. T2, and surface, i.e. TSK, UHI effect (Figure 19 and Figure 22). During this heat wave, the UHI effect was found to be most profound at 2100 LST, which is due to multiple reasons. First, because of their high thermal inertia, impervious surfaces release a substantial amount of heat in the evening that has accumulated throughout the day. In contrast, soil has a lower thermal inertia, especially when it is dry (Oke et al. 2017), e.g. during a heat wave. In addition, a greater density of vegetation in rural locations compared to urban areas assists in cooling local temperatures to a greater extent through latent heat of evaporation. These factors, along with others (see Introduction for more information), cause the UHI effect to be more pronounced during the late evening and night. This phenomenon continues to be prevalent, although to a lesser extent, until 0600 LST due to the slow release of heat throughout the nighttime. One interesting occurrence is that during the daytime, rural areas became

warmer than urban sites. This effect is also due to the difference in thermal inertia between the two surfaces. Rural surfaces are able to take up and release heat more efficiently than impervious surfaces, therefore locations outside the KCMA warm at a faster rate than those within the KCMA. By 1500 LST, the near-surface UHI effect began to form in areas of industrial/commercial land cover in the control simulation, but hadn't formed in the cool roof simulations at this time. Even at 1800 LST, locations with high- and low-intensity residential urban land covers in the 0.8-albedo simulation still had yet to become warmer than rural sites. Similar to the near-surface UHI, the surface UHI effect also still had yet to appear in the two residential land cover classes at 1800 LST during the 0.8-albedo scenario.

The surface energy balance plays a significant role in results obtained for T2 and TSK. With an increase in albedo with cool roofs, both sensible heat flux and net radiation decrease due to a greater percentage of solar radiation being reflected skyward (Figure 23). In addition, the storage heat flux becomes less negative/positive during the daytime/nighttime, indicating a reduction in the amount of heat energy stored/released at these times. In turn, the combination of these effects decreases the near-surface and surface temperatures throughout the day.

One unsuspected result was that the latent heat flux declined in the 0.8-albedo simulation from 0900 – 1200 LST, which was not seen to the same extent in the 0.5-albedo scenario. The high-reflectivity condition also exhibited a greater gain in both Q (for the first kilometer above the surface) and Q2 compared to 0.5-albedo simulation (Figure 25 and Figure 26). One possible explanation for this phenomenon is that due to a reduction in TKE over the KCMA, there is a reduction in PBL height. Due to having a shallower PBL, atmospheric moisture was retained within a smaller volume compared to the control, leading to an increase in Q and Q2 over the urban area. This combination of effects then likely led to a reduction in

evaporation, and therefore, surface latent heat flux was also decreased. A similar finding was reported by Li et al. (2014), but they noted that the decrease in latent heat flux was due to stronger advection of moist air from rural locations. Since the five-day average difference in wind speed between the 0.8-albedo simulation and control is approximately $\pm$0.5 m/s in this study (Figure A10), their rationale would likely not have had a major effect here.

In assessing the social impact of widespread deployment of cool roofs, statistically significant relationships between reductions in T2 from both mitigation scenarios and median household income were identified. The Spearman rank correlation coefficient for the 0.5- and 0.8-albedo simulations were 0.41 and 0.50, respectively. When this information is combined with the scatterplots in Figure 32, a positive relationship between T2 reduction and median household incomes, especially below $50,000 per year, is observed. This indicates that people living in census tracts with lower household incomes would reap the greatest benefits from cool roofs. In addition, many people in these areas have to spend more time outdoors when commuting to work, including walking, riding a bicycle, or waiting for public transportation, compared to other parts of the KCMA (Figure A11). The widespread deployment of cool roofs would assist in relieving the thermal stress they experience, even after aging of the roofs has occurred (i.e. 0.5-albedo simulation).

CHAPTER 6. SUMMARY AND CONCLUSIONS

Over the past seven decades, urban temperatures in the KCMA have grown in both magnitude and areal extent. With an increase in impervious surface density in the central portions of the metro between 1938 and 2011, temperatures in these areas were shown to have increased by over 2.5°C at night during the same simulated heat wave event. Through the widespread deployment of 0.8-albedo cool roofs, these temperatures were able to be reduced by an average of 0.62°C in the more highly developed portions of the innermost domain. After "aging" of the roofs (i.e. albedo of 0.5), temperatures were still decreased by 0.24°C in these locations. Another important aspect of cool roofs from these results was the impact on the actual UHI effect, i.e. the contrast between urban and rural temperatures. As the near-surface UHI effect began to form at 1500 LST in the industrial/commercial parts of the city during the control simulation, both cool roof scenarios were able to push back the onset of this phenomenon until the next output time (i.e. 1800 LST). The 0.8-albedo case was able to even able to delay the UHI effect until 2100 LST in high- and low-intensity residential locations. Although the impact of cool roofs on T2 can lessen over time with the deposition of debris (as indicated by the 0.5-albedo simulation), cool roofs albedo can be restored to 90 – 100% of its original value with cleaning (Bretz and Akbari 1997; Akbari et al. 2005).

In addition to impacting urban temperatures, cool roofs were also shown to have an effect on the heat riskscape in the KCMA. Jenerette et al. (2011) described heat riskscapes as differences in individuals' exposure to environmental heat hazards in an area based on different personal and environmental factors, including socioeconomic status, race/ethnicity, and vegetation density. Many areas in the KCMA that have the greatest density of impervious surfaces (Figure 7), and therefore greatest UHI effect, have median household incomes that are

at the lower-end of the spectrum in this region (Figure 30), indicating that they have less financial resources to cope with more extreme temperatures. Individuals that live in these areas are also more likely to spend a greater amount of time outdoors in order to commute to work (Figure A11). The results from this study show that the deployment of cool roofs in the KCMA has the potential to reduce urban temperatures the most for many citizens that have the least resources available to adapt to these hazards.

One limitation to this study is that it assumes that all buildings in this area are able to have cool roofs installed, which would take a substantial amount of resources to complete. In order to make UHI mitigation more feasible, future research could be directed at investigating the effects of deploying cool roofs in certain portions of the city, e.g. areas with lower median household incomes. Using WRF with the SLUCM, this could be accomplished by increasing roof albedo in only one or two of the three urban land cover categories instead of all three.

APPENDIX

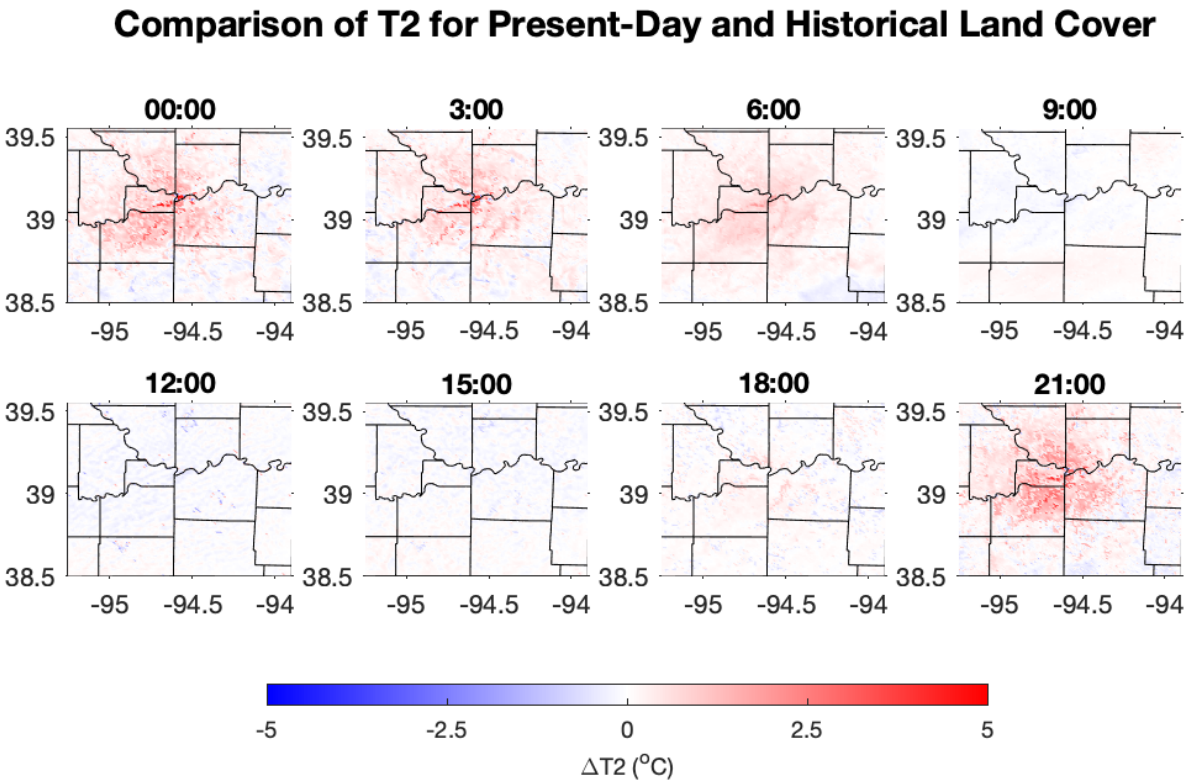

Figure A1. Difference in T2 between the simulations with historical and present-day land cover (historical minus present-day).

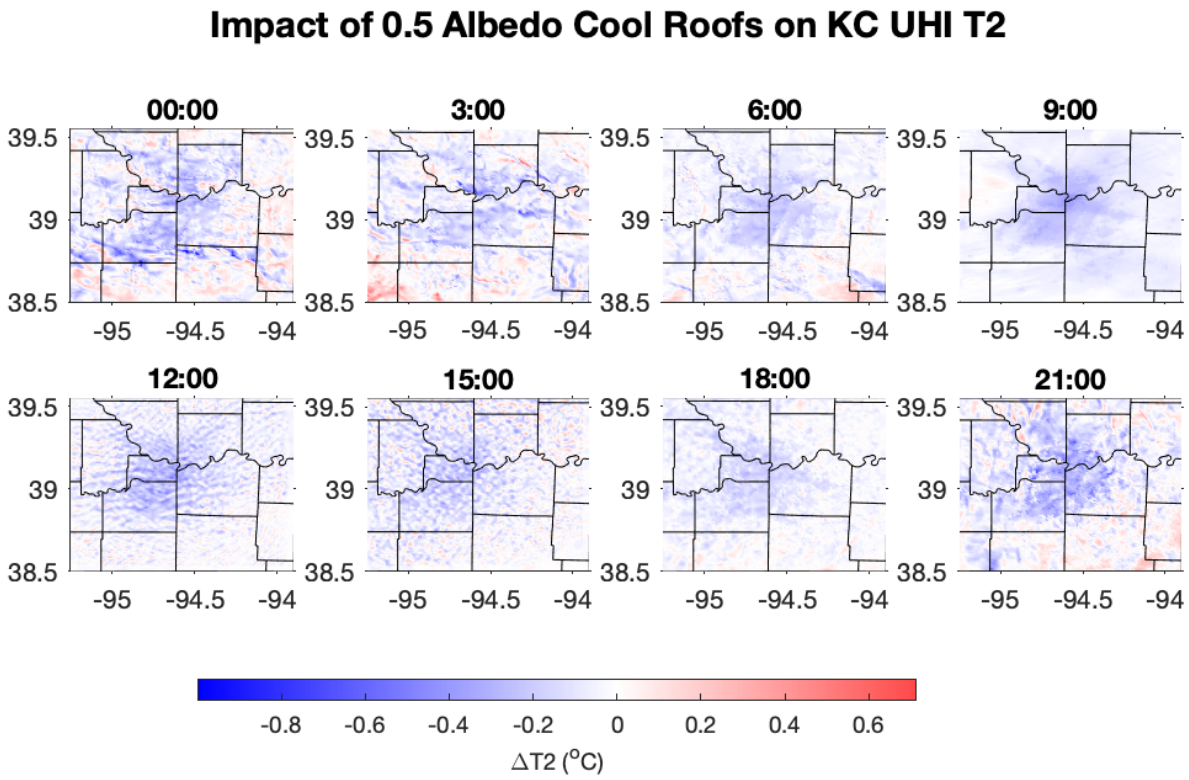

Figure A2. Difference in T2 between the 0.5-albedo and control scenarios for each WRF model output time (cool roof minus control). Color scheme is not equal to that in Figure A3.

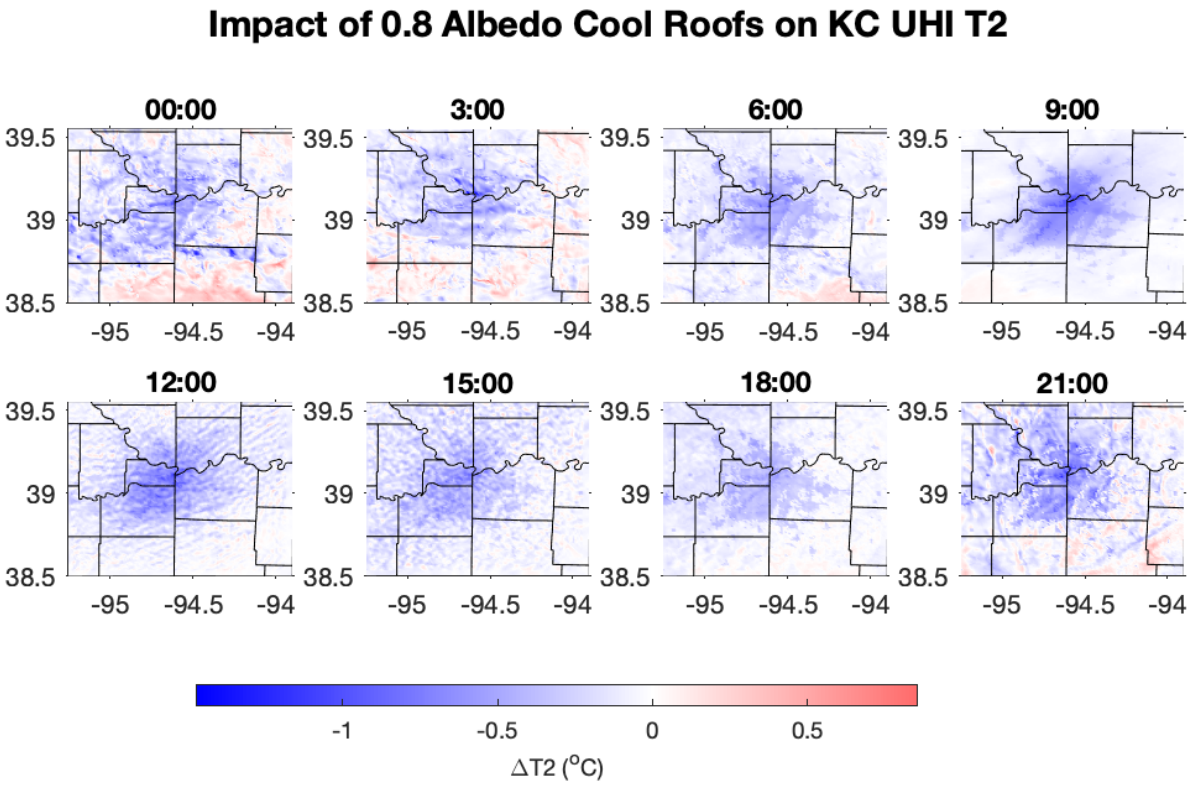

Figure A3. Impact of 0.8-albedo cool roofs on T2 in the KCMA for each WRF model output time (cool roof minus control). Color scheme is not equal to that in Figure A2.

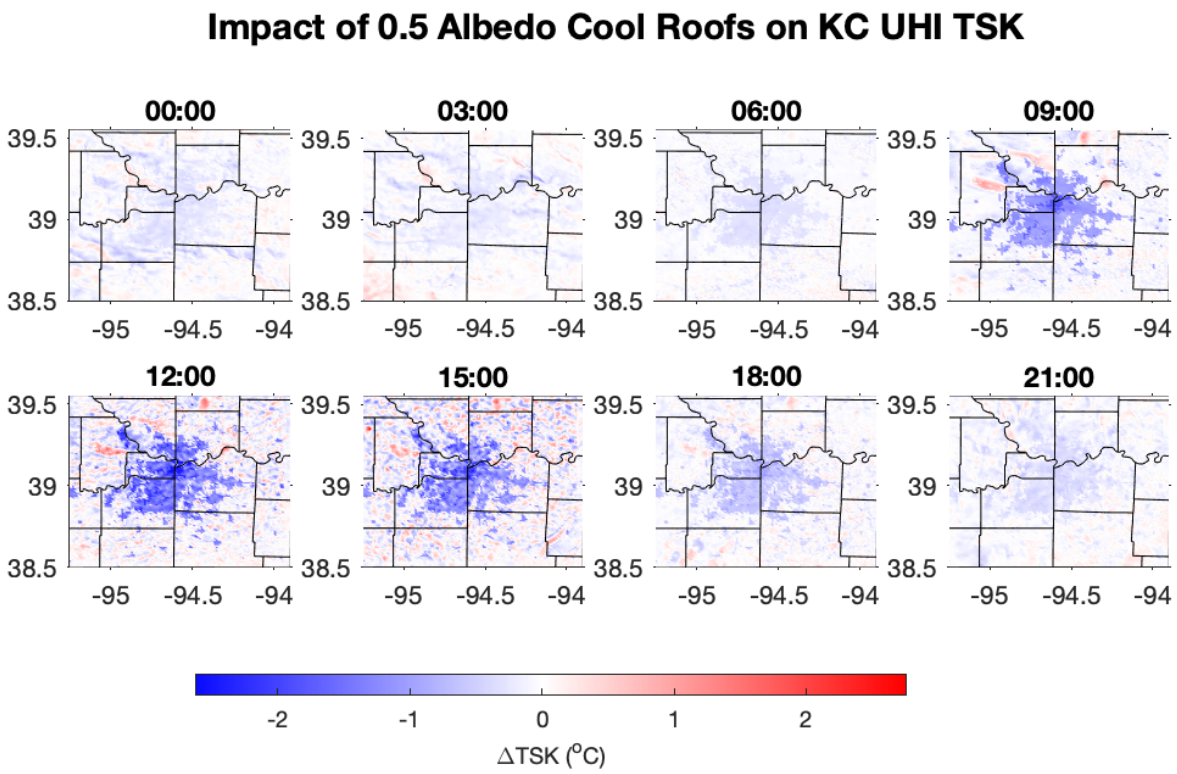

Figure A4. Difference in TSK between the 0.5-albedo and control scenarios for each WRF model output time (cool roof minus control). Color scheme is not equal to that in Figure A5.

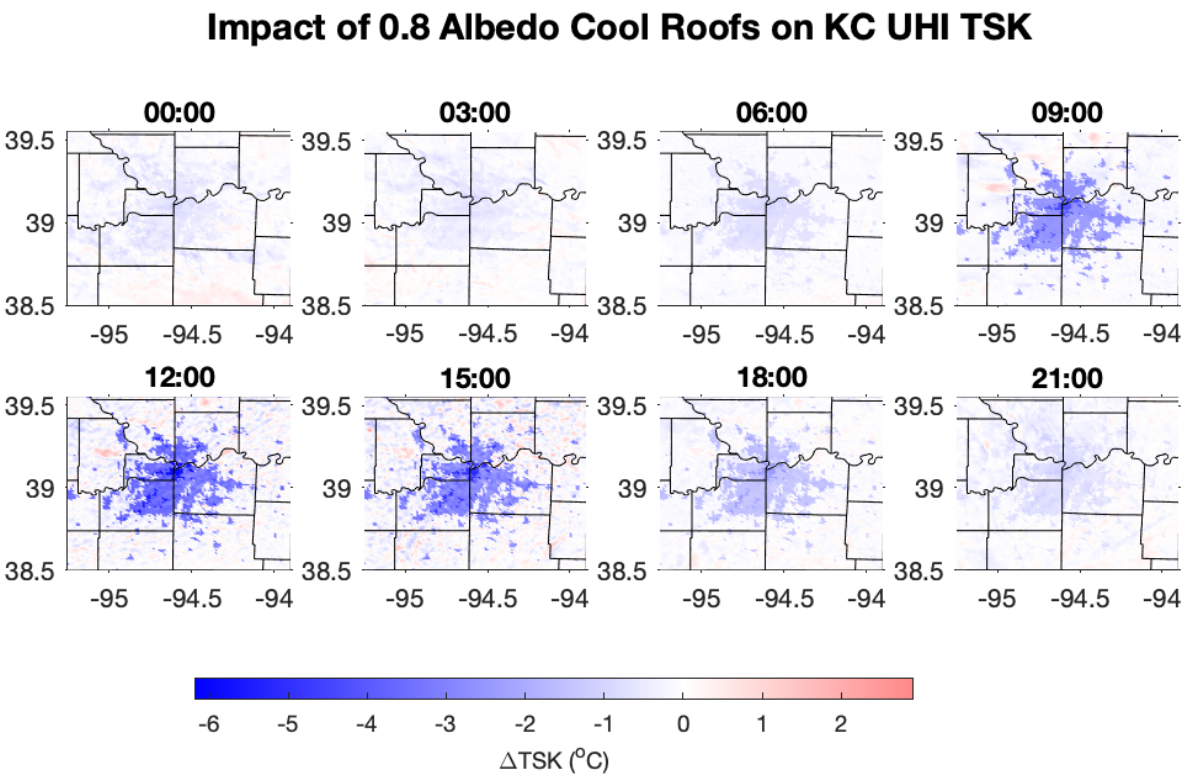

Figure A5. Impact of 0.8-albedo cool roofs on TSK in the KCMA for each WRF model output time (cool roof minus control). Color scheme is not equal to that in Figure A4.

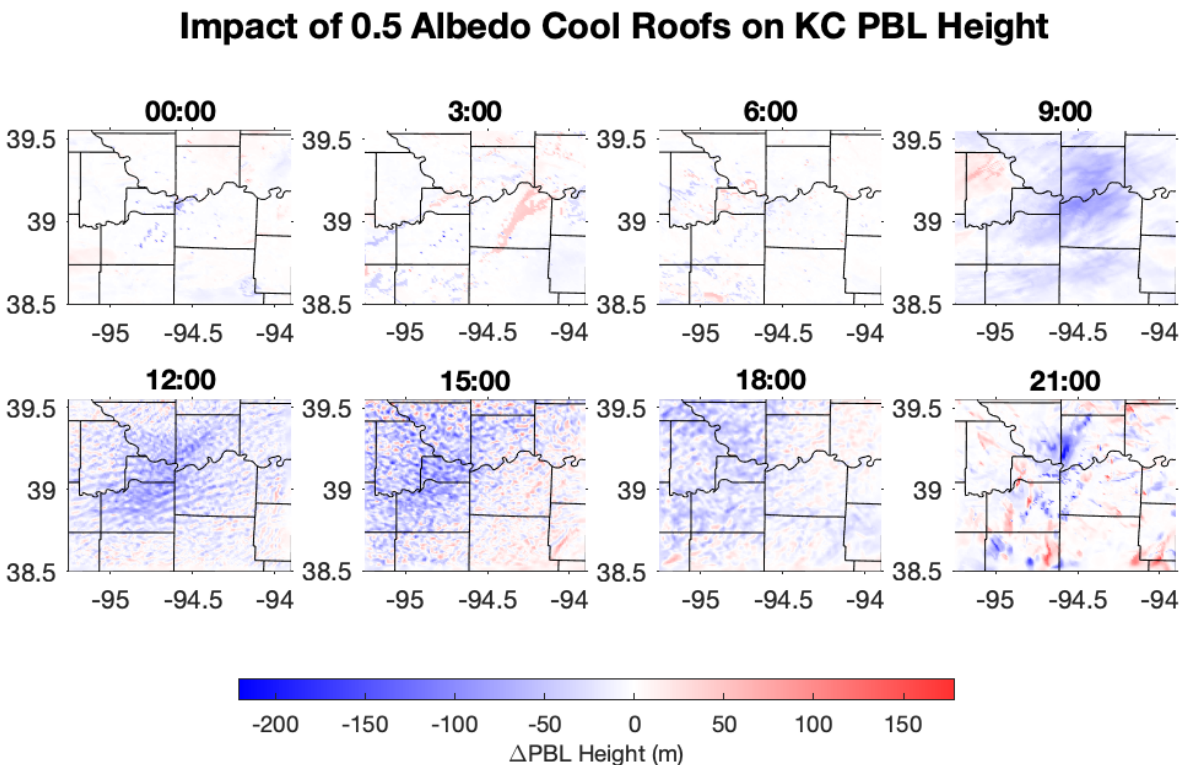

Figure A6. Difference in five-day average PBL height with the installation 0.5-albedo cool roofs for each model output time. Color scheme is not equal to that in Figure A7.

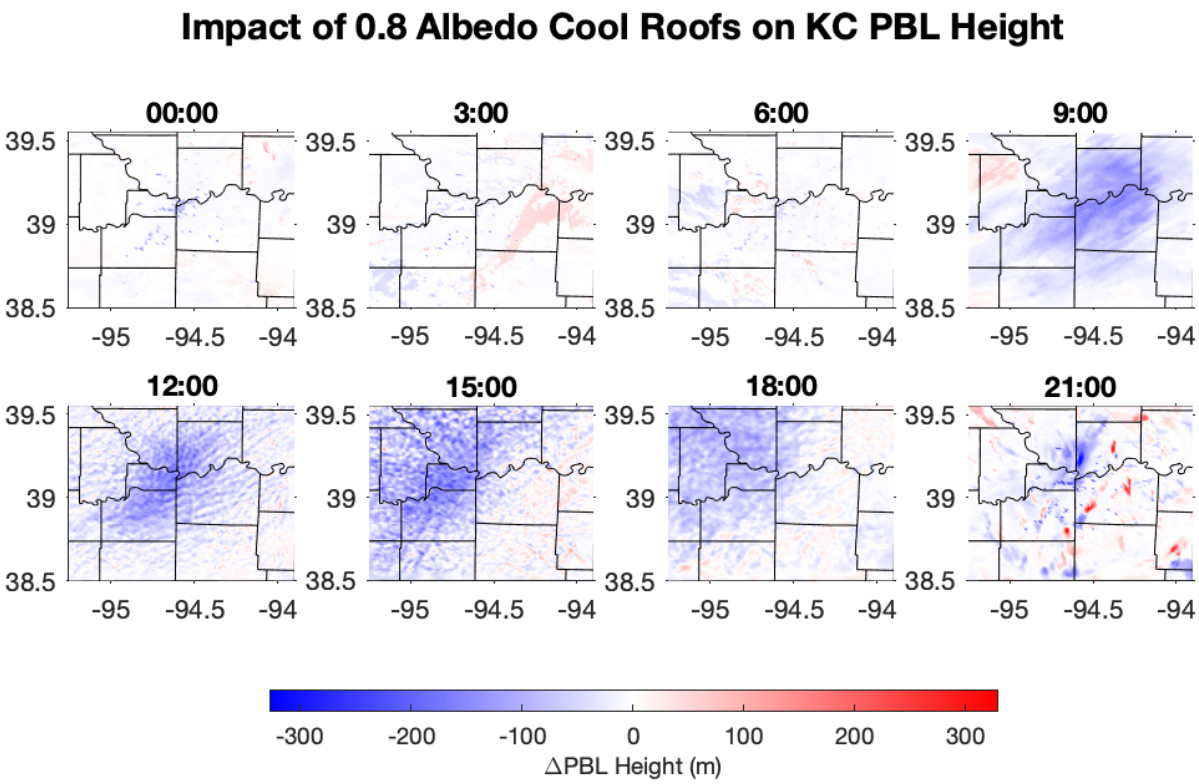

Figure A7. Effect of widespread deployment of 0.8-albedo cool roofs on PBL height in the KCMA. Five-day average results are shown for each output time. Color scheme is not equal to that in Figure A6.

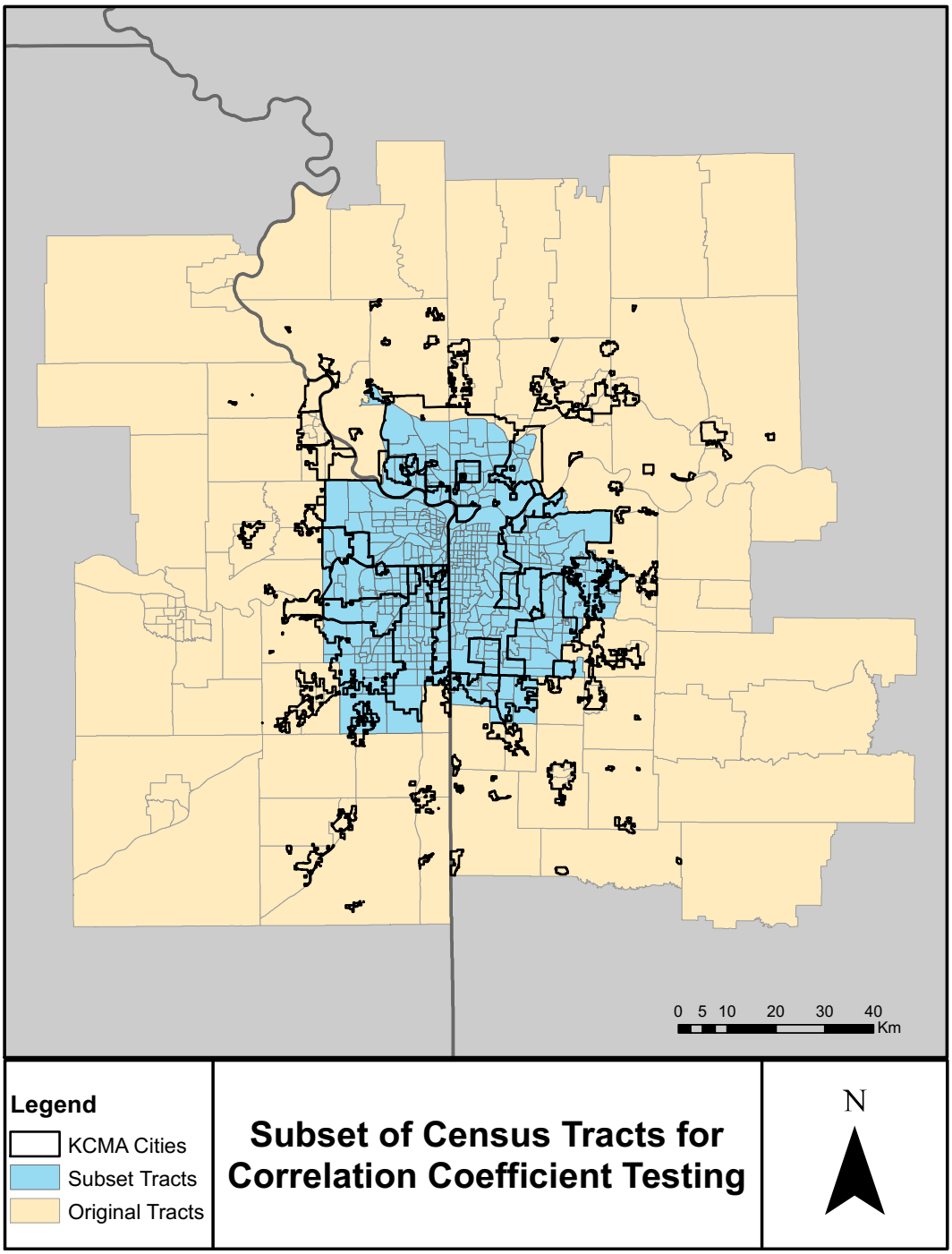

Figure A8. In order to reduce the amount of non-urban areas in the correlation coefficient analysis, T2 and median household income data from the blue census tracts were extracted from the full data set. The thick black lines indicate the boundaries of cities that are part of the Mid-America Regional Council region.

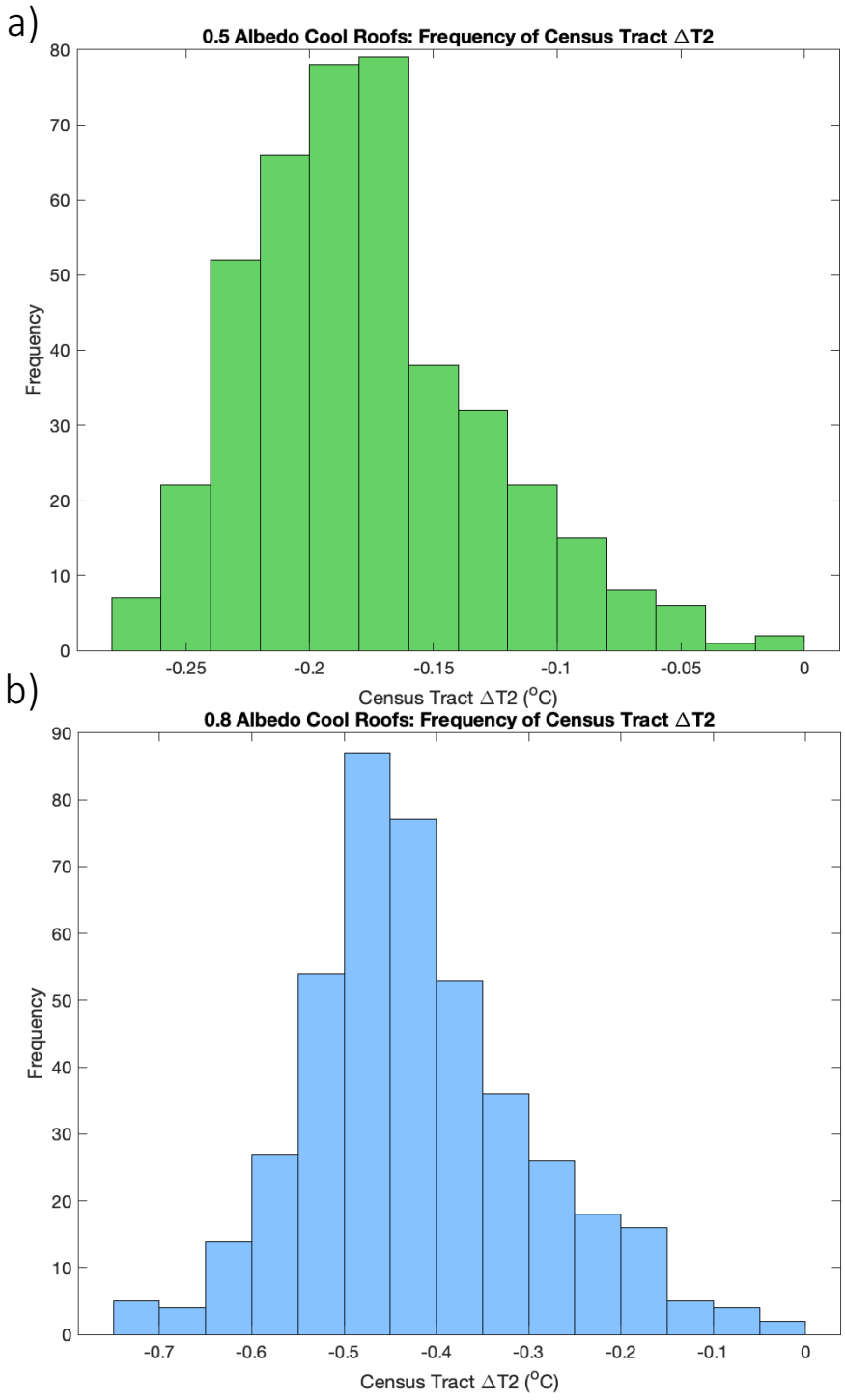

Figure A9. Frequency of census tract T2 difference between the cool roof and control for both the a) 0.5- and b) 0.8-albedo scenarios. Both figures reveal a positively-skewed distribution.

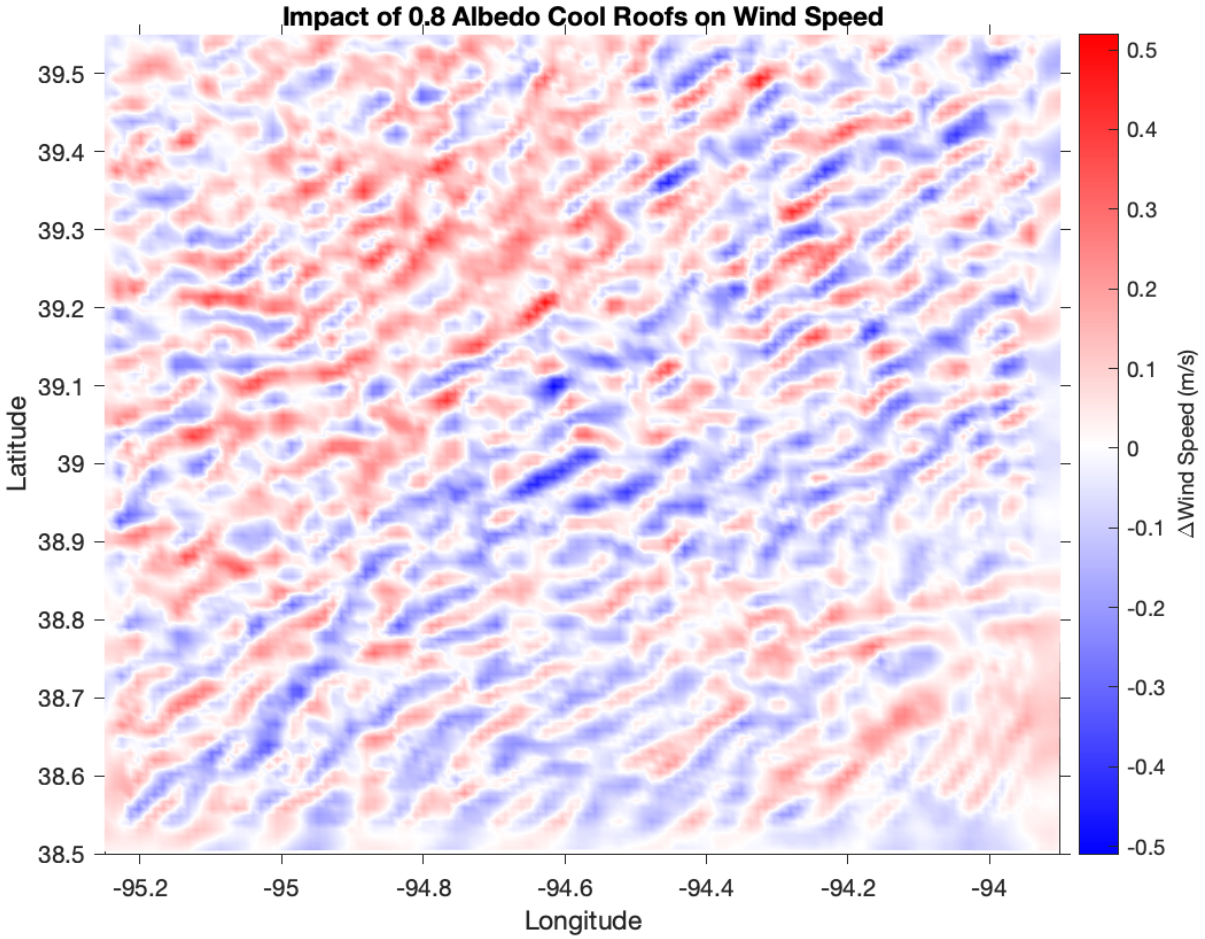

Figure A10. Effect of widespread deployment of 0.8-albedo cool roofs on 10-m wind speed in the KCMA.

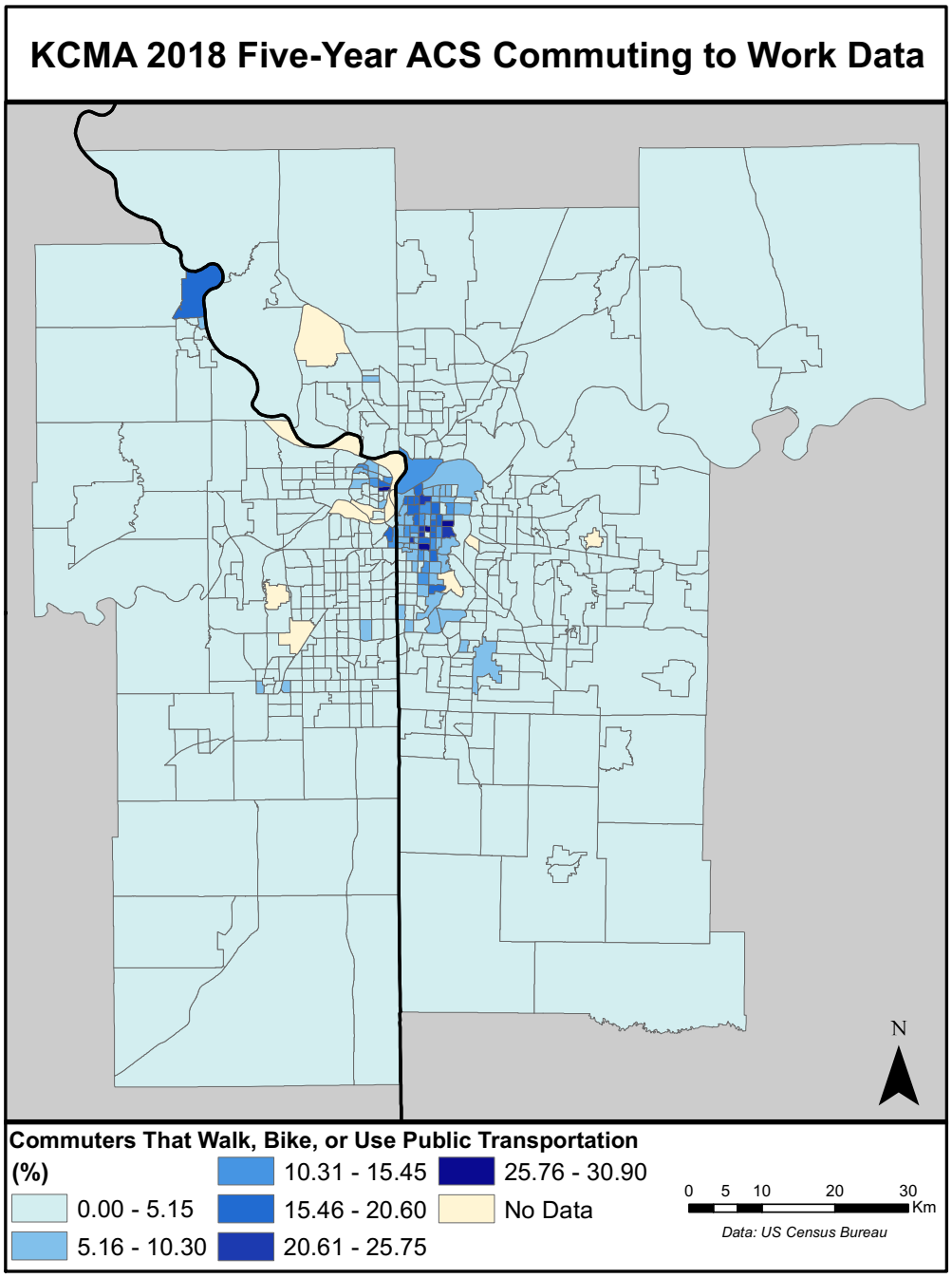

Figure A11. Percent of people in each census tract that have to spend a greater amount of time outdoors when commuting to work because of walking, biking, or using public transportation (US Census Bureau 2018b).

REFERENCES

Akbari, H., A. A. Berhe, R. Levinson, S. Graveline, K. Foley, A. H. Delgado, and R. M. Paroli, 2005: *Aging and weathering of cool roofing membranes*. 15 pp. https://escholarship.org/uc/item/3qb8j3k7#author.

American Meteorological Society, 2012: Surface Energy Balance. Accessed December 12, 2019, http://glossary.ametsoc.org/wiki/Surface_energy_balance.

Bhati, S., and M. Mohan, 2016: WRF model evaluation for the urban heat island assessment under varying land use/land cover and reference site conditions. *Theor. Appl. Climatol.*, **126**, 385–400, doi:10.1007/s00704-015-1589-5.

Bretz, S. E., and H. Akbari, 1997: Long-term performance of high-albedo roof coatings. *Energy Build.*, **25**, 159–167, doi:10.1016/s0378-7788(96)01005-5.

Cao, M., P. Rosado, Z. Lin, R. Levinson, and D. Millstein, 2015: Cool Roofs in Guangzhou, China: Outdoor Air Temperature Reductions during Heat Waves and Typical Summer Conditions. *Environ. Sci. Technol.*, **49**, 14672–14679, doi:10.1021/acs.est.5b04886.

Carvalho, D., H. Martins, M. Marta-Almeida, A. Rocha, and C. Borrego, 2017: Urban Climate Urban resilience to future urban heat waves under a climate change scenario : A case study for Porto urban area (Portugal). *Urban Clim.*, **19**, 1–27, doi:10.1016/j.uclim.2016.11.005.

Chai, T., and R. R. Draxler, 2014: Root mean square error (RMSE) or mean absolute error (MAE)? -Arguments against avoiding RMSE in the literature. *Geosci. Model Dev.*, **7**, 1247–1250, doi:10.5194/gmd-7-1247-2014.

Chen, F., and Coauthors, 2011: The integrated WRF/urban modelling system: Development, evaluation, and applications to urban environmental problems. *Int. J. Climatol.*, **31**,

273–288, doi:10.1002/joc.2158.

Chen, Y., and N. Zhang, 2018: Urban heat island mitigation effectiveness under extreme heat conditions in the Suzhou-Wuxi-Changzhou Metropolitan area, China. *J. Appl. Meteorol. Climatol.*, **57**, 235–253, doi:10.1175/JAMC-D-17-0101.1.

Christopherson, R. W., and G. H. Birkeland, 2015: *Geosystems*. 9th ed. Macmillan Publishing Company, Upper Saddle River, NJ, 262–263 pp.

Climate Central, 2012: 2012 Record Temperatures: Which States Led the Nation. Accessed December 13, 2019, https://www.climatecentral.org/news/2012-record-temperatures-which-states-led-the-nation-14951.

Cool Roof Rating Council, 2016: *Policy Makers and Code Officials: Learn About Cool Roofs*. 2 pp. https://coolroofs.org/documents/Policy.pdf.

Crum, S. M., S. A. Shiflett, and G. D. Jenerette, 2017: The influence of vegetation, mesoclimate and meteorology on urban atmospheric microclimates across a coastal to desert climate gradient. *J. Environ. Manage.*, **200**, 295–303, doi:10.1016/j.jenvman.2017.05.077.

Dunn, O. J., 1961: Multiple Comparisons Among Means. *J. Am. Stat. Assoc.*, **56**, 52, doi:10.2307/2282330.

ENERGY STAR, 2020: Roof Products Key Product Criteria. *Energy Effic. Prod.*,. Accessed January 12, 2020, https://www.energystar.gov/products/building_products/roof_products/key_product_criteria.

Environmental Protection Agency, 2006: *Excessive Heat Events Guidebook*. 60pp pp.

——, 2008: Cool Roofs. *Reducing Urban Heat Islands: Compendium of Strategies*, 16–18.

——, 2009: *Land-Use Scenarios:National-Scale Housing Density Scenarios Consistent with Climate Change Storylines*. Washington, D.C., 137 pp.

Georgescu, M., 2015: Challenges Associated with Adaptation to Future Urban Expansion. *J. Clim.*, **28**, 2544–2563, doi:10.1175/JCLI-D-14-00290.1.

——, P. E. Morefield, B. G. Bierwagen, and C. P. Weaver, 2014: Urban adaptation can roll back warming of emerging megapolitan regions. *Proc. Natl. Acad. Sci.*, **111**, 2909–2914, doi:10.1073/pnas.1322280111.

Google Maps, 2020: Google Maps Satellite View - Kansas City. Accessed May 1, 2020, https://www.google.com/maps.

Harlan, S. L., A. J. Brazel, L. Prashad, W. L. Stefanov, and L. Larsen, 2006: Neighborhood microclimates and vulnerability to heat stress. *Soc. Sci. Med.*, **63**, 2847–2863, doi:10.1016/j.socscimed.2006.07.030.

Hartmann, D. L., 1994: *Global Physical Climatology*. 1st ed. Academic Press, San Diego, 411 pp.

He, C., Z. Liu, S. Gou, Q. Zhang, J. Zhang, and L. Xu, 2019: Detecting global urban expansion over the last three decades using a fully convolutional network. *Environ. Res. Lett.*, **14**, doi:10.1088/1748-9326/aaf936.

Heaviside, C., S. Vardoulakis, and X. M. Cai, 2016: Attribution of mortality to the urban heat island during heatwaves in the West Midlands, UK. *Environ. Heal. A Glob. Access Sci. Source*, **15**, 49–59, doi:10.1186/s12940-016-0100-9.

Hoerling, M., J. Eischeid, A. Kumar, R. Leung, A. Mariotti, K. Mo, S. Schubert, and R. Seager, 2014: Causes and predictability of the 2012 Great Plains drought. *Bull. Am. Meteorol. Soc.*, **95**, 269–282, doi:10.1175/BAMS-D-13-00055.1.

Homer, C., and Coauthors, 2020: Conterminous United States land cover change patterns 2001–2016 from the 2016 National Land Cover Database. *ISPRS J. Photogramm. Remote Sens.*, **162**, 184–199, doi:10.1016/j.isprsjprs.2020.02.019.

Homer, C. G., and Coauthors, 2015: Completion of the 2011 National Land Cover Database for the conterminous United States – representing a decade of land cover change information. *Photogramm. Eng. Remote Sensing*, **81**, 345–353.

Husain, S. Z., S. Bélair, and S. Leroyer, 2014: Influence of soil moisture on urban microclimate and surface-layer meteorology in Oklahoma City. *J. Appl. Meteorol. Climatol.*, **53**, 83–98, doi:10.1175/JAMC-D-13-0156.1.

Imran, H. M., J. Kala, A. W. . Ng, and S. Muthukumaran, 2018: Effectiveness of green and cool roofs in mitigating urban heat island effects during a heatwave event in the city of Melbourne in southeast Australia. *J. Clean. Prod.*, **197**, 393–405, doi:10.1016/j.jclepro.2018.06.179.

Inhabitat, 2006: Chicago Green Roof Program.

Jaffal, I., S.-E. Ouldboukhitine, and R. Belarbi, 2012: A comprehensive study of the impact of green roofs on building energy performance. *Renew. Energy*, **43**, 157–164, doi:10.1016/j.renene.2011.12.004.

Jenerette, G. D., S. L. Harlan, W. L. Stefanov, C. A. Martin, G. D. Jenerette, S. L. Harlan, W. L. Stefanov, and C. A. Martin, 2011: Ecosystem services and urban heat riskscape moderation: water, green spaces, and social inequality in Phoenix, USA. *Ecol. Soc. Am.*, **21**, 2637–2651, doi:10.1890/10-1493.1.

Jeong, S., D. Millstein, and R. Levinson, 2019: *Evaluation of urban heat island mitigation strategies for the Kansas City region*. 1–25 pp.

https://www.marc.org/Environment/pdf/EvaluationofUrbanHeatIslandMitigationStrategiesKCR.aspx.

Jeworrek, J., G. West, and R. Stull, 2019: Evaluation of cumulus and microphysics parameterizations in WRF across the convective gray zone. *Weather Forecast.*, **34**, 1097–1115, doi:10.1175/WAF-D-18-0178.1.

Kaiser, D., M. Köhler, M. Schmidt, and F. Wolff, 2019: Increasing Evapotranspiration on Extensive Green Roofs by Changing Substrate Depths, Construction, and Additional Irrigation. *Buildings*, **9**, 173, doi:10.3390/buildings9070173.

Kenward, A., D. Yawitz, T. Sanford, and R. Wang, 2014: *Summer in the city: Hot and getting hotter*. 29 pp.

Kusaka, H., and F. Kimura, 2004: Coupling a Single-Layer Urban Canopy Model with a Simple Atmospheric Model : Impact on Urban Heat Island Simulation for an Idealized Case Coupling a Single-Layer Urban Canopy Model with a Simple Atmospheric Model : Impact on Urban Heat Island Simulation f. *J. Meteorol. Soc. Japan*, **82**, 67–80, doi:10.2151/jmsj.82.67.

——, H. Kondo, Y. Kikegawa, and F. Kimura, 2001: A Simple Single-Layer Urban Canopy Model For Atmospheric Models : Comparison With Multi-Layer And Slab Models. *Boundary-Layer Meteorol.*, **101**, 329–358, doi:10.1023/A.

Laaidi, K., A. Zeghnoun, P. Bretin, E. Giraudet, and P. Beaudeau, 2012: The Impact of Heat Islands on Mortality in Paris during the August 2003 Heat Wave. *Environ. Health Perspect.*, **120**, 254–259.

Li, D., E. Bou-Zeid, and M. Oppenheimer, 2014: The effectiveness of cool and green roofs as urban heat island mitigation strategies. *Environ. Res. Lett.*, **9**.

Liu, X., G. Tian, J. Feng, J. Wang, and L. Kong, 2018: Assessing summertime urban warming and the cooling ef fi cacy of adaptation strategy in the Chengdu-Chongqing metropolitan region of China. *Sci. Total Environ.*, **610**–**611**, 1092–1102, doi:10.1016/j.scitotenv.2017.08.082.

Luber, G., and M. McGeehin, 2008: Climate Change and Extreme Heat Events. *Am. J. Prev. Med.*, **35**, 429–435, doi:10.1016/j.amepre.2008.08.021.

Lund, M., C. Stiegler, J. Abermann, M. Citterio, B. U. Hansen, and D. van As, 2017: Spatiotemporal variability in surface energy balance across tundra, snow and ice in Greenland. *Ambio*, **46**, 81–93, doi:10.1007/s13280-016-0867-5.

Ma, S., A. Pitman, J. Yang, C. Carouge, J. P. Evans, M. Hart, and D. Green, 2018: Evaluating the effectiveness of mitigation options on heat stress for Sydney, Australia. *J. Appl. Meteorol. Climatol.*, **57**, 209–220, doi:10.1175/JAMC-D-17-0061.1.

Mentens, J., D. Raes, and M. Hermy, 2006: Green roofs as a tool for solving the rainwater runoff problem in the urbanized 21st century? *Landsc. Urban Plan.*, **77**, 217–226, doi:10.1016/j.landurbplan.2005.02.010.

Mesinger, F., and Coauthors, 2005: North American Regional Reanalysis. *Bull. Am. Meteorol. Soc.*, **87**, 42.

Mid-America Regional Council, 2010: *Land Use in Greater Kansas City*. 2 pp.

——, 2014: *Appendix B: Land use and traffic forecasting*. 10 pp.

Mills, G., 2008: Luke Howard and The Climate of London. *Weather*, **63**, 153–157, doi:10.1002/wea.195.

Mitchell, B. C., and J. Chakraborty, 2018: Exploring the relationship between residential segregation and thermal inequity in 20 U.S. cities. *Local Environ.*, **23**, 796–813,

doi:10.1080/13549839.2018.1474861.

Morini, E., A. G. Touchaei, B. Castellani, F. Rossi, and F. Cotana, 2016: The impact of albedo increase to mitigate the urban heat island in Terni (Italy) using the WRF model. *Sustain.*, **8**, 1–14, doi:10.3390/su8100999.

——, A. G. Touchaei, F. Rossi, F. Cotana, and H. Akbari, 2018: Evaluation of albedo enhancement to mitigate impacts of urban heat island in Rome (Italy) using WRF meteorological model. *Urban Clim.*, **24**, 551–566, doi:10.1016/j.uclim.2017.08.001. https://doi.org/10.1016/j.uclim.2017.08.001.

National Climatic Data Center, 2012: 1981-2010 Normals. Accessed December 15, 2019, https://www.ncdc.noaa.gov/cdo-web/datatools/normals.

National Oceanic and Atmospheric Administration, 2020: Daily-Observed Data. *Autom. Surf. Obs. Syst.*,. Accessed December 15, 2019, https://mrcc.illinois.edu/CLIMATE/.

National Weather Service, 2019: Weather Related Fatality and Injury Statistics. https://www.weather.gov/hazstat/.

Oke, T. R., 1982: The energetic basis of the urban heat island. *Q. J. R. Meteorol. Soc.*, **108**, 1–24, doi:10.1002/qj.49710845502.

Oke, T. R., G. Mills, A. Christen, and J. A. Voogt, 2017: *Urban Climates*. Cambridge University Press, New York, 525 pp.

Robine, J. M., S. L. K. Cheung, S. Le Roy, H. Van Oyen, C. Griffiths, J. P. Michel, and F. R. Herrmann, 2008: Death toll exceeded 70,000 in Europe during the summer of 2003. *Comptes Rendus - Biol.*, **331**, 171–178, doi:10.1016/j.crvi.2007.12.001.

Rowe, D. B., 2011: Green roofs as a means of pollution abatement. *Environ. Pollut.*, **159**, 2100–2110, doi:10.1016/j.envpol.2010.10.029.

Salamanca, F., M. Georgescu, A. Mahalov, M. Moustaoui, and M. Wang, 2014: Anthropogenic heating of the urban environment due to air conditioning. *J. Geophys. Res. Atmos.*, **119**, 5949–5965, doi:10.1002/2013JD021225.Received.

Santamouris, M., 2013: Using cool pavements as a mitigation strategy to fight urban heat island - A review of the actual developments. *Renew. Sustain. Energy Rev.*, **26**, 224–240, doi:10.1016/j.rser.2013.05.047. http://dx.doi.org/10.1016/j.rser.2013.05.047.

——, A. Synnefa, and T. Karlessi, 2011: Using advanced cool materials in the urban built environment to mitigate heat islands and improve thermal comfort conditions. *Sol. Energy*, **85**, 3085–3102, doi:10.1016/j.solener.2010.12.023. http://dx.doi.org/10.1016/j.solener.2010.12.023.

Seto, K. C., M. Fragkias, B. Guneralp, and M. K. Reilly, 2011: A Meta-Analysis of Global Urban Land Expansion. *PLoS One*, **6**, 1–9, doi:10.1371/ journal.pone.0023777.

Sharma, A., P. Conry, H. J. S. Fernando, A. F. Hamlet, J. J. Hellmann, and F. Chen, 2016: Green and cool roofs to mitigate urban heat island effects in the Chicago metropolitan area: evaluation with a regional climate model. *Environ. Res. Lett.*, **11**, 1–15, doi:10.1088/1748-9326/11/6/064004.

Shiflett, S. A., L. L. Liang, S. M. Crum, G. L. Feyisa, J. Wang, and G. D. Jenerette, 2017: Variation in the urban vegetation, surface temperature, air temperature nexus. *Sci. Total Environ.*, **579**, 495–505, doi:10.1016/j.scitotenv.2016.11.069.

Skamarock, W. C., and Coauthors, 2008: A Description of the Advanced Research WRF Version 3. *NCAR Tech. Note*, 125.

Snodgrass, E. C., and L. L. Snodgrass, 2006: *Green roof plants: a resource and planting guide*. Timber Press, Portland, OR, 37 pp.

Sohl, T., R. Reker, M. Bouchard, K. Sayler, J. Dornbierer, S. Wika, R. Quenzer, and A. Friesz, 2016: Modeled historical land use and land cover for the conterminous United States. *J. Land Use Sci.*, **11**, 476–499, doi:10.1080/1747423X.2016.1147619.

Su, Z., 2002: The Surface Energy Balance System (SEBS) for estimation of turbulent heat fluxes. *Hydrol. Earth Syst. Sci.*, **6**, 85–100, doi:10.5194/hess-6-85-2002.

Sun, T., C. S. B. Grimmond, and G. Ni, 2016: How do green roofs mitigate urban thermal stress under heat waves? *J. Geophys. Res. Atmos.*, **121**, 5320–5335, doi:10.1002/2016JD024873.Received.

Tewari, M., F. Chen, H. Kusaka, and S. Miao, 2007: Coupled WRF/Unified Noah/Urban-Canopy Modeling System. 22. https://ral.ucar.edu/sites/default/files/public/product-tool/WRF-LSM-Urban.pdf%0A.

——, J. Yang, H. Kusaka, F. Salamanca, C. Watson, and L. Treinish, 2019: Interaction of urban heat islands and heat waves under current and future climate conditions and their mitigation using green and cool roofs in New York City and Phoenix, Arizona. *Environ. Res. Lett.*, **14**, doi:10.1088/1748-9326/aaf431.

United Nations, 2018: *World Urbanization Prospects: The 2018 Revision*. 2 pp.

Urban, B., and K. Roth, 2010: *Guidelines for selecting cool roofs*. 5 pp. https://heatisland.lbl.gov/sites/all/files/coolroofguide_0.pdf.

US Census Bureau, 2012: 2008-2012 American Community Survey 5-Year Estimates. Accessed February 14, 2020, https://factfinder.census.gov/faces/nav/jsf/pages/index.xhtml.

——, 2018a: Community Facts. *Am. Fact Finder*,. Accessed January 3, 2020, https://factfinder.census.gov/faces/nav/jsf/pages/index.xhtml.

——, 2018b: 2014-2018 American Community Survey 5-Year Estimates. Accessed February 15, 2020, https://factfinder.census.gov/faces/nav/jsf/pages/index.xhtml.

Vahmani, P., and G. A. Ban-Weiss, 2016: Impact of remotely sensed albedo and vegetation fraction on simulation of urban climate in WRF-urban canopy model: A case study of the urban heat island in Los Angeles. *J. Geophys. Res.*, **121**, 1511–1531, doi:10.1002/2015JD023718.

Vahmani, P., and A. D. Jones, 2017: Water conservation benefits of urban heat mitigation. *Nat. Commun.*, **8**, doi:10.1038/s41467-017-01346-1. http://dx.doi.org/10.1038/s41467-017-01346-1.

Vahmani, P., F. Sun, A. Hall, and G. Ban-Weiss, 2016: Investigating the climate impacts of urbanization and the potential for cool roofs to counter future climate change in Southern California. *Environ. Res. Lett.*, **11**.

Wang, J., Q. Meng, K. Tan, L. Zhang, and Y. Zhang, 2018: Experimental investigation on the influence of evaporative cooling of permeable pavements on outdoor thermal environment. *Build. Environ.*, **140**, 184–193, doi:10.1016/j.buildenv.2018.05.033.

Whiting, D., and N. Unwin, 2008: Cities, urbanization and health. *Int. J. Epidemiol.*, **38**, 1737–1742, doi:10.1093/ije/dyn152.

Yang, J., and E. Bou-Zeid, 2019: Scale dependence of the benefits and efficiency of green and cool roofs. *Landsc. Urban Plan.*, **185**, 127–140, doi:10.1016/j.landurbplan.2019.02.004.

——, Z. H. Wang, M. Georgescu, F. Chen, and M. Tewari, 2016: Assessing the Impact of Enhanced Hydrological Processes on Urban Hydrometeorology with Application to Two Cities in Contrasting Climates. *J. Hydrometeorol.*, **17**, 1031–1047,

doi:10.1175/JHM-D-15-0112.1.

Yang, L., and Coauthors, 2018: A new generation of the United States National Land Cover Database: Requirements, research priorities, design, and implementation strategies. *ISPRS J. Photogramm. Remote Sens.*, **146**, 108–123, doi:10.1016/j.isprsjprs.2018.09.006.

Zhang, N., Y. Chen, L. Luo, and Y. Wang, 2017: Effectiveness of Different Urban Heat Island Mitigation Methods and Their Regional Impacts. *J. Hydrometeorol.*, **18**, 2991–3012, doi:10.1175/JHM-D-17-0049.1.

VITA

Kyle Reed received his Bachelor of Science in Biology in May 2008 from Fort Hays State University, then earned his Doctor of Physical Therapy degree from the University of Kansas Medical Center in May 2012. In 2017, Kyle returned to school at the University of Missouri – Kansas City (UMKC), attaining his Bachelor of Science in Geography with an undergraduate certificate in GIS in May 2018. He then continued with his master's at UMKC the following fall semester, earning a Master of Science in Environmental and Urban Geosciences degree. While at UMKC, Kyle worked as an undergraduate and graduate research associate for Dr. Fengpeng Sun.

In July 2018, Kyle had the opportunity to attend a week-long training in the use of the Weather Research and Forecasting (WRF) model at the National Center for Atmospheric Research in Boulder, CO. Kyle has been able to present his work at multiple events, including the 2018 Missouri Transect annual meeting in Kansas City, MO, 2018 AGU Fall Meeting in Washington, D.C., 2019 UMKC Community of Scholars in Kansas City, MO, 2019 UMKC Faculty Research Symposium in Kansas City, MO, 2019 Missouri Space Grant Consortium annual meeting in Rolla, MO, and the 2019 AGU Fall Meeting in San Francisco, CA. Kyle is affiliated Gamma Theta Upsilon, an international honor society in geography. His publications include:

Reed, K. and Sun, F. (2020): Investigating Climate Impacts of Urbanization and Mitigation of the UHI Effect using Cool Roofs in the Kansas City Metropolitan Area. Manuscript in Preparation.

Reed K. and F. Sun, (2019): Investigating Climate Impacts of Urbanization and the Potential for Cool Roofs to Mitigate Future Climate Change in Kansas City, NASA-Missouri Space Grant Consortium. 9 pp. Technical Report.